

The physics of ink-jet printing onto thin porous substrates

Citation for published version (APA):

Murali, V. (2021). *The physics of ink-jet printing onto thin porous substrates*. [Phd Thesis 1 (Research TU/e / Graduation TU/e), Applied Physics and Science Education]. Eindhoven University of Technology.

Document status and date:

Published: 23/11/2021

Document Version:

Publisher's PDF, also known as Version of Record (includes final page, issue and volume numbers)

Please check the document version of this publication:

- A submitted manuscript is the version of the article upon submission and before peer-review. There can be important differences between the submitted version and the official published version of record. People interested in the research are advised to contact the author for the final version of the publication, or visit the DOI to the publisher's website.
- The final author version and the galley proof are versions of the publication after peer review.
- The final published version features the final layout of the paper including the volume, issue and page numbers.

[Link to publication](#)

General rights

Copyright and moral rights for the publications made accessible in the public portal are retained by the authors and/or other copyright owners and it is a condition of accessing publications that users recognise and abide by the legal requirements associated with these rights.

- Users may download and print one copy of any publication from the public portal for the purpose of private study or research.
- You may not further distribute the material or use it for any profit-making activity or commercial gain
- You may freely distribute the URL identifying the publication in the public portal.

If the publication is distributed under the terms of Article 25fa of the Dutch Copyright Act, indicated by the "Taverne" license above, please follow below link for the End User Agreement:

www.tue.nl/taverne

Take down policy

If you believe that this document breaches copyright please contact us at:

openaccess@tue.nl

providing details and we will investigate your claim.

The physics of ink-jet printing onto thin porous substrates

Vignesh Murali



This work is part of the research programme " The role of surfactants in spreading and sorption of water based printing inks" with project number 14666, which is partly financed by the Netherlands organisation for scientific research (NWO). Additional funding is provided by Océ-Technologies B.V.

Copyright © 2021, Vignesh Murali
All rights reserved.

A catalogue record is available from the Eindhoven University of Technology Library

ISBN: 978-90-386-5399-0

NUR: 925

The physics of ink-jet printing onto thin porous substrates

PROEFSCHRIFT

ter verkrijging van de graad van doctor aan de Technische Universiteit Eindhoven, op gezag van de rector magnificus prof.dr.ir. F.P.T. Baaijens, voor een commissie aangewezen door het College voor Promoties, in het openbaar te verdedigen op dinsdag 23 november 2021 om 11:00 uur

door

Vignesh Murali

geboren te Chennai, India

Dit proefschrift is goedgekeurd door de promotoren en de samenstelling van de promotiecommissie is als volgt:

voorzitter:	prof.dr.ir. G.M.W. Kroesen
1e promotor:	prof.dr. A.A Darhuber
co-promotor:	dr.ir. J.C.H. Zeegers (Technische Universiteit Eindhoven)
leden:	prof.dr. F. Mugele (Universiteit Twente)
	dr.ir. Wouter den Otter (Universiteit Twente)
	dr.ir. R.H.J Peerlings
	prof.dr.ir. H.M.A Wijshoff
adviseur:	Dr. N. Tomozeiu

Het onderzoek of ontwerp dat in dit proefschrift wordt beschreven is uitgevoerd in overeenstemming met de TU/e Gedragscode Wetenschapsbeoefening.

Contents

1	Introduction	1
1.1	Fundamentals of ink-jet printing	1
1.1.1	Droplet generation and emission	2
1.1.2	Print-control	5
1.1.3	Deposited solution/material processing	6
1.2	Outline	9
2	Infrared thermography of sorptive heating of thin porous media	11
2.1	Introduction	11
2.2	Experimental	12
2.3	Experimental results	14
2.4	Theoretical model	17
2.4.1	Transport in the thin porous medium domain	17
2.4.2	Gas-phase domain	19
2.4.3	Evaporation rate, sorptive heating and evaporative cooling	20
2.4.4	Initial and boundary conditions	21
2.5	Discussion	23
2.5.1	Moisture transport in the paper substrate	23
2.5.2	Convection-diffusion in the gas phase	25
2.5.3	Scaling analysis	27
2.5.4	Limitations of our model	29
2.6	Summary and conclusions	29
3	Inkjet deposition of lines onto thin moving porous media	33
3.1	Introduction	33
3.2	Materials and methods	35
3.2.1	Experimental set-up, inkjet operation and dual-visualization	35
3.2.2	Calibration of intensity vs. moisture content	37
3.2.3	The maximum liquid holding capacity of paper	38
3.3	Experimental results	39
3.3.1	Variation of the deposition frequency	39
3.3.2	Variation of the substrate speed	41

3.3.3	Transient evolution of a deposited line	44
3.4	Theoretical model	45
3.4.1	Moisture transport	45
3.4.2	Heat transfer	47
3.4.3	Boundary conditions	49
3.4.4	The inkjet deposition term j_{IJ}	49
3.5	Discussion	50
3.5.1	The effect of the frequency of deposition	50
3.5.2	The effects of the substrate velocity	52
3.5.3	Transient evolution	54
3.5.4	Scaling behavior	55
3.5.5	Including the gas phase – 3D simulations	56
3.6	Summary and conclusions	57

4 Inkjet deposition of lines of surfactant solutions onto thin moving porous media 61

4.1	Introduction	61
4.2	Materials and methods	63
4.2.1	Surfactant properties	63
4.2.2	Surfactant adsorption	64
4.2.3	Evaporation of surfactant solutions	65
4.2.4	Maximum holding capacity of paper	65
4.2.5	Calibration of transmitted intensity vs. moisture content	66
4.2.6	Possible reasons for surfactant-induced reduction of light transmission	67
4.3	Experimental results	68
4.3.1	Variation of substrate speed	68
4.3.2	Variation of deposition rate	71
4.3.3	Variation of surfactant concentration	72
4.3.4	Effect of paper type	73
4.4	Theoretical model	74
4.4.1	Modified Darcy velocity	75
4.4.2	Dual-porosity description of pore-fiber exchange	75
4.4.3	Solute transport in unsaturated porous media	76
4.4.4	Initial and boundary conditions	77
4.5	Discussion	77
4.5.1	Variation of the droplet deposition frequency	77
4.5.2	Variation of the substrate speed	79
4.5.3	Variation of the surfactant concentration	81
4.5.4	Effect of surfactant adsorption	81

4.5.5	Intensity overshoot	83
4.5.6	Surfactant precipitation	84
4.6	Summary and conclusions	85
5	Chromatographic effects in inkjet printing	89
5.1	Introduction	89
5.2	Materials and methods	90
5.3	Experimental results	92
5.3.1	Drop casting	92
5.3.2	Inkjet deposition of colorant lines	92
5.4	Theoretical model	94
5.4.1	Scales and dimensionless parameters	96
5.4.2	Definition of water and colorant front positions	97
5.5	Discussion	100
5.5.1	Variation of the adsorption/desorption rates	100
5.5.2	Variation of the sorption capacity C_∞	101
5.5.3	Variation of y_0 and the initial moisture content	102
5.5.4	Variation of the evaporation rate	102
5.5.5	Line formation in dye-based inkjet printing on paper	102
5.5.6	Dye precipitation	103
5.5.7	Technological relevance	104
5.6	Summary and conclusions	105
6	Concluding remarks	107
6.1	Conclusions	107
6.2	Recommendations for future study	111
	Bibliography	115
	Summary	133
	Curriculum Vitae	137
	List of publications and conferences	139
	Acknowledgements	141

Chapter 1

Introduction

1.1 Fundamentals of ink-jet printing

In its essence, ink-jet printing consists of depositing a desired amount of liquid (ink) directly according to a computer-generated image onto a desired location of a substrate (usually paper, glass or polymers) by generating droplets of ink from an ink reservoir [1–3]. The non-contact nature offers great flexibility in terms of both the substrate and the ink, with virtually no limitations to the type of the substrate that can be used. The substrate can be rigid (metals, glass) or flexible (paper, polymers). Several types of inks are possible ranging from solvent based inks with molecularly dissolved dyes or solvent based inks with suspended pigments (rendering the ink as a colloidal suspension or emulsion) to UV gel inks, with cross-linked polymer particles, that deposit materials without the aid of a solvent. The ink-jet technology is now renowned for being simple, silent, fast, versatile, non-contact and a process with a completely digital control [1–5].

In the recent decades, there is a growing recognition that ink-jet technology offers cost-effective solutions for micro and nano fabrication of functional materials due to its ability to generate high-speed and high-resolution large area patterning, employing only a controlled and pre-determined amount of ink. Consequently, apart from its traditional use in printing text and images onto paper substrates, ink-jet printing has also become important for applications such as plastic electronics, nanotechnology and tissue engineering, to name a few [3]. The capability to fabricate functional features without the need for masks (as in lithographic processes) is particularly attractive for the additive manufacturing industry because of the reduction in the processing steps and thus reduction in waste, time and space of the manufacturing process.

However, for developing applied ink-jet printing techniques, it is paramount to attain an in-depth understanding of the fluid properties (such as surface tension and viscosity), the hydrodynamics that govern the various stages of the process, the (physico-chemical) interactions between the ink and the substrate

and, vitally, how these parameters and phenomena determine the quality of the deposition process. In general, the key challenges or areas requiring scientific study are

- How to form the drops of ink (drop generation)
- How to generate the motion of the formed drops (drop emission)
- How to control the drop to land on the required spot of the substrate (print control)
- How to cure (evaporation/UV curing) the deposited material to obtain the required features (deposited solution/material processing).

1.1.1 Droplet generation and emission

Drop formation can be achieved in several ways, some of which are,

- Fig. 1.1(a) shows a schematic of the continuous ink-jet technology (CIJT). In CIJT, the droplet is charged by an electrostatic field and passes through a deflection field which determines the location of drop landing. The unprinted drops are fed back for re-use. This method is suitable for printing with large droplet sizes or high throughput. The downside is however the low achievable resolution.
- Drop on demand (DoD) ink-jet printing offers higher efficiency than the CIJT method. Instead of continuously jetting drops, in the DoD method, the drops are only generated if the information to be printed requires so. Some types of DoD printing are as follows
- Fig. 1.1(b) shows a schematic of thermal ink-jet technology (TIJT). The drops are generated by heating a resistive element in the ink-chamber, causing vaporization of the ink leading to bubble formation and subsequently forcing a drop to be formed.
- Piezo-electric drop-on-demand ink-jet technology (PIJT) where a voltage is applied (generating an electric field) to distort the piezo-crystal which leads to a drop being formed.
- Electrostatic drop-on-demand ink-jet technology (EIJT) in which an electrostatic force is applied between an electrode and the nozzle to form drops.

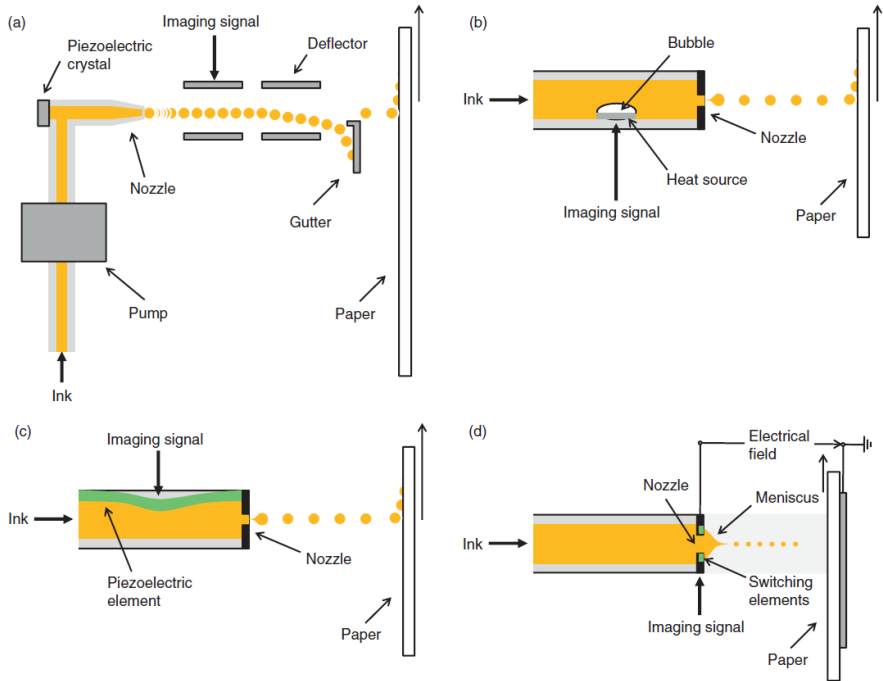


Figure 1.1: Schematic of (a) CIJ and DoD printing techniques (b) TIJ (c) PIJ and (d) EIJ. Image inspired from [1]

In the piezo-electric process, there is no restriction on the type of ink. This is in contrast to the thermal ink-jet technology where only inks that have a volatile component and can also withstand high temperatures are suitable. This limitation renders TIJT unsuitable for printing polymers. Moreover, water-based inks, where the solvent is water, are now in wide-spread use for printing onto various substrates, and especially onto porous substrates because of the advantages they offer from an environmental stand-point. While TIJT is most suitable for water-based inks, the fluid in the print-head undergoes thermal stresses [6] due to the high temperatures. This is not the case with PIJT, making it more versatile.

At the heart of all the above methods is the realization that the application of a pressure wave (acoustic energy) will break-up a liquid stream into discrete droplets of uniform size and shape (Rayleigh instability [1, 7]). Fig. 1.1(c) shows a schematic of the working of a piezo-electric ink-jet process. The applied voltage, the pulse duration (pulse-width) and the diameter of the nozzle control the size of the generated drops. The role of the pressure wave will be to primarily overcome the surface tension of the ink-air interface which tends to retain the

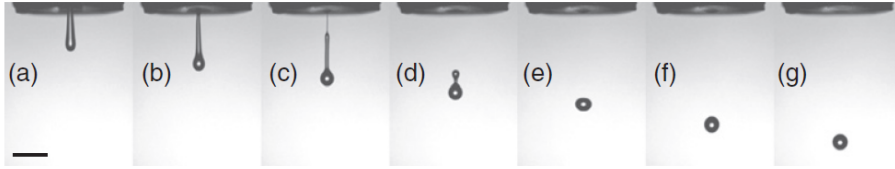


Figure 1.2: Stroboscopic images of an Ethylene glycol drop formation process from a slender liquid jet. The scale bar is $100\mu m$ in length. Image source [1]

ink at the orifice. Upon setting a voltage, the piezo element expands and a pressure wave propagates in two directions through the fluid, eventually expelling a stream of liquid which breaks up into discrete droplets in order to minimize the surface energy (again caused by the surface tension of the ink-air interface).

Fig. 1.2(a)-(g) show stroboscopic images of the various stages of an ideal droplet formation process from a slender column of ink. Initially, the ejected jet begins to adapt into a spherical shape to minimize its surface energy (figs. 1.2(a)-(c)).

During this time, the fluid is still attached to the nozzle through a filament. A drop pinch-off point occurs leading to the formation of the secondary or satellite drops inducing filament rupture, due to Laplace-pressure induced drainage of the filament-thickness into the secondary drop (fig. 1.2(d)). After which, coalescence of the primary and the secondary drops (fig. 1.2(e)) and thence post-coalescence oscillation occur (fig. 1.2(f)). A stable operating mode is then attained with the emitted drop hurtling towards the substrate (fig. 1.2(g)). Typical speed of the ejected liquid at the nozzle exit is $1 - 5 m/s$. The formed drop, however, impacts the substrate at considerably lower speeds. A drop with a typical size of $50 \mu m$ reaches its terminal velocity in approximately $10 ms$. The individual settings of the voltage, the pulse-width and frequency of deposition control the droplet emission process and is not universal for all liquids. Typically, the electrical signals are adjusted for each material system until the stable operating mode is achieved. It is often the case that very high voltages can cause large volumes of liquid being ejected (higher voltage however is a requirement for liquids with a high viscosity), and a too low-surface tension can cause the formation of several satellite drops leading to low resolution. In the context of this work, an ejection mode is considered stable if:

- A single droplet is formed after the jet-breaks up
- A larger primary drop and a smaller secondary drop are initially formed, but coalesce mid-air.

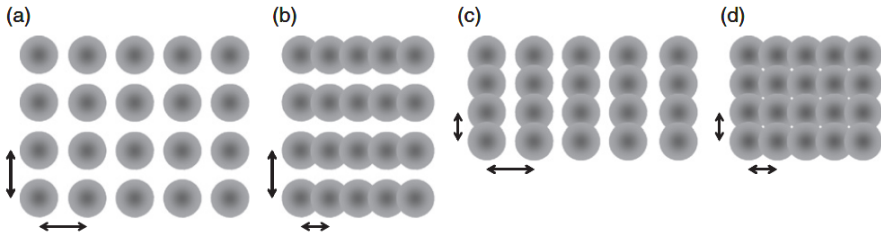


Figure 1.3: Schematic of variations in dot spacing (a) independent droplets are deposited due to large spacings (b) formation of horizontal lines when dot spacing is reduced (c) formation of transverse lines TJIT and (d) continuous structure when dot-spacing in both x and y directions are reduced. Image source [1]

- The secondary drop and the primary drop do not coalesce, but the secondary drop lands on the pool of the larger primary drop. This may cause fluctuations in the mass-flow rate as a function of the frequency of the deposition, so this mode should be avoided as much as possible.

Hourly or bi-hourly monitoring of the drop formation and emission processes can greatly enhance the accuracy, consistency and reproducibility of the ink-jet deposition experiments.

1.1.2 Print-control

Print-control depends on the distance between the nozzle and the substrate and on the speed of the ejected droplets. It also depends on the types of motion of the substrate. Certain applications require linear motion of the substrate, some others may require three dimensional motion with the help of precision (X-Y-Z) stages. Usually a working distance of not more than 5 mm is preferred between the nozzle apex and the substrate, because of antagonistic aerodynamic effects on the drops that could arise leading to inaccurate drop positioning. Both the thermal and the piezo-electric print-heads can be employed as side-shooters (with an angled mounting) or as roof-shooters.

The behaviour of droplets on substrate surfaces forming lines or films is of fundamental importance in ink-jet printing, because it determines the usefulness of the end product. Defect-free continuous structures are essential for many applications with functional materials. A crucial parameter is dot-spacing, i.e., the centre to centre distance of two drops on the substrate. Fig. 1.3(a)-(d) show the different types of structures that are formed depending on the way in which either the print-head or the substrate moves. If the droplet spacing is larger than the radius of the drops, discontinuous structures are formed. On

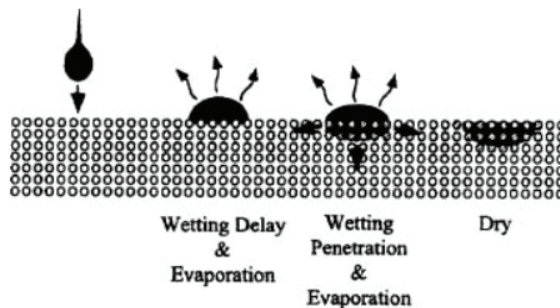


Figure 1.4: Various stages of the emitted drop's interaction with a porous substrate. Image taken from <https://www.imaging.org/site/IST/Resources>

the other hand, for dot spacing smaller than the radius of the drops, continuous features are produced. Moreover, for porous substrates, forming or printing lines are a convenient way to study competing phenomena such as solvent absorption and evaporation, as steady-state solvent distributions occur over sufficiently long printing duration. In the subsequent chapters, we will study the process of ink-jet deposition of lines in considerable detail as functions of both the speed in which the substrate moves underneath the print-head and the rate of droplet deposition.

1.1.3 Deposited solution/material processing

After drops are generated and emitted from the print-head, the final print-quality crucially depends on the interactions between the ink drops and the substrate. For porous substrates, the interplay of two simultaneous and competing phenomena of ink absorption and solvent evaporation governs the quality of the final print. When employing ink-jet to perform experiments, it is sought to first attain the stable operating mode (similar to fig. 1.2(g)) for different material systems. After the attainment of the stable mode, emphasis lies on gaining insights onto the transport processes that occur as ink-drops get redistributed into the paper substrate (imbibition). Fig. 1.4 shows a schematic of the different transport processes that occur after a drop impacts a porous substrate. Upon impact, depending on the type of coatings on the substrate and the nature of the additives present in the ink-drops, a wetting delay can be caused. The delay manifests as a slow rate of absorption. This delay is often detrimental as it leads to poor resolution and color density. Coated papers are therefore popular as they promote wetting. Typical aqueous inks also contain surface-active solutes (surfactants) which are well-known wetting agents. After

the droplet reaches its maximum extension, retraction begins with the droplet rapidly losing its mass [8]. Liquid is then re-distributed into the paper (in the lateral as well as in the vertical direction) under the driving influence of a pressure gradient between the wet and the dry zones (absorption/Darcy's law), with simultaneous evaporation of the solvent. Other added solutes, such as dyes or pigments, then bind to the substrate.

The goal of the research presented in this dissertation is to study the dynamics associated with spreading, imbibition and subsequent drying of water-based printing inks onto thin porous substrates (paper). We will disregard the impact process that occur on very short (ms) time-scales and focus rather on the absorption and evaporation regimes that occur on time-scales between $10^0 - 10^3$ seconds. Developing (experimental) methods to quantify and monitor solvent imbibition and evaporation on these time-scales is another important goal of this work. To this end, we will consider heat-transfer effects associated with the transport and evaporation of the solvent. Fig. 1.5 shows a scenario where a thin strand of paper is placed few centimetres away from a cup containing water. The water in the cup is colder than the ambient due to evaporative cooling. Despite no direct contact between the paper and the liquid, the end of the paper that is closest to the surface of the liquid shows an increase in temperature. Thus, we realize that insights on water- water vapor-paper interactions can be obtained by measuring and interpreting the temperature changes of the paper substrate. Both liquid imbibition (front-motion) and phase change effects such as evaporation and condensation translate into changes in the temperature of the paper, and can be exploited for robust process control, due to the poor heat capacity of paper leading to a measurable rise in temperature. In the subsequent chapters, we will delve deep, amongst other things, into the causes that lead to such interesting phenomena shown in Fig. 1.5.

Fig 1.6 shows a scanning electron microscope image of the internal structure of a typical printing paper. Paper is a porous material made up of cellulose fibres that are themselves permeable to varying degrees [9–11]. The fate of even a certain amount of solvent is to imbibe into the interior of the fibres leading to what is known as the residual liquid content. Thus, there is an internal transport mechanism that drives the solvent into the fibres, owing to the permeability of the fibres. The capacity of the paper fibres to imbibe moisture is important for the study of hygro-expansion of paper sheets and is also a chief factor in causing swelling or shrinkage of the media. While, imbibition facilitates drying of the solvent to impart the final features, it is only the beginning of the story. The final feature size can also be controlled by regulating the distribution of the solute (dyes, pigments, surfactants or their combination [12]) on the

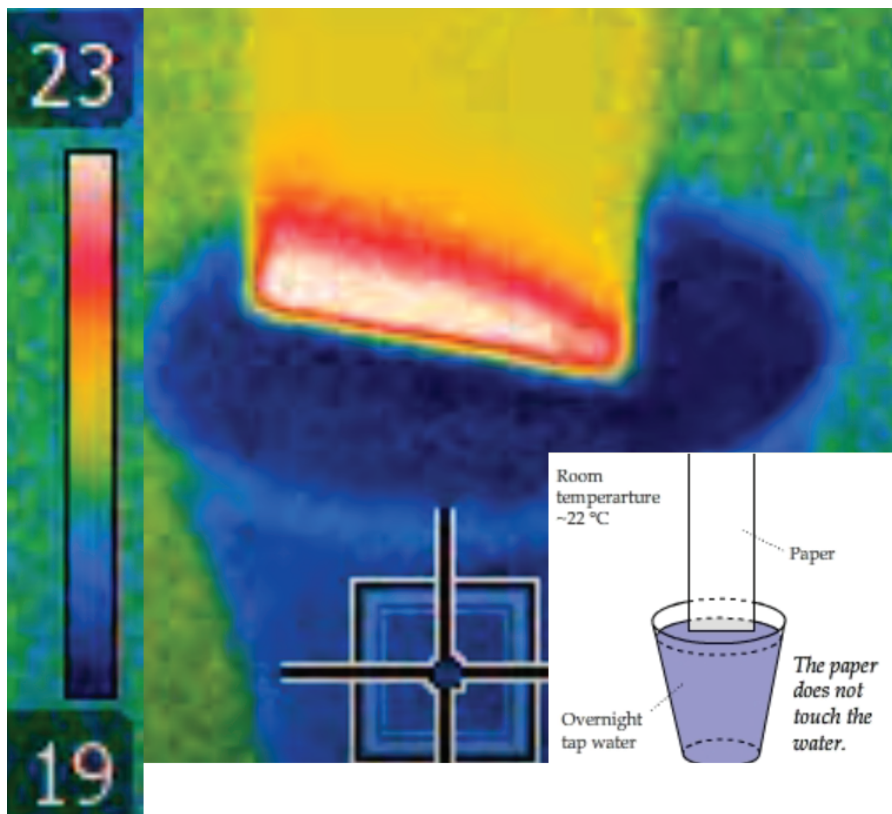


Figure 1.5: Potential of infrared thermography to monitor solvent-substrate (paper) interactions. The color bar on the left shows the temperature range in $^{\circ}\text{C}$. Image taken from <http://energy.concord.org/ir/>

substrate surface. It is beneficial to confine the distribution of the colorant to a narrow zone on the surface to obtain a smaller, more regular and intense print. Thus, adsorption of the solute onto the solid matrix (fibres) of the substrate, independently of the solvent distribution, becomes central to the quality of the deposition process. An effective color fixation occurs when the substrate has an opposite ionic charge to that of the ink-colorant [13]. In case of an anionic ink, a cationic substrate charge is required and vice-versa. Coatings on the paper substrate typically also aid in color fixation. In the forthcoming chapters, we will investigate the mechanisms by which the colorant fixes onto the substrate, along with quantifying the retardation of the solute (due to adsorption onto the fibres) behind the advancing solvent front. Furthermore, we will unravel the role of surface-active solutes (surfactants) on the moisture

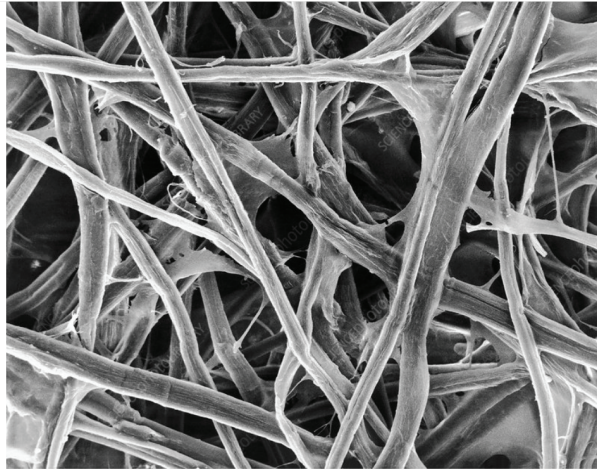


Figure 1.6: Scanning electron microscope image of the cellulose structures in printing papers. Image source <https://www.sciencephoto.com/media/874491/view/cellulose-fibres-print-paper-sem>

distribution profile. Due to the smaller sizes of the fibres in relation to the void-spaces (see fig. 1.6), the characteristic length scale that determines the visible light scattering or transmission efficiency through the paper becomes the pore-size. We will first understand how to employ optical light transmission signals to measure the moisture or solvent content and then it will be elucidated how the presence of surfactants alter the light-transmission intensities, and finally, how the altered signal can be used to interpret the role of surfactants in inducing moisture migration within the wet-zone. This migration occurs from zones of high surfactant concentration to purer zones of low or zero surfactant concentration.

1.2 Outline

Chapter 2 studies the problem of liquid imbibition into a porous medium and the thermal aspects accompanying this process. Infrared (IR) thermography is used to measure the temperature field of moving sheets of paper with a stationary wet-zone. Unraveling the response of the temperature field to the different speeds in which dry paper moves into the wet-zone, and the influence of the gas phase surrounding the paper on the temperature field are the key objectives. We will also develop a theoretical model which will enhance our interpretation of the measured data.

Subsequently, piezo-electric drop-on-demand ink-jet deposition of lines onto

thin porous media at various deposition parameters such as speed of the substrate and frequency of droplet deposition is studied. Optical transmission imaging is developed to measure the 2-D moisture content and IR thermography is applied to measure the ensuing temperature field of the paper. Another goal is also to develop a theoretical model to reproduce and rationalize the measured data (Chapter 3).

Chapter 4 extends the methods to study surfactant-laden material systems. Experiments with drop-casting and ink-jet deposition in transmission and reflection modes describe the light-media interaction that are crucially altered by the presence of surfactants. The experiments offer invaluable support to the dual-porosity model developed by the theoretical counterpart of this work.

Chapter 5 studies the problem of chromatographic separation of molecularly mixed dye-water solutions. Here the chief goal is to measure the lag of the dye behind the advancing solvent front in the context of ink-jet printing. Finally, some conclusions are drawn in the last chapter.

Each of the four main chapters (Chapter 2- Chapter 5) are divided into six main sections. Every chapter contains a local introduction (Section 1) which is followed by the description of experimental set-up or materials and methods (Section 2). Section 3 presents and describes the experimental results. Section 4 either develops (as in Chapter 2 and Chapter 3) or briefly introduces and outlines the theoretical model (as in Chapter 4 and Chapter 5) used to compare with and interpret the experimental results. The penultimate section discusses the results with particular emphasis on comparing the model and the experiments. Other relevant experimental phenomena are also discussed. In the last section, the results are summarized.

Chapter 2

Infrared thermography of sorptive heating of thin porous media

In this chapter, the imbibition of water from a stationary nozzle into thin, moving porous media that are suspended in air, as well as the accompanying evaporation and condensation processes are studied by means of systematic experiments and numerical simulations. Due to sorptive heating and the latent heat associated with the phase change processes, the temperature of the porous medium becomes non-uniform. We have measured the temperature distributions using infrared thermography as a function of substrate speed. Moreover, a numerical model coupling Darcy flow and heat transfer in the thin porous medium with gas flow, heat and water vapor transport in the surrounding gas phase is developed. The numerical simulations reproduce the measurements very well and point at an intricate buoyancy-induced gas-phase convection pattern.

2.1 Introduction

Imbibition and drying processes of thin porous media are of paramount importance in technological applications such as paper making, [14–21] printing [22–41] and coating. [42–50] Owing to the strong absorption bands of water in the near infrared (NIR) spectral region, NIR spectroscopy has been used for moisture content analysis during paper making and drying processes. [51–61] Similarly, infrared (IR) thermography has been used as an indirect method for the determination of moisture distributions in paper. [62–71]

Aslannejad *et al.* have used IR thermography to characterize the temperature rise at the wetting front accompanying the vertical imbibition of water into a sheet of dry paper driven by capillary rise. [71] Evaporation and condensation processes were eliminated by means of impermeable plastic sheets- that were contacting the paper on both sides. They measured temperature amplitudes for a single sheet of paper up to approximately 1°C. The authors concluded from their results that evaporation/condensation processes do not significantly

contribute to temperature changes in *bulk* porous media.

Using IR thermography, we have studied temperature changes accompanying aqueous imbibition into *thin* porous media that are in direct contact with the ambient atmosphere. Our motivation is to gain insight into the thermal aspects of solvent imbibition and subsequent drying of inkjet printed sheets. For paper initially equilibrated to an ambient relative humidity of about 40%, we measured temperature increases up to 3°C. As we show, the recondensation of evaporated water by far exceeds the sorptive heating at low substrate speeds and cannot be disregarded.

The geometry of our setup resembles that of an automatic scanning absorptometer. [72, 73] The important differences are that the paper is suspended in air and that the constant substrate speed is slow. Thus, imbibition in the thickness direction of the paper sheets can be considered instantaneous compared to the time required for attaining a quasi-steady moisture distribution in the horizontal direction. An IR camera captures the temperature field of the moving porous substrate. Besides conducting systematic experiments we also developed a numerical model for one-dimensional flow and heat transfer in the substrate coupled to a two-dimensional model for flow as well as heat and vapor transport in the adjacent gas phase.

The following section contains a detailed description of the experimental setup and the material properties of the paper samples. In Section 2.3 we describe the experimental results, which are compared with and serve as a validation for the numerical results that are discussed in Section 2.5. In Section 2.4 we present the theoretical model based on 1D unsaturated single-phase flow and heat transfer in a thin porous medium, the 2D equations for gas flow, water vapor and heat convection and diffusion in the adjacent gas phases as well as the relevant boundary and interfacial conditions.

2.2 Experimental

Figure 2.1(a,b) shows a schematic and a photograph of the experimental set-up. It consists of a sheet of paper mounted 6 mm above an aluminum base plate fastened onto a motorized translation stage (Newport, model UTS 100CC). A stationary brass injector with 3 supply holes of diameter 1 mm is connected to a motorized syringe pump (KD Scientific, model Gemini 88 plus) and supplies water onto the suspended sheet of paper. The gap-distance between the bottom surface of the injector and the paper surface was maintained at approximately 0.5 mm. The constant speed of motion U_{sub} of the substrate is varied in the range 0.2 – 3 mm/s. The dimensions of the substrates are on the order of 80 ×

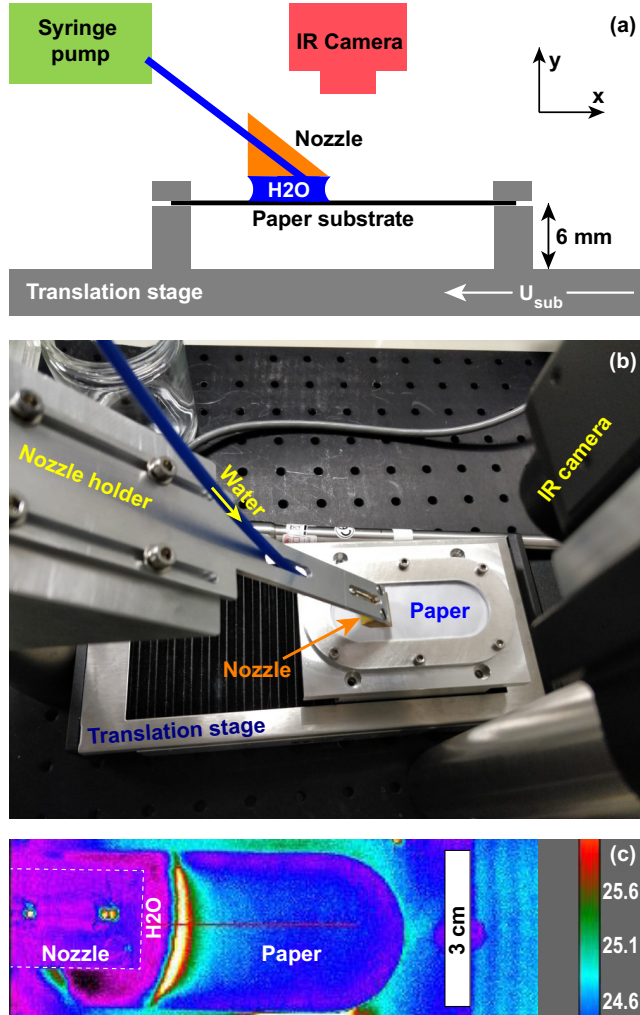


Figure 2.1: (a) Sketch and (b) photograph of the experimental setup. (c) A typical temperature distribution for a substrate speed of $U_{sub} = 1 \text{ mm/s}$.

$30 \times 0.1 \text{ mm}$. A long-wave infrared camera (FLIR, model A35sc, 320×256 pixels, spectral sensitivity range $7.5 - 13.5 \mu\text{m}$) is used to determine the temperature field $T(x, z, t)$ of the substrate upon injection of water. We calibrated the temperature data by placing paper on a hotplate maintained at a defined temperature. We could not detect a significant effect of the moisture content on the emissivity of the porous medium.

The volume of water on the paper is kept approximately constant in time by adjusting a constant flow rate using the syringe pump, which depends on

the substrate speed and which compensates for the loss due to absorption and evaporation and helps maintain stationary boundary conditions. The water was kept at room temperature, i.e. approximately $(23 \pm 1)^\circ\text{C}$. The position $x = 0$ corresponds to the apex of the nozzle, $y = 0$ denotes the horizontal plane of the paper substrate and $t = 0$ corresponds to the time when the imbibition front has become approximately steady.

Figure 2.1(c) shows a typical temperature map acquired approximately 10 s after injection of water. The ambient temperature and the relative humidity (RH) are measured during the experiments (General Electric, model RH2350 plus). Experiments have been performed at ambient conditions with room temperature varying in the range $23 - 27^\circ\text{C}$ and RH varying in the range $40 - 60\%$.

The paper types studied comprise typical coated and calendered (Mondi, DNS HSI CF, porosity 41.3%) and uncoated, uncalendered (Mondi, DNS HSI NF, porosity 35.8%) printing papers. We used demineralized water for our experiments (BWT Ministil P-12, electrical conductivity $1.0 \mu\text{S}/\text{cm}$).

2.3 Experimental results

Figure 2.2(a,b) shows measured temperature distributions $T(x, t)$ for the uncoated paper type and with the substrate moving at 0.2 and 1 mm/s, respectively, along the negative x -axis. Far away from the nozzle the temperature remains at ambient level. Close to the nozzle, T falls below ambient temperature due to evaporative cooling from a region where a liquid water meniscus resides on top of and is in contact with the porous substrate. Its precise extension depends on the wetting properties of the paper, the volume of water underneath the nozzle prior to commencing the substrate motion, the vertical gap separation of the nozzle from the paper and the settings of the syringe pump. Generally it ranges between about $0.5 - 3 \text{ mm}$. At a certain distance from the nozzle, a temperature maximum occurs that exceeds ambient level by $2 - 3 \text{ K}$, which is caused by recondensation of water vapor on dry regions of the substrate as well as sorptive heating due to moving a dry substrate into a stationary wet zone.

It can be seen from both figures that the position of the maximum of the temperature curve does not change strongly in time implying that the system is in a quasi-steady state. The differences in amplitude and width of the observed $T(x, t)$ profile are caused by the different substrate speeds. For a higher value of U_{sub} , the $T(x, t)$ profile becomes narrower. We quantify the shape of the curves by the two parameters ΔT_{max} and Δx_{max} , which correspond to the

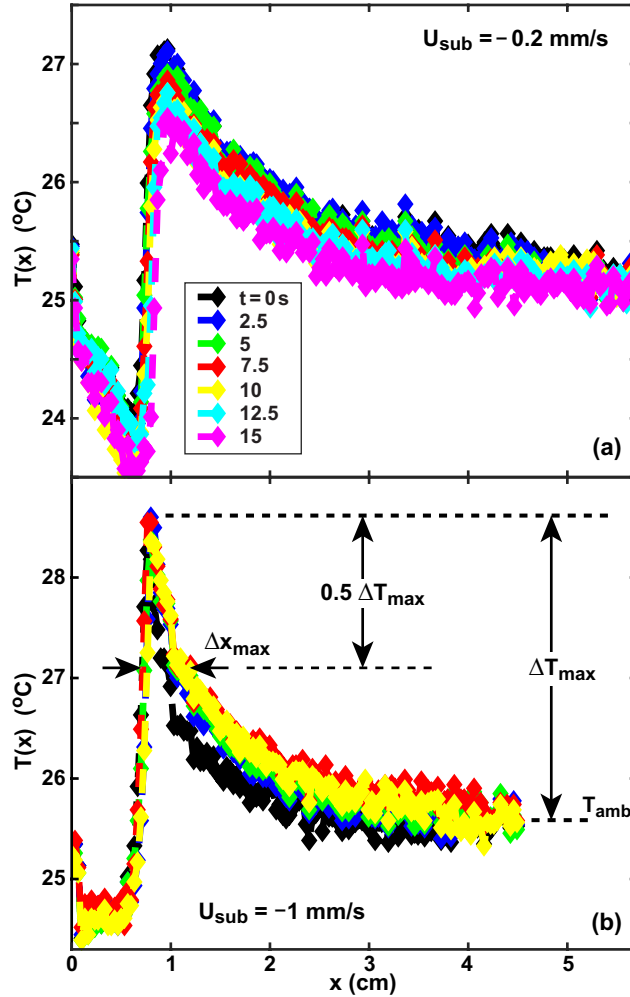


Figure 2.2: Measured temperature profiles $T(x, t)$ for two values of $U_{sub} = -0.2$ and -1 mm/s at a relative humidity $r_h = 0.47$ for uncoated paper.

maximum temperature rise above ambient and its full width at half maximum relative to ambient conditions.

Figure 2.3(a) shows the variation of ΔT_{max} with substrate speed U_{sub} for two different types of paper along with the result of the model introduced in section 2.4. A maximum is observed for a speed of $U_{sub} \approx 1$ mm/s. At much lower or higher substrate speeds, ΔT_{max} seems to approach a constant. There is good agreement between the experiments and the model within experimental scatter. In Fig. 2.3(b) the width Δx_{max} of the temperature peaks is plotted as a

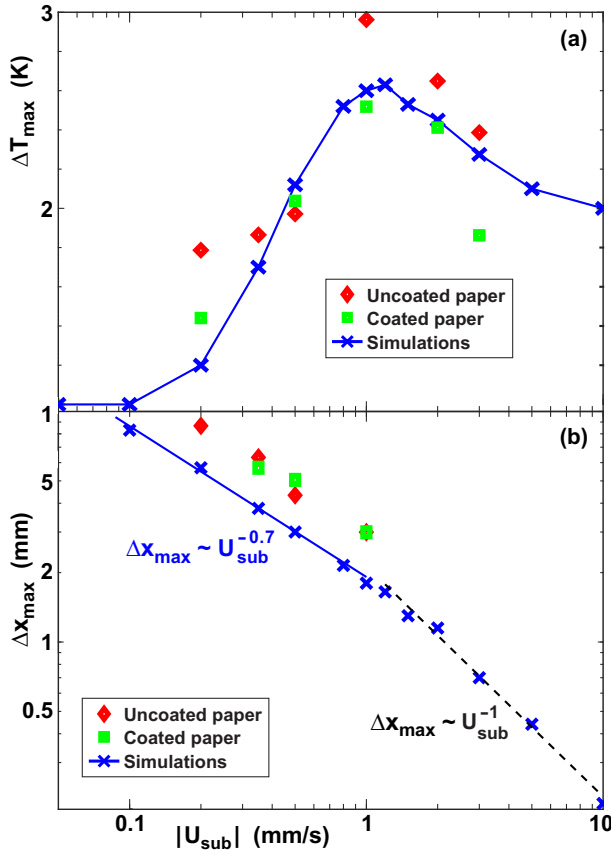


Figure 2.3: Variation of (a) ΔT_{max} and (b) Δx_{max} with substrate speed U_{sub} . Diamond and square symbols correspond to experimental data obtained with the uncoated (porosity 0.36, $r_h = 46.5\%$) and the coated paper type (porosity 0.41, $r_h = 52.5\%$). Crosses correspond to numerical simulations obtained for a porosity of 0.4 and $r_h = 46\%$. The solid and dashed lines in (b) correspond to powerlaw fits $\Delta x_{max} \sim U_{sub}^{-0.7}$ and $\sim U_{sub}^{-1}$ of the numerical data, respectively.

function of substrate speed U_{sub} . The symbols represent experimental data, the solid and dashed lines correspond to powerlaw relations $\Delta x_{max} \sim |U_{sub}|^{-0.7}$ and $\sim |U_{sub}|^{-1}$, respectively. The simulations reproduce the trend of the measurements very well.

2.4 Theoretical model

We have developed a continuum scale model for one-dimensional (1D) water imbibition into unsaturated thin porous media including evaporation/condensation and heat transfer effects that is coupled to a two-dimensional (2D) model for gas-phase convection, vapor transport and heat transfer in the ambient atmosphere above. These fully-coupled set of equations are solved using the finite-element software Comsol Multiphysics 5.3a.

2.4.1 Transport in the thin porous medium domain

Our starting point is the single-phase transport equation for liquids in unsaturated porous media [74]

$$\phi \rho_w \frac{\partial S_w}{\partial t} + \nabla \cdot (\rho_w \langle \vec{\mathbf{u}} \rangle) = 0 , \quad (2.1)$$

where ϕ is the porosity, $S_w = V_{liq}/(\phi V)$ is the degree of saturation, i.e. the ratio of the liquid volume V_{liq} contained in a volume element V of the porous medium and the volume available to fluid ϕV . Moreover, ρ_w is the mass density of liquid water and $\langle \vec{\mathbf{u}} \rangle$ the Darcy velocity

$$\langle \vec{\mathbf{u}} \rangle = - \frac{K_s K_{rw}(S_w)}{\mu_w} \frac{dp_c}{dS_w} \nabla S_w , \quad (2.2)$$

where $K_{rw}(S_w)$ is the relative permeability of water, K_s is the intrinsic permeability of the porous medium, μ_w is the dynamic viscosity of water and p_c is the capillary pressure. We assume that p_c varies with S_w according to the Van Genuchten relation [75, 76]

$$p_c(S_w) = p_g (S_w^{(-1/m_g)} - 1)^{(1/n_g)} , \quad (2.3)$$

where p_g , m_g and n_g are adjustable parameters that depend on the average pore size and the pore size distribution. Since we only consider imbibition with a monotonic water distribution, we need not take hysteretic effects into account. As is commonly assumed, we set $m_g = 1 - 1/n_g$. Aslannejad *et al.* [77, 78] determined typical values of p_g , m_g and n_g for coated and uncoated printing paper. We assumed that the relative permeability is given by the Van Genuchten relation [75, 76]

$$K_{rw}(S_w) = S_w^{k_c} \left[1 - \left(1 - S_w^{m_g} \right)^{m_g} \right]^2 , \quad (2.4)$$

where $k_c = -0.4$ is a connectivity factor, which we treated as a fitting parameter.

In using Eq. (2.1) as the transport equation for the imbibition of water into the porous medium, the presence of air is neglected. This is justified by the large viscosity ratio $\mu_w/\mu_{air} \approx 50$ and the small thickness of the porous medium. Equation (2.1) applies to systems without mass loss. In our case, evaporation and condensation effects will induce changes in the local saturation, which depend on the local temperature. This requires addition of a source and sink term J in Eq. (2.1) and to simultaneously solve for heat transfer [79]

$$\phi \rho_w \frac{\partial S_w}{\partial t} + \nabla \cdot (\rho_w \langle \vec{\mathbf{u}} \rangle) = J, \quad (2.5)$$

$$(\rho c_p)_{av} \frac{\partial T}{\partial t} + \rho_w c_{p,w} \langle \vec{\mathbf{u}} \rangle \cdot \nabla T = \nabla \cdot (k_{av} \nabla T) + \dot{Q}, \quad (2.6)$$

where \dot{Q} accounts for heat generation processes in the bulk (unit W/m³). The average of the product of mass density and specific heat capacity at constant pressure is defined as [79]

$$(\rho c_p)_{av} \equiv \phi S_w \rho_w c_{p,w} + \phi(1 - S_w) \rho_{air} c_{p,air} + (1 - \phi) \rho_s c_{p,s}. \quad (2.7)$$

Similarly, the average thermal conductivity is assumed to be

$$k_{av} \equiv \phi S_w k_w + \phi(1 - S_w) k_{air} + (1 - \phi) k_s. \quad (2.8)$$

Here the subscripts ‘s’ and ‘air’ refer to the intrinsic properties of the solid [80–82] (not including the pore space) and air, respectively. In practice, the terms containing properties of air can be neglected, owing to the low numerical values of k_{air} and ρ_{air} .

We now transform Eqs. (2.5,2.6) into a coordinate system moving with speed U_{sub} into the negative x -direction and perform an average in the y -direction across the thickness t_p of the porous medium, which yields the one-dimensional evolution equations

$$\phi \rho_w \frac{\partial S_w}{\partial t} + \frac{\partial}{\partial x} (\rho_w \langle u \rangle - \phi \rho_w S_w U_{sub}) = j, \quad (2.9)$$

$$\begin{aligned} (\rho c_p)_{av} \frac{\partial T}{\partial t} + [\rho_w c_{p,w} \langle u \rangle - (\rho c_p)_{av} U_{sub}] \frac{\partial T}{\partial x} = \\ = \frac{\partial}{\partial x} \left[k_{av} \frac{\partial T}{\partial x} \right] + \dot{q}. \end{aligned} \quad (2.10)$$

Information on the source and sink terms j and \dot{q} will be provided in Section 2.4.3.

2.4.2 Gas-phase domain

In the gas-phase domain, the incompressible Navier-Stokes equation

$$\rho_{gas} \left(\frac{\partial \vec{u}}{\partial t} + \vec{u} \cdot \nabla \vec{u} \right) = -\nabla p + \rho_{gas} \vec{g} + \mu_{gas} \nabla^2 \vec{u} \quad (2.11)$$

is solved, as the relevant speeds are much smaller than the speed of sound. Here, ρ_{gas} is the mass density of water vapor-air mixtures, \vec{u} the velocity, p is the pressure and \vec{g} is the gravitational acceleration. We assumed that the viscosity of the gas phase μ_{gas} is unaffected by the water vapor concentration and substituted $\mu_{air} = 1.84 \cdot 10^{-5}$ Pa-s. Gas flow is driven by the motion of the translation stage and by buoyancy effects, both as water vapor is lighter than air and the temperature is non-uniform. Consequently, we need to solve a coupled system of equations for gas flow, heat transfer and mass transfer.

For the time evolution of the water vapor density ρ_{H_2O} in the gas phase, the convection-diffusion equation

$$\frac{\partial \rho_{H_2O}}{\partial t} + \vec{u} \cdot \nabla \rho_{H_2O} = \nabla \cdot (D_{H_2O} \nabla \rho_{H_2O}) \quad (2.12)$$

is solved. Here, $D_{H_2O} = 2.8 \cdot 10^{-5} \text{m}^2/\text{s}$ is the diffusivity of water vapor in air at room temperature ($T = 25^\circ\text{C}$). For the dynamics of the gas temperature distribution, we solve the heat transfer equation

$$(\rho c_p)_{air} \frac{\partial T_{gas}}{\partial t} + (\rho c_p)_{air} \vec{u} \cdot \nabla T_{gas} = \nabla \cdot (k_{air} \nabla T_{gas}), \quad (2.13)$$

where we have substituted thermal properties of dry air [$\rho_{air} = 1.18 \text{kg}/\text{m}^3$, $c_{p,air} = 1.005 \text{kJ}/(\text{kg}\cdot\text{K})$, $k_{air} = 0.0253 \text{W}/(\text{m}\cdot\text{K})$], as the ones for humid air do not differ appreciably.

We treat the mixtures of water vapor and air as an ideal gas. The dependence of the saturated vapor pressure on temperature is determined from the following empirical relation [83]

$$p_{sat}(\text{Pa}) = 610.78 \exp \left(17.2694 \frac{T(^{\circ}\text{C})}{T(^{\circ}\text{C}) + 238.3} \right). \quad (2.14)$$

Using the ideal gas law, the mass density of water vapor is determined as

$$\rho_{H_2O} = p_{H_2O} M_W / (RT), \quad (2.15)$$

where $R \equiv 8.314472 \text{J}/(\text{mol}\cdot\text{K})$ is the universal gas constant and p_{H_2O} the partial pressure of water vapor. The density of water vapor-air mixtures are

determined using Dalton's law as

$$\begin{aligned}\rho_{gas} &= \frac{p_{dry\ air}}{R_{dry\ air}T} + \frac{p_{H_2O}}{R_{H_2O}T} \\ &= \frac{p_{amb}}{R_{dry\ air}T} \left[1 - \frac{p_{H_2O}}{p_{amb}} \left(1 - \frac{R_{dry\ air}}{R_{H_2O}} \right) \right],\end{aligned}\quad (2.16)$$

where $p_{amb} = 101300$ Pa is the ambient pressure, $R_{dry\ air} = R/M_W = 287.04$ J/(kg-K) and $R_{H_2O} = 461.5$ J/(kg-K) are the specific gas constants of dry air and water vapor, respectively.

2.4.3 Evaporation rate, sorptive heating and evaporative cooling

We assume that the evaporation process is diffusion-limited, which is appropriate for near-ambient conditions. Consequently, the rate of mass loss j from the paper is given by

$$j = \frac{D_{H_2O}}{t_p} \frac{\partial \rho_{H_2O}}{\partial y} . \quad (2.17)$$

where $t_p \approx 100$ μm is the paper thickness. The heat source/sink term \dot{q} is given by [84–88]

$$\begin{aligned}\dot{q} &= j \frac{L_w}{M_w} + \frac{k_{air}}{t_p} \frac{\partial T_{gas}}{\partial y}(y=0) - \frac{h_N}{t_p} (T - T_{amb}) \\ &\quad - \rho_w \phi \left(\frac{\partial S_w}{\partial t} - U_{sub} \frac{\partial S_w}{\partial x} \right) \Delta H_s ,\end{aligned}\quad (2.18)$$

where $L_w = 44.203$ kJ/mol is the enthalpy of evaporation of water and $h_N = k_{air}/d = 4.33$ W/m² is a heat transfer coefficient, where $d = 6$ mm is the height of the suspended paper sheet above the Al base plate.

The first term in Eq. (2.18) proportional to j describes heat removal or addition due to water evaporation or condensation. The second and third terms represent Newtonian cooling due to the Al baseplate and the conductive thermal coupling with the 2D domain. The last term refers to sorptive heating effects due to dynamic changes in S_w as well as the motion of dry paper into a wet zone. We represent the differential heat of wetting [89–95] ΔH_s by the empirical equation

$$\Delta H_s = C_1 \exp(-C_2[MC]) \quad (2.19)$$

with fitparameters $C_1 = 1500$ kJ/kg and $C_2 = 25$. Here,

$$[MC] = \frac{\phi \rho_w}{(1 - \phi) \rho_s} S_w \quad (2.20)$$

is the moisture content (units: kg water per kg dry paper).

The coupling of the paper domain to the gas domain is done by assuming continuity of temperature, i.e. $T_{gas}(x, y = 0, t) = T(x, t)$ as well as assuming a vapor density $\rho_{H_2O}(x, y = 0, t)$ determined by the relevant vapor sorption isotherm (VSI) of paper. We assume that the VSI is given by a Guggenheim-Anderson-de Boer (GAB) isotherm, which can reproduce the sorption behavior of cellulose-based materials well [96–100]

$$[MC] = \frac{M_0 C_g k a_w}{(1 - k a_w)(1 + (C_g - 1)k a_w)} . \quad (2.21)$$

Here a_w is the water activity and $M_0 = 0.061$, $C_g = 18.647$ and $k = 0.85$ are typical fit-parameters for paper. [96–100] In local thermodynamic equilibrium, the water activity is equal to the local relative humidity r_h

$$a_w = r_h \equiv \frac{\rho_{H_2O}(x, y = 0, t)}{\rho_{sat}[T(x, y = 0, t)]} , \quad (2.22)$$

where ρ_{sat} is defined by Eqs. (2.14,2.15). Equations (2.20,2.21) couple ρ_{H_2O} with S_w , which closes our set of equations.

2.4.4 Initial and boundary conditions

In this section, the relevant initial and boundary conditions for the coupled domains are described. Figure 2.4 shows a schematic of the computational domains and the relevant boundary conditions (BCs).

Paper domain

We assume that at $t = 0$ the moisture content of the paper is in equilibrium with ambient conditions, i.e. the initial value of saturation $S_w(t = 0)$ is determined by Eq. (2.20) and the sorption isotherm Eq. (2.21)

$$S_w(t = 0) = \frac{(1 - \phi)\rho_s}{\phi\rho_w} [MC](a_w = r_h) . \quad (2.23)$$

The initial temperature is T_{amb} . The BCs are assumed to be $S_w(x = 0) = S_l$, which is close to 1, and $S_w(x = L_2) = S_r$, which is set equal to $S_w(t = 0)$. The thermal BCs are $T(x = L_1) = T(x = 0) = T_{amb}$. Here, $x = 0$ and L_1 are the position of the left and right domain boundaries in Fig 2.4. The latter is sufficiently remote from the nozzle such that it does not affect the temperature distribution for small x .

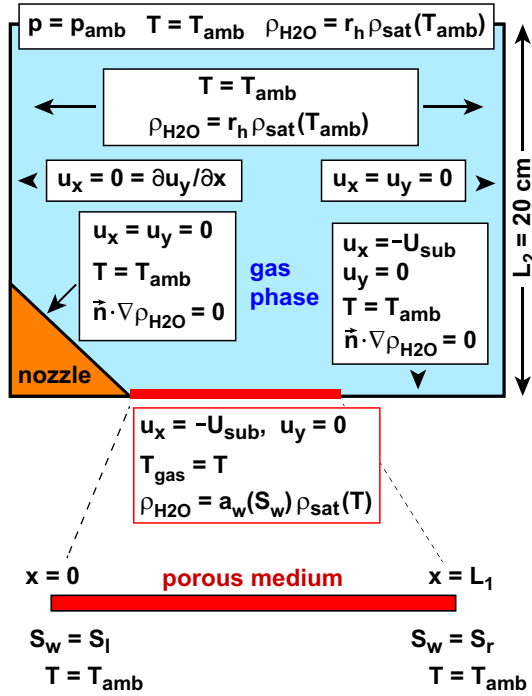


Figure 2.4: Schematic of the computational domains and the boundary conditions for the 2D gas-phase and the 1D porous medium domains.

Gas-phase domain

The initial gas velocity is set to zero. The initial vapor concentration and temperature correspond to ambient conditions

$$\vec{u}(x, y, t = 0) = 0, \quad (2.24)$$

$$p(x, y, t = 0) = p_{amb} \quad (2.25)$$

$$\rho_{gas}(x, y, t = 0) = r_h \rho_{sat}(T_{amb}), \quad (2.26)$$

$$T_{gas}(x, y, t = 0) = T_{amb} . \quad (2.27)$$

The BCs for the top boundary ($y = L_2$) represent ambient conditions

$$p(x, y = L_2, t) = p_{amb}, \quad (2.28)$$

$$\rho_{gas}(x, y = L_2, t) = r_h \rho_{sat}(T_{amb}), \quad (2.29)$$

$$T_{gas}(x, y = L_2, t) = T_{amb} . \quad (2.30)$$

The BCs for the lateral boundaries are

$$u_x(x, y, t) = 0 = \partial u_y / \partial x = 0 \quad (\text{left}), \quad (2.31)$$

$$u_x(x, y, t) = 0 = u_y \quad (\text{right}), \quad (2.32)$$

$$\vec{\mathbf{n}} \cdot \nabla \rho_{gas} = 0, \quad (2.33)$$

$$T_{gas}(x, y, t) = T_{amb}, \quad (2.34)$$

i.e. no-slip and no-penetration BCs for the velocity and no-adsorption BCs for the water vapor.

2.5 Discussion

2.5.1 Moisture transport in the paper substrate

Figure 2.5(a) shows numerical simulations of the degree of saturation $S_w(x)$ for three values of U_{sub} and the same conditions as in Fig. 2.3. The position $x = 0$ corresponds to the apex of the nozzle (or, more precisely, the extension of the water meniscus ahead of the nozzle). For higher substrate speeds, the penetration distance x_d of the wetting front decreases and the spatial saturation gradients $\max(|\partial S_w / \partial x|)$ increase. The parameter x_d is defined as the x -coordinate where $S_w = 0.4$. The inset shows x_d as a function of U_{sub} , which is well-represented by a powerlaw $x_d \sim |U_{sub}|^{-1}$ (solid line) for $|U_{sub}| > 0.1$ mm/s. In other words, U_{sub} controls how far ahead of the nozzle the wetting front can propagate for high substrate speeds. There is a second regime for very slow speeds $|U_{sub}| < 0.1$ mm/s, where evaporative mass loss rather than convection controls the position of the wetting front and where x_d becomes independent of U_{sub} .

Figure 2.5(b) shows the temperature change $\Delta T_\infty(x) \equiv T(x, t \rightarrow \infty) - T_{amb}$ at steady state for the same conditions as in Figs. 2.5(a) and 2.3. The curves look qualitatively similar to the experimental temperature profiles in Fig. 2.2. Close to the nozzle, there is a colder zone $\Delta T < 0$ due to evaporative cooling. Further ahead there is a local temperature maximum $\Delta T_{max} > 0$, after which ΔT diminishes to zero. The position of the temperature maximum occurs at relatively low values of S_w , i.e. close to the wetting front. Its presence is caused by two separate effects:

- Recondensation of water vapor that evaporated from the more saturated region closer to the nozzle. The condensation is accompanied by the liberation of latent heat. It is affected by the convective and diffusive transport of water vapor in the gas-phase domain.

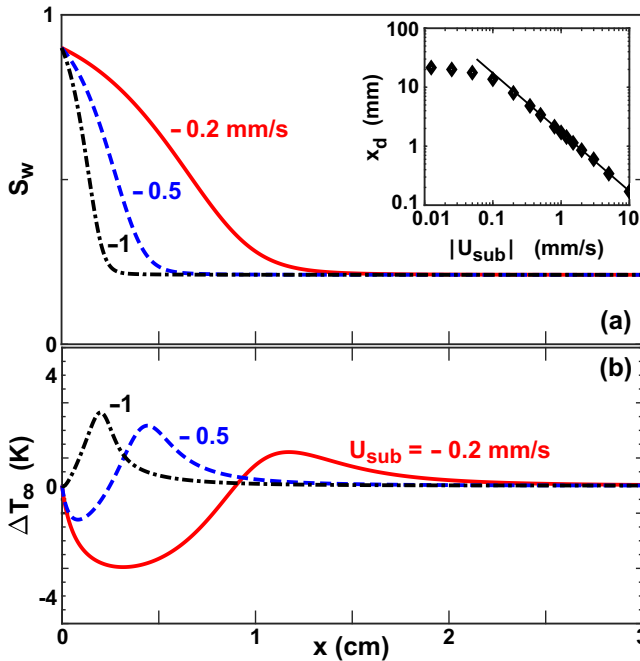


Figure 2.5: (a) Degree of saturation S_w and (b) temperature change ΔT_∞ as a function of position x for different values of U_{sub} at quasi-steady state. Inset: location of the imbibition front x_d defined as the x -coordinate where $S_w = 0.4$ as a function of U_{sub} . The solid line is a powerlaw fit $x_d \sim |U_{sub}|^{-1}$.

- The heat of wetting ΔH_s due to the steady motion of dry substrate material into the stationary wet zone, which becomes more pronounced at lower values of S_w [see Eq. (2.19)].

According to Eq. (2.18), the position of the maximum of \dot{q} is determined by the product of $\partial S/\partial x$ and ΔH_s , as far as sorption is concerned. Since ΔH_s decays with increasing S_w , the maximum is located close to the wetting front rather than at the inflection point of $S(x)$. The contribution from vapor condensation is contained in the term proportional to $j(x)$, which is controlled by the vapor convection and diffusion. Interestingly, the non-uniformity of the saturation curve S_w in Fig. 2.5(a) induces a built-in horizontal gradient in ρ_{H_2O} via the interfacial condition Eq. (2.22). One expects also the condensation-induced heat flux to reach a maximum close to the wetting front, because it is the position closest to the source where substantial condensation can occur. However, the spatial distribution will be broader due to the diffusive and convective vapor transport mechanisms. The superposition of the two contributions results in

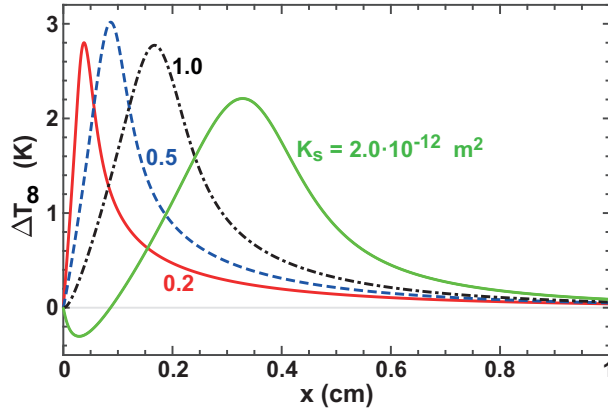


Figure 2.6: Quasi-steady-state temperature distribution $\Delta T_{\infty}(x)$ for $U_{sub} = -1$ mm/s and different values of the absolute permeability K_s .

a peak close to the wetting front with a relatively slow decay in the positive x -direction, consistent with Figs. 2.2 and 2.5(b).

Figure 2.6 illustrates the influence of the substrate permeability parameter K_s on the temperature profiles. A larger value of K_s implies that the wetting front extends further, i.e. leads to a larger value of x_d . As both $\partial S_w / \partial x$ decreases and the gas-phase transport becomes impaired because it has to cover a larger distance, the temperature profile becomes broader and decreases in amplitude for large K_s .

Figure 2.7 shows the effect of the ambient humidity on the maximum temperature change ΔT_{max} . Since ΔH_s diminishes for higher values of $[MC]$ and since less water can condense on more saturated paper, ΔT_{max} goes to zero for r_h approaching 1. For the same reason, ΔT_{max} increases significantly for dry paper equilibrated with a low humidity atmosphere in the limit $r_h \rightarrow 0$.

2.5.2 Convection-diffusion in the gas phase

In the gas-phase, convection is induced by the motion of the substrate and by buoyancy, as water vapor is lighter than air and the temperature is non-uniform. The convection influences the water vapor distribution and thus the diffusion-limited evaporative mass transfer into and out of the 2D domain. Consequently, it affects both the amplitude and the width of the temperature profile of the porous domain. Figure 2.8 shows contour plots of the concentration of water vapor in air for four different values of U_{sub} . The lateral extent of the region with enhanced vapor concentration is determined primarily by the width of the wet zone x_d and decreases for increasing $|U_{sub}|$.

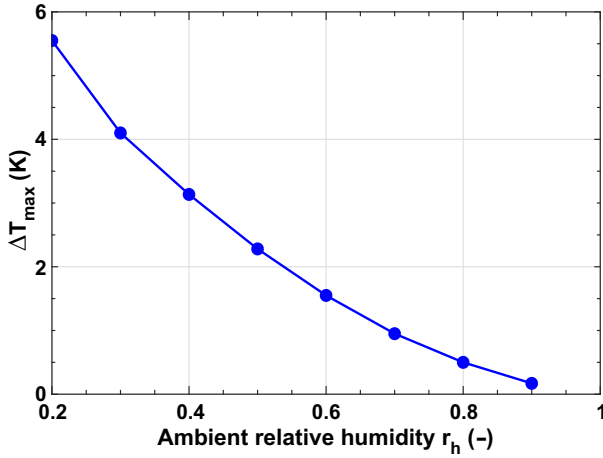


Figure 2.7: ΔT_{max} as a function of the ambient relative humidity r_h for $U_{sub} = -1$ mm/s.

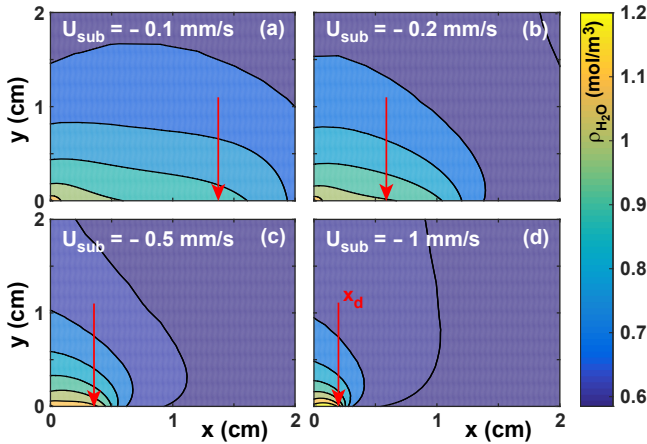


Figure 2.8: Contour plots of the water vapor concentration ρ_{H_2O} in the gas phase for four different values of U_{sub} . The vertical red arrows indicate the values of x_d .

Figure 2.9 presents contour plots of the x -coordinate of the gas-phase velocity $u_x(x, y)$. Close to the substrate, the convection velocity is determined by the BC $u_x = U_{sub} < 0$. Above the substrate, a convection roll is observed. Surprisingly, the speed of convection in the gas phase by far exceeds the substrate speed. Moreover, while the gas velocity is aligned with the direction of substrate motion in the region immediately above the substrate for $|U_{sub}| \geq 0.4$ mm/s, a change of direction is visible in Fig. 2.9(a,b) close to the nozzle exit for $|U_{sub}| \leq 0.4$ mm/s. This flip is due to the antagonistic effects of the thermally-

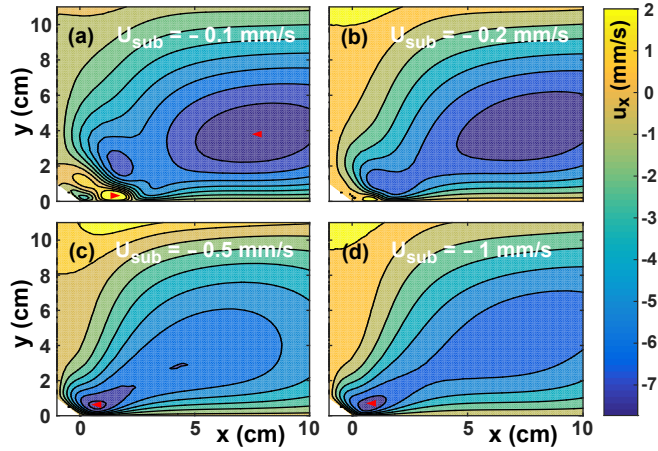


Figure 2.9: Contour plots of the horizontal gas velocity component u_x for four different values of U_{sub} .

induced and water-vapor-concentration-induced buoyancy terms. A high water vapor concentration occurs primarily near the nozzle exit, which favors a rising velocity. Together with the leftwards substrate motion, a convection roll rotating clock-wise is induced. The same holds for the thermal buoyancy induced by the temperature maximum. For low speeds, however, both the extension of the wet zone x_d and the degree of evaporative cooling significantly increase. The corresponding thermally-induced buoyancy now favors a falling velocity and thus a locally counter-clockwise rotation.

2.5.3 Scaling analysis

The scaling analysis of this problem is challenging, as five coupled partial differential equations belonging to two different domains are involved. Nevertheless it is possible to rationalize the behavior of the temperature distribution in the limits of very high and very low substrate speeds.

For high $|U_{sub}|$, the convection induced by the substrate motion in the negative x -direction balances the Darcy flow in the positive x -direction. Evaporative mass loss is negligible, because the spatial extent of the wet zone quantified by x_d is very short. In steady state the balance of Darcy flow and substrate motion yields

$$\langle u \rangle \sim \phi S_w U_{sub}.$$

Using Eq. (2.2) and x_d as the relevant lateral lengthscale, this leads to the scaling relation $x_d \sim U_{sub}^{-1}$, in perfect agreement with the numerical results

shown in the inset in Fig. 2.5(a).

In the limit of small $|U_{sub}|$, the extension of the wet zone is not controlled by the substrate motion, but rather by the evaporative mass loss. This explains why x_d approaches a constant for decreasing $|U_{sub}| \rightarrow 0$ in the inset in Fig. 2.5(a). The extension of the wet zone becomes considerably large, which implies that a wide zone is subjected to evaporative cooling and thus a reduced temperature $T < T_{amb}$. The evaporatively cooled substrate temperature saturates for small $|U_{sub}|$, because the sorption term proportional to U_{sub} becomes negligible and the thermal coupling with the base plate becomes dominant. This cold zone induces a thermal-buoyancy-induced flow in the gas phase that is driven by the temperature difference between the nozzle and the substrate. This flow is locally in the positive x -direction consistent with the finding e.g. in Fig. 2.9(a). Consequently, in the limit of small $|U_{sub}|$, the horizontal gas flow speed and the gas temperature distribution in the vicinity of the nozzle goes approximately constant and so does the evaporation rate j . Thus, all terms in Eq. (2.10) are small for steady state and small $|U_{sub}|$ and thus large x_d , except \dot{q} . The wetting term in \dot{q} is negligible and the remaining terms indicate a scaling of ΔT_{max} that is independent of U_{sub} in perfect agreement with the trend observed in Fig. 2.3(a).

For high $|U_{sub}|$, the heat released by wetting becomes significantly higher than the heat released by vapor recondensation. In this regime, the flow speed in the gas phase is determined by U_{sub} rather than buoyancy effects. All horizontal gradient terms scale as $x_d^{-1} \sim U_{sub}$. As the typical values of the Peclet number $Pe = U_{sub}x_d/D_{H_2O} \approx 0.1$ are both small and approximately constant, the typical lengthscales in the x - and y -directions in the gas phase are equal. Therefore, the mass flux j is expected to scale approximately linearly with U_{sub} , which implies that the term jL_w/M_w in Eq. (2.18) is negligible compared to the wetting term proportional to U_{sub}^2 in the recondensation region. The same holds for the heat conduction term and the term proportional to h_N in Eq. (2.18). Consequently, all non-negligible terms in Eq. (2.10) scale as U_{sub}^2 , which means that again ΔT_{max} should become constant. This is visible in Fig. 2.3(a) only approximately, as ΔT_{max} decreases by only about 30% upon an increase in speed from 1 mm/s to 10 mm/s. At speeds higher than 10 mm/s the trend of ΔT_{max} approaching a constant becomes more apparent (data not shown), however, the validity of our 1D model becomes somewhat questionable in this regime.

At $U_{sub} \approx 1$ mm/s, the heat released due to wetting and recondensation are of similar magnitude and the locations of the maximum heat release for both effects essentially coincide, leading to a global maximum of ΔT_{max} .

2.5.4 Limitations of our model

1. We consider a one-dimensional model in the paper domain, i.e. the T and S_w distributions are assumed to be independent of z . This is permissible for thin substrates but places an upper limit U_c on the substrate speed $|U_{sub}|$. A suitable criterion may be that x_d should remain larger than the substrate thickness t_p , which indicates that $U_c > 10$ mm/s according to the inset of Fig. 2.5(a).
2. The air phase is explicitly disregarded in the paper domain, only the liquid-phase saturation is considered. This is permissible as there is no net airflow in the thickness direction of the paper that could enhance evaporation or condensation. Moreover, pushing away of air by the liquid-filled zone does not induce any pressure drop, as the air escapes essentially without resistance in the vertical direction owing to the thinness of the paper. Moreover, the heat capacity of the displaced air is negligible compared to that of water or paper.
3. We neglected the hysteretic behavior of the capillary pressure. This does not restrict the validity of our model, as we only consider (quasi-) steady state wetting of a substrate, i.e. hysteretic behavior cannot manifest itself.
4. We assume laminar flow in the gas phase, which is appropriate for the relatively low Reynolds numbers $\lesssim 50$ resulting from the simulations.
5. We assume the temperature of the nozzle to be ambient, whereas evaporative cooling can reduce it slightly.
6. We do not explicitly account for the exchange of liquid between the pore space and the interior of the paper fibers, neither for the water transport inside the fibers.
7. We neglected evaporation from the underside of the paper. This is permissible as the space underneath is narrow, closed and cannot take up much humidity. Moreover, for the same reason there is no significant gas convection in this region.

2.6 Summary and conclusions

We have studied the temperature increase of paper substrates when they come in contact with liquid water by means of infrared thermography. The heating is due to the release of latent heat upon water vapor condensation on the dry

regions and the release of the heat of wetting. We have conducted systematic experiments using both coated and uncoated paper types. Moreover, we developed a coupled numerical model taking into account vapor convection and diffusion in the gas phase as well as liquid flow in the thin porous medium coupled with heat transfer. The numerical results reproduce the experimental results well.

The results are relevant to inkjet printing, where infrared thermography can be used to monitor the imbibition of water into paper substrates and its subsequent evaporation. The simulations point at a complex buoyancy-induced gas-phase convection pattern, that changes qualitatively as the substrate speed is altered. This suggests that an external flow should be applied to facilitate a robust process control.

Acknowledgements

This work is part of the research programme ‘*The role of surfactants in spreading, imbibition and sorption of water-based printing inks*’ with project number 14666, which is (partly) financed by the Netherlands Organisation for Scientific Research (NWO). The author thanks Nicolae Tomozeiu and Herman Wijshoff of Océ - A Canon Company for fruitful discussions and suggestions. Louis Saes of the same organisation is acknowledged for supplying sorption isotherm data for various types of paper sheets. The author extends his thanks to Gerald Oerlemans of Eindhoven University of Technology for his contribution to the design of the apparatus. Jorgen van der veen of Eindhoven University of Technology is thanked for helping the author to calibrate the IR camera.

Table 2.1: List of symbols and parameters.

Symbol	Name	Value	Units
a_w	Water activity	-	-
c_g	GAB Isotherm constant	18.647	-
$c_{p,air}$	Specific heat capacity of air	1000	J/kgK
$c_{p,av}$	Volume averaged specific heat capacity	-	J/kgK
$c_{p,s}$	Specific heat capacity of solid	1400	J/kgK
$c_{p,w}$	Specific heat capacity of water	4180	J/kgK
C_1	Prefactor of heat of wetting	$1.2 \cdot 10^6$	J/kg
C_2	Exponential prefactor of heat of wetting	25	-
D_{H_2O}	Water vapour diffusivity in air	$0.28 \cdot 10^{-4}$	m^2/s
h_n	Convective heat transfer coefficient	5	W/m^2K
ΔH_s	Heat of wetting	-	J/kg
j	Mass flux of water vapor	-	kg/m^3s
k	GAB Isotherm constant	0.85	-
k_{air}	Thermal conductivity of air	0.025	W/mK
k_{av}	Volume averaged thermal conductivity	-	W/mK
k_c	Relative permeability parameter	-0.4	-
K_{rw}	Relative permeability	-	-
k_s	Thermal conductivity of solid	0.4	W/mK
K_s	Absolute permeability	$1.2 \cdot 10^{-12}$	m^2
k_w	Thermal conductivity of water	0.6	W/mK
L_w	Latent heat of water	$2.44 \cdot 10^6$	J/kg
M_0	GAB isotherm parameter	0.061	-
m_g	Van Genuchten exponent	$1-1/n_g$	-
M_w	Molar mass of water	$18 \cdot 10^{-3}$	kg/mol
n_g	Capillary pressure exponent	14	-
p	Pressure of the gas	-	Pa
p_{amb}	Ambient pressure	$1 \cdot 10^5$	Pa
p_c	Capillary pressure	-	Pa
p_g	Pressure scaling parameter	-2800	Pa
p_{sat}	Saturation vapor pressure	-	Pa
\dot{q}	Heat source	-	W/m^3
r_h	Relative humidity	-	-
R_{dryair}	Specific gas constant of dry air	287	J/kgK
R_{H_2O}	Specific gas constant of water vapor	461.5	J/kgK
S_{ra}	Residual air saturation	0.1	-
S_{rw}	Residual water saturation	-	-
S_w	Degree of saturation	-	-
T	Temperature of the porous medium	-	K
T_{amb}	Ambient temperature	298.15	K
T_{gas}	Temperature of the gas	-	K
t_p	Paper thickness	0.1	mm
$\langle \bar{\mathbf{u}} \rangle$	Darcy velocity	-	m/s
$\bar{\mathbf{u}}$	Velocity of the gas phase	-	m/s
U_{sub}	Speed of the substrate	-	m/s
x	Horizontal coordinate	-	m
x_d	Horizontal extension of wetting front	-	m
y	Vertical coordinate	-	m
μ_{air}	Dynamic viscosity of air	$1.81 \cdot 10^{-5}$	Pa-s
μ_w	Dynamic viscosity of water	$8.9 \cdot 10^{-4}$	Pa-s
ρ_{av}	Volume averaged density	-	kg/m^3
ρ_{gas}	Mass density of air-vapor mixture	-	-
ρ_{H_2O}	Concentration of water vapor	-	kg/m^3
ρ_s	Mass density of solid	1500	kg/m^3
ρ_{sat}	Saturation conc. of water vapor in air	0.02287	kg/m^3
ρ_w	Mass density of water	1000	kg/m^3
ϕ	Porosity	-	-

Chapter 3

Inkjet deposition of lines onto thin moving porous media

The deposition of lines of water onto a thin porous medium by means of a droplet-on-demand, single-nozzle inkjet system is studied. The substrate speed and the droplet frequency are systematically varied. Optical transmission imaging was used to measure the dynamic moisture distribution in the substrate in conjunction with infrared thermography to determine the in-plane temperature distribution of the paper. The temperature of the paper becomes non-uniform mainly due to evaporative cooling. Furthermore, a numerical model coupling Richards' equation for moisture transport in unsaturated porous media with evaporative mass-loss and heat transfer. The results of the numerical simulation agree qualitatively well with the experiments.

3.1 Introduction

Inkjet printing consists of the ejection and deposition of ink droplets on substrates that are moving underneath the printhead [7, 101–103]. The contactless nature of the process provides great flexibility regarding the compositions of both the ink and the substrate. For printing on paper, water-based inks have been developed that are beneficial from an environmental standpoint.

The printing of a long or semi-infinite line on a moving paper substrate gives rise to steady-state distributions of moisture and temperature, which are a convenient way to study the interplay of heat and mass transfer in inkjet printing. Fabie *et al.*, Ubal *et al.* and Friedrich and Begley have studied the continuous deposition of a liquid thread onto a partially-wetting, impermeable substrate [104–106]. Karyappa *et al.* showed that the line deposition on impermeable substrates can benefit from immersion in a pool of an immiscible liquid [107]. The deposition of extruded threads of ceramic slurries [108, 109] or molten polymers [110, 111] onto impermeable substrates has been studied in the context of additive manufacturing. Li *et al.* reviewed technological applications

of pen-based writing as a method of rapid prototyping [112]. Kim *et al.* studied the deposition of continuous lines of ink on impermeable but topographically patterned surfaces that exhibit surface wicking [113, 114]. Duineveld, Thompson *et al.* and Zhou *et al.* studied the intermittent deposition of lines using an ink-jet on impermeable surfaces, which can give rise to a bulge instability on surfaces with zero receding contact angle [115–117]. Franke and Rose studied pen writing on paper [118].

In this chapter we study the heat and mass transfer aspects governing inkjet printing on paper. The main contributions to mass transfer arise from lateral wicking inside the paper and solvent evaporation. Regarding heat transfer, evaporative cooling reduces the paper temperature by up to approximately 6 K, which has a measurable impact on the evaporation rate. Moreover, the heat of wetting [119] and the temperature of the incoming droplets need to be taken into account. We disregard the impact process of the deposited droplets, which occurs on a millisecond timescale. In the experiments to follow emphasis is on the regime in which the substrate speeds are sufficiently slow, such that transport in the thickness direction of paper can be considered instantaneous. This allows us to focus on the lateral imbibition dynamics on a timescale of seconds or longer.

Our goals were to develop an experimental setup and procedure to systematically and quantitatively measure the moisture distribution and temperature field of moving sheets of paper and to develop a theoretical model with which the heat and mass transfer dynamics can be rationalized and reproduced. We use light transmission [120] to characterize the moisture content and infrared thermography [119] to determine the temperature of the paper. The speed of motion of the substrate and the frequency of droplet deposition will be systematically varied. Moreover, a theoretical model is developed that couples Richards' equation [121], evaporative mass transfer and heat transfer that reproduces many features of the experiments very well. It is to be noted that the difference between the experiments to follow and the experiments detailed in chapter 2 is not merely the introduction of the ink-jet deposition, but also the changes to the geometry of the deposited wet-zone which permits visualization and quantification of its entirety. In contrast, chapter 2 focused entirely on the heat and mass transfer processes occurring at the front of the wet-zone.

Section 3.2 contains a description of the experimental setup and procedures. Section 3.3 details the experimental results and section 3.4 the theoretical model. Section 3.5 presents the numerical results including a comparison with the experimental results.

3.2 Materials and methods

3.2.1 Experimental set-up, inkjet operation and dual-visualization

Figure 3.1(a) shows a schematic of the experimental set-up for printing lines of water onto a horizontal paper substrate. It consists of a sheet of uncoated, uncalendered paper (Mondi, DNS HSI NF) mounted 12 mm above an area light source (Advanced Illumination, wavelength 660 nm) that is placed on a motorized translation stage (Newport, model UTS 100CC). The constant substrate speed U_{IJ} is directed in the positive x -direction and varied between 0.05 and 5 mm/s. The length, width and thickness of the substrate were approximately 60, 45 and 0.1 mm, respectively. Figure 3.1(b) shows a top-view photograph of a line being printed on a paper substrate.

A stationary printhead (Microdrop, model MDK-140-020) is mounted approximately 5 mm above the surface of the paper at an angle of approximately 45° with respect to the vertical z -direction. The printhead is operated with a typical applied voltage of 65 V, a pulse width of 80 μs and a constant droplet ejection frequency f ranging between 10 and 1000 Hz. The emitted droplets have a diameter $D \approx 40 \mu\text{m}$. Figure 3.2 shows emitted drops in flight for a few instances of the strobe delay time, after attainment of the stable operating mode (see, fig. 1.2(g)). The time-averaged mass flow rate \dot{m} was measured by jetting liquid into a tall bottle with a narrow mouth to minimize evaporative mass loss and subsequent weighing, resulting in 26 $\mu\text{g/s}$ for $f = 1000 \text{ Hz}$. We used ultrapure water for our experiments (Millipore, model Direct-Q3 R). The fate of hundreds of thousands of such drops shown in fig 3.2 after a time x_d/U_{IJ} , with x_d the horizontal printing distance, become, as shown in fig 3.1(b). For more details on the physics governing drop emission or piezo-electric actuation, the reader is referred to [7].

A long-wave infrared (IR) camera (FLIR, model A35sc, 320×256 pixels, spectral sensitivity range 7.5 – 13.5 μm) is used to determine the temperature field $T(x, y, t)$ of the substrate upon deposition of liquid. Due to its fibrous nature, printing paper is non-transparent to long-wave IR radiation [119]. The area light source underneath the paper does not significantly heat up during operation and hence does not alter the temperature distribution. The moisture distribution is determined from the intensity $I(x, y, t)$ of optical transmission through the paper by means of a CCD camera.

Figure 3.1(c) shows a typical optical transmission image for $U_{IJ} = 0.1 \text{ mm/s}$ and $f = 1000 \text{ Hz}$, at a time $t = 300 \text{ s}$ after commencing both the substrate motion and the ink-jet deposition. The optical transmission intensity of the wet zone is not uniform in space. The moisture content is highest close to the

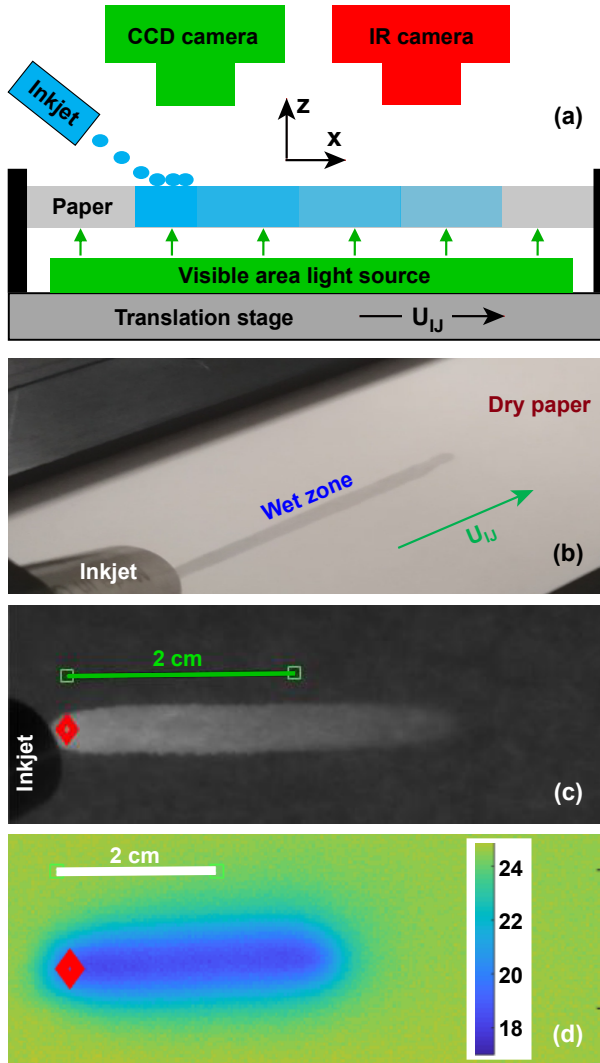


Figure 3.1: (a) Sketch of the experimental setup. A stationary printhead periodically deposits drops of ultrapure water onto a moving paper substrate. The moisture content is evaluated by means of the transmitted light intensity. The substrate temperature is monitored by an IR camera. (b) Top-view photograph of a line being printed on a paper substrate. (c) Optical transmission image for $U_{IJ} = 0.1$ mm/s and $f = 1000$ Hz at a time $t = 300$ s after commencement of deposition. (d) Corresponding temperature map. The color bar on the right illustrates the temperature of the paper in centigrade.

impingement point of the inkjet droplets. A higher moisture content leads to a reduction in scattering of light, because the refractive index of water is closer to

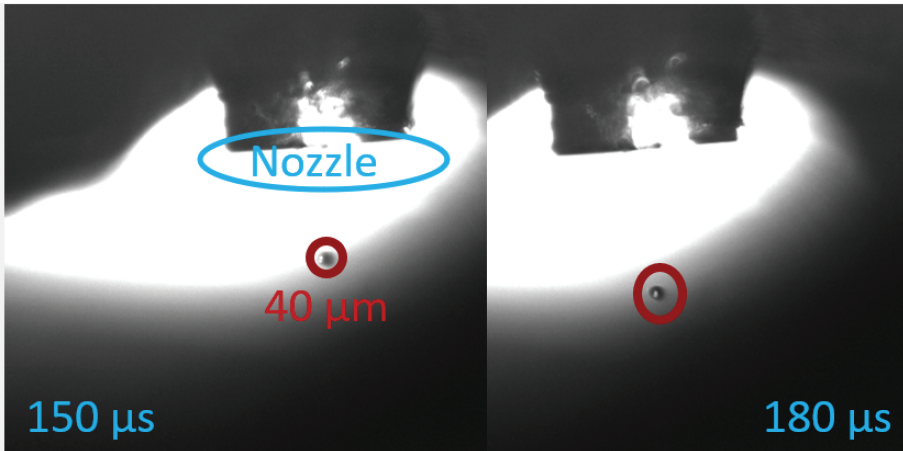


Figure 3.2: Photograph of droplets being emitted for two instances of the strobe delay time. The blue-elliptical box marks the ink-jet nozzle.

the one of cellulose than that of air, corresponding to a higher light transmission than for dry paper [122]. Figure 3.1(d) shows the temperature distribution for the same experiment as shown in Figure 3.1(c). In both Figs. 3.1(c) and (d), the red diamond marks the impingement point, which defines $x = 0$.

3.2.2 Calibration of intensity vs. moisture content

To correlate the transmitted intensity with the moisture content in the paper substrate, we performed calibration experiments. We submerged a piece of paper with dimensions 50×55 mm into a water bath. After retraction, the porous paper was completely saturated with water and excess liquid adhered to both surfaces. Subsequently, we removed the excess liquid using a combination of evaporative mass loss and repeated contact with a dry metallic surface. Using a combination of optical microscopy and observation of specular light reflection from the wet surface, we determined the maximum moisture content, when water only resides inside the paper and no excess liquid remains on its surface.

Figure 3.3 show reflection microscopy images of different stages of this process. Figure 3.3(a) shows a rather uniform intensity, corresponding to a thick layer of entrained excess liquid directly after removal from the bath. Figure 3.3(b) was recorded some time later, after some of the excess liquid had been removed. Water puddles are still clearly visible. Figure 3.3(c) corresponds to the maximum moisture content inside the paper, after the excess liquid is gone. Subsequently, the wet paper is placed between two plastic sheets of known weight to prevent further evaporation. The mass of the contained water is obtained by weigh-

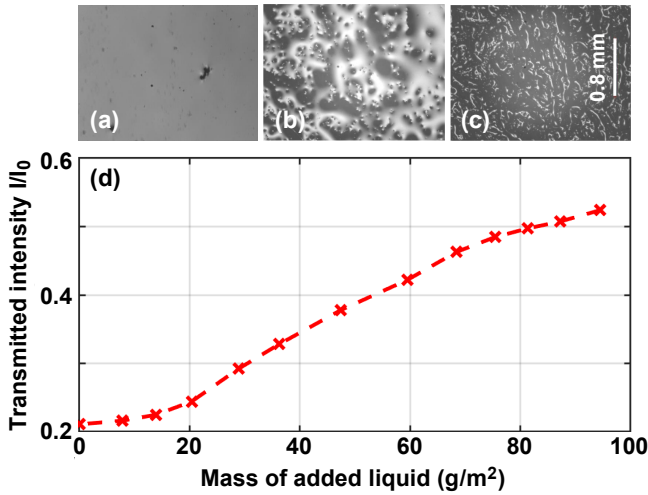


Figure 3.3: (a-c) Reflection microscopy images of a paper sheet with different amounts of excess liquid. (a) A thick uniform liquid layer resides on the top giving rise to a uniform reflected intensity. (b) Some time later, a discontinuous liquid film is visible on top of the paper. In (c) all the excess liquid is gone and water resides only inside the paper bulk. (d) Dependence of transmitted intensity on the mass of added liquid.

ing. The wet paper with a known mass of added liquid is then placed in the setup to obtain the transmitted intensity I . To obtain additional calibration points between the fully wet and the fully dry configurations, the liquid in the paper is allowed to evaporate by temporarily removing the plastic sheets and repeating the procedure. Figure 3.3 (d) shows the dependence of I/I_0 on the residual mass of liquid per unit area of the paper. Here, I_0 corresponds to the maximum grayscale intensity, i.e. the intensity obtained when there is no paper placed between the camera and the light source. The integration time of the CCD camera was adjusted to provide a grayscale level of $I_0 = 245$ to prevent oversaturation.

3.2.3 The maximum liquid holding capacity of paper

The maximum holding capacity was determined in the previous subsection to be $\Theta_{w,max} = 94 \text{ g/m}^2$ for water. The mass of paper equilibrated with the ambient humidity level $RH \approx 30\%$ is $\Theta_s = 77 \text{ g/m}^2$, which we consider an approximation for dry paper. The maximum possible value of the moisture content $\theta_w \equiv \Theta_w/\Theta_s$ (kg water/kg dry paper) is thus 1.21. Table 3.1 lists the measured values of $\theta_{l,max}$ for three different liquids. Polar liquids such as water and ethylene glycol (EG) give rise to a significantly higher value of $\theta_{w,max}$ than

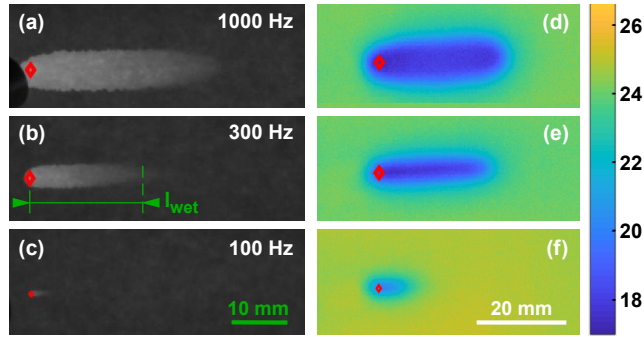


Figure 3.4: (a-c) Optical transmission images for $U_{IJ} = 0.05$ mm/s, $t = 600$ s and (a) $f = 1000$ Hz, (b) 300 Hz and (c) 100 Hz. (d-f) Corresponding temperature distributions. The red diamond in each image indicates the impingement point $(x, y) = (0, 0)$.

non-polar liquids like hexadecane. This difference is attributed to the swelling of cellulose fibers induced by polar liquids [123–125].

Table 3.1: Maximum holding capacity of Mondi DNS HSI NF printing paper for different liquids.

Liquid	$\theta_{l,max}$	γ (mN/m)
Water	1.21	72
Ethylene glycol (EG)	1.11	47
Hexadecane	0.46	27

3.3 Experimental results

In the experiments, we systematically varied the frequency of droplet deposition f and the substrate speed U_{IJ} .

3.3.1 Variation of the deposition frequency

Figure 3.4(a-c) show optical transmission images for $U_{IJ} = 0.05$ mm/s and three different values of f . Figures 3.4(d-f) show the corresponding IR images. The red diamonds denote the location of the impingement point $(x, y) = (0, 0)$. All images were recorded at $t = 600$ s after commencement of injection. Figure 3.5(a,b) shows longitudinal cross-sections of both the moisture content $\theta_w(x, y = 0, t = 600$ s) and the temperature distribution $\Delta T \equiv T(x, y = 0, t = 600$ s) $- T_{amb}$. The fluctuations in Fig. 3.5(a) are not measurement noise, but

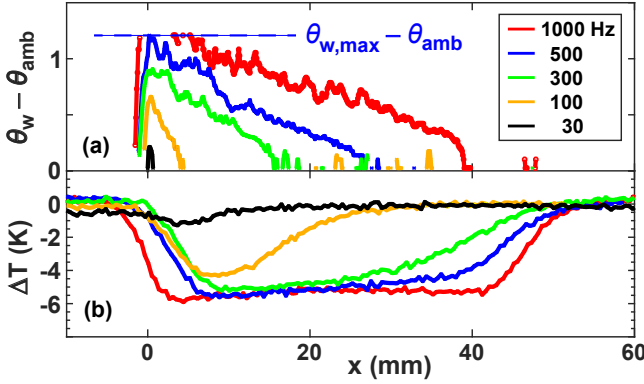


Figure 3.5: (a) Moisture content distribution $\theta_w(x, y = 0, t = 600 \text{ s})$ for $U_{IJ} = 0.05 \text{ mm/s}$ and different values of f . (b) Corresponding temperature distributions $\Delta T \equiv T(x, y = 0, t = 600 \text{ s}) - T_{amb}$. All data shown correspond to a time $t = 600 \text{ s}$.

rather reflect heterogeneities of the material properties and the conformation of the paper sheet.

The length and width of the wet zone increase with frequency. For the two highest frequencies $f = 500$ and 1000 Hz , the moisture content θ_w is equal to $\theta_{w,max}$ close to the impingement point $x = 0$. For lower frequencies, $\theta_w(x = 0)$ drops below $\theta_{w,max}$ and decreases. As f increases, the longitudinal gradients $\frac{\partial \theta_w}{\partial x}$ decrease in the wet zone. This is because at higher f more liquid is added per unit length and evaporation has a relatively weaker effect on θ_w at a fixed position and time.

We define the length of the wet zone l_{wet} as the x -position where $\theta_w(x, y = 0) - \theta_{amb}$ has decreased to a value of 0.1 again, measured relative to the impingement point $x = 0$ along the positive x -direction. The blue asterisks in Fig. 3.6(b) represent the experimental values of l_{wet} , which are plotted as a function of f . For values of $U_{IJ} = 0.05 \text{ mm/s}$ and $t = 600 \text{ s}$, the length of the printed line is $U_{IJ}t = 30 \text{ mm}$. For low values of f , l_{wet} is shorter than $U_{IJ}t$, whereas for $f = 1000 \text{ Hz}$, $l_{wet} > U_{IJ}t$. The value of l_{wet} can exceed $U_{IJ}t$ due to Darcy flow in the x -direction, especially at low U_{IJ} . It can also be shorter than $U_{IJ}t$ due to evaporation (especially at low frequencies f) and Darcy flow in the y -direction (especially at high speeds U_{IJ} , see Section 3.3.2).

Figure 3.5(b) shows that the entire wet zone is colder than T_{amb} due to evaporative cooling. For high values of $f \geq 500 \text{ Hz}$, the temperature is rather uniform in the region $0 \leq x \leq U_{IJ}t$. As shown in Fig. 3.6(c), the amplitude of cooling increases with increasing frequency, as more liquid gets added and is subsequently distributed over a wider and longer zone. The length of the

cold zone exceeds l_{wet} , because it takes a finite time for the paper to reach T_{amb} again, once it has dried, due to heat exchange with the ambient. For low values of $f = 30$ and 100 Hz, T returns to T_{amb} at a distance well before $U_{IJ}t$. Moreover, for low frequencies $f = 30$ and 100 Hz, the minimum of the temperature distribution occurs at $x \approx l_{wet}$. In contrast, for high frequencies the coldest point is located close to the impingement point $x = 0$. The blue asterisk in Fig. 3.6(c) represent the experimental data of the maximum temperature difference $\Delta T_{max}(t) \equiv \max |T(x, y, t) - T_{amb}|$, which is plotted as a function of f for $t = 600$ s.

3.3.2 Variation of the substrate speed

Figure 3.7(a-e) shows optical transmission images and the corresponding temperature distributions for a constant frequency $f = 1000$ Hz and different values of U_{IJ} spanning two decades from 0.05 to 5 mm/s. The labels in Fig. 3.7(a) and (f) illustrate the definitions of the transverse widths [full width at half maximum/minimum (FWHM)] of the moisture distribution Δy_w and of the

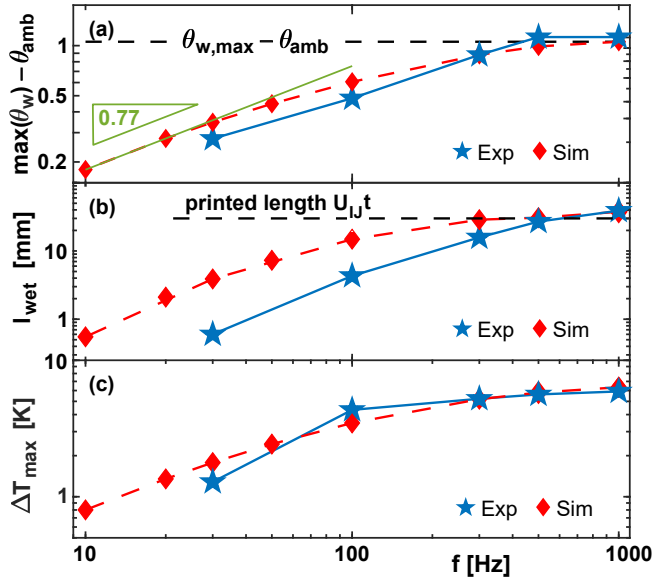


Figure 3.6: (a) Maximum moisture content $\max(\theta_w)$ as a function of droplet frequency for $U_{IJ} = 0.05$ mm/s and a printed length of $U_{IJ}t = 30$ mm. (b) Length of the wet zone l_{wet} as a function of f for $U_{IJ} = 0.05$ mm/s and a printed length of $U_{IJ}t = 30$ mm. (c) Maximum temperature difference ΔT_{max} as a function of f for $U_{IJ} = 0.05$ mm/s and a printed length of $U_{IJ}t = 30$ mm. In (a-c) the blue asterisks represent experimental data, the red diamonds numerical simulations.

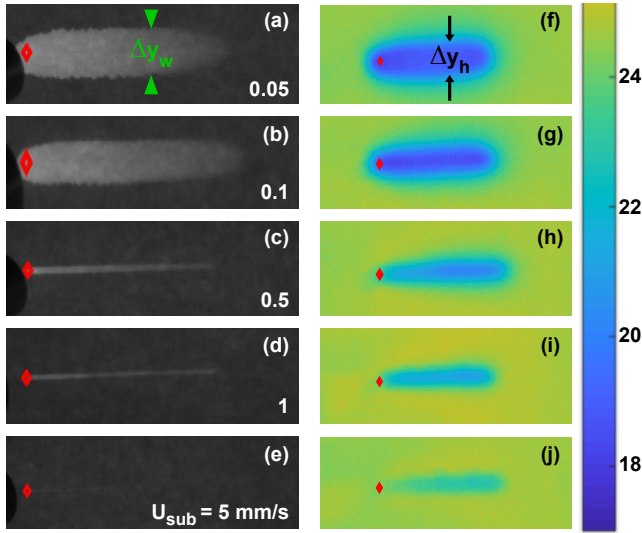


Figure 3.7: Optical transmission maps (a-e) and temperature distributions (f-j) for $f = 1000 \text{ Hz}$ and different values of the substrate speed (a,f) $U_{IJ} = 0.05 \text{ mm/s}$, (b,g) 0.1 mm/s , (c,h) 0.5 mm/s , (d,i) 1 mm/s and (e,j) 5 mm/s . The maps were recorded at different times corresponding to a constant value of $U_{IJ}t = 3 \text{ cm}$. The red diamonds denote the impingement point $x = 0$.

temperature distribution Δy_h . Figure 3.8(a) shows longitudinal cross-sections $\theta_w(x, y = 0)$ of the 2D-maps shown in Fig. 3.7(a-e). The data were extracted for printed line lengths $U_{IJ}t = 3 \text{ cm}$, i.e. the variation of U_{IJ} implies different printing times. For low values of $U_{IJ} < 0.5 \text{ mm/s}$, the moisture content θ_w reaches $\theta_{w,max}$ close to the impingement point $x = 0$, similarly to the high frequency data shown in Fig. 3.5(a). The width of this fully saturated zone decreases with increasing U_{IJ} . For $U_{IJ} > 0.5 \text{ mm/s}$, $\theta_w(0, 0)$ is no longer saturated and decreases with increasing U_{IJ} .

The temperature distributions $\Delta T(x, y = 0)$ for low speeds $U_{IJ} \leq 0.2 \text{ mm/s}$ in Fig. 3.8(b) are also qualitatively similar to the high frequency data in Fig. 3.5(b) in the sense that the temperature is rather uniform in the region $0 \leq x \leq U_{IJ}t$. For high speeds $U_{IJ} \geq 0.5 \text{ mm/s}$, the coldest point is close to the end of the wet zone $x \approx l_{wet}$.

Figures 3.9(a,b) present Δy_w and Δy_h as functions of U_{IJ} at position $x = 20 \text{ mm}$ for a printing distance of $U_{IJ}t = 30 \text{ mm}$. The solid lines represent power-law fits with $\Delta y_w \sim U_{IJ}^{-0.7}$, and $\Delta y_h \sim U_{IJ}^{-0.3}$, which are excellent approximations to the measured data (blue asterisks). Figure 3.9(c) shows measurements of the maximum cooling amplitude $\Delta T_{max} \equiv \max |T - T_{amb}|$, which are well

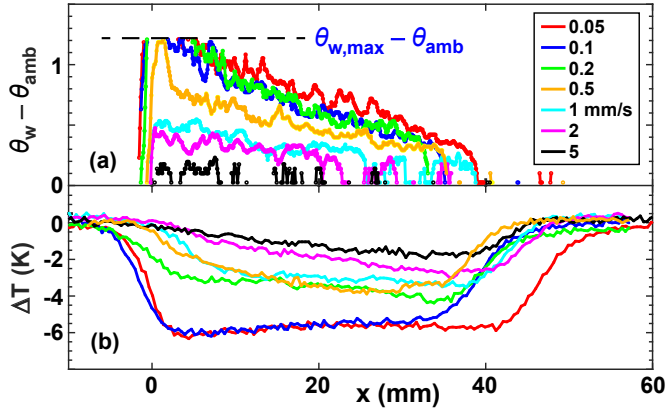


Figure 3.8: Longitudinal cross-sections of (a) the moisture content $\theta_w(x, y = 0)$ and (b) the corresponding temperature distributions $\Delta T(x, y = 0)$ for different values of U_{IJ} . All data shown correspond to a printed length of $U_{IJ}t = 3$ cm.

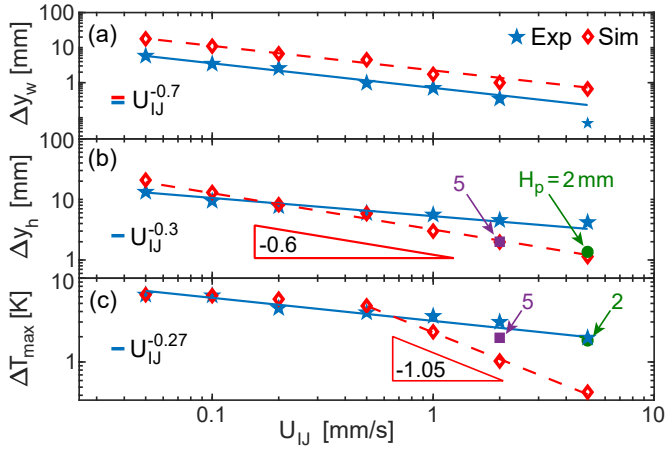


Figure 3.9: (a,b) Transverse widths (FWHM) of (a) the moisture distribution Δy_w and (b) the temperature distribution Δy_h as a function of U_{IJ} . The data were extracted from two-dimensional maps at a position $x = 2$ cm when the printed line length was $U_{IJ}t = 3$ cm. (c) Maximum cooling amplitude ΔT_{max} as a function of U_{IJ} extracted from Fig. 3.8(b). Blue stars represent experimental data. Red diamonds are simulations with a fixed convection length $H_p = 10$ mm. Violet and green squares and circles correspond to $H_p = 5$ mm and $H_p = 2$ mm, respectively. The solid and dashed lines in (a-c) represent powerlaw fits. The blue asterisks correspond to experimental data, the other symbols to numerical results.

represented by the powerlaw $\Delta T_{max} \sim U_{IJ}^{-0.27}$.

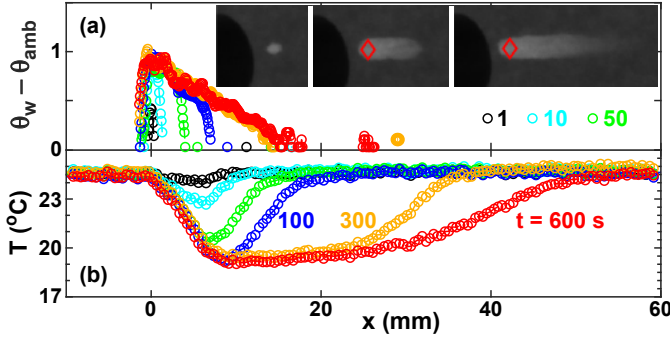


Figure 3.10: (a) Longitudinal cross-sections of (a) the moisture content $\theta_w(x, y = 0)$ and (b) the corresponding temperature distribution $T(x, y = 0)$ for $U_{IJ} = 0.05$ mm/s, $f = 300$ Hz and different times. The insets in (a) are optical transmission maps for $t = 10, 100, \text{ and } 300$ s. The red diamonds represent the impingement point $x = 0$.

3.3.3 Transient evolution of a deposited line

Figures 3.10(a,b) show longitudinal cross-sections of the moisture content $\theta_w(x, y = 0)$ and the corresponding temperature distribution $T(x, y = 0)$ for $U_{IJ} = 0.05$ mm/s, $f = 300$ Hz and different times after the commencement of deposition. The inset in (a) shows the corresponding optical transmission maps obtained at $t = 10, 100$ and 300 s. With increasing times, $\theta_w(x = 0, y = 0)$ increases until it reaches a value of about 1 and remains steady for $t \geq 100$ s. The length of the wet zone l_{wet} increases until $t \approx 300$ s and remains constant thereafter. For the early times, l_{wet} is slightly larger than $U_{IJ}t$, indicating the effect of wicking. For later times ($t \geq 300$ s), the liquid distribution profile becomes linear. According to Fig. 3.10 the moisture content becomes steady at $t \approx 300$ s, whereas the temperature distribution becomes steady only after 600 s. The maximum temperature difference ΔT_{max} initially increases with time before saturating at $t \approx 100$ s.

Figures 3.11(a,b) present the time evolution of the length of the wet zone $l_{wet}(t)$ and of the maximum temperature amplitude $\Delta T_{max}(t)$ for two different printing frequencies $f = 300$ and 500 Hz. For $t \leq 100$ s, l_{wet} increases monotonically and - in the case of $f = 300$ Hz - saturates for $t \geq 300$ s. The triangle represents a powerlaw relation $l_{wet} \sim t^\alpha$ with exponent $\alpha = 1$, i.e. if a powerlaw were fitted to the experimental data, the exponent α would be smaller than 1. For $t \leq 100$ s, ΔT_{max} increases approximately according to $t^{0.5}$ and saturates for $t \geq 100$ s, i.e. ΔT_{max} saturates sooner than l_{wet} .

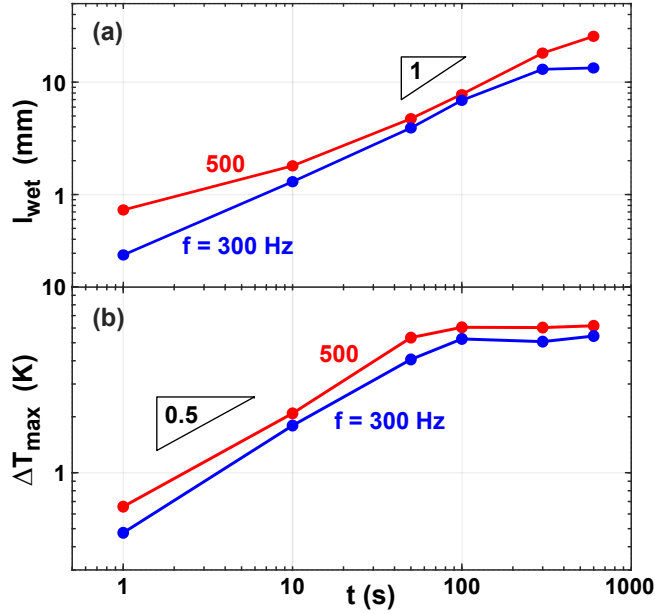


Figure 3.11: Time dependence of (a) the length of the wet zone $l_{\text{wet}}(t)$ and (b) the maximum temperature amplitude $\Delta T_{\text{max}}(t)$ for $U_{1J} = 0.05$ mm/s and two different values of f .

3.4 Theoretical model

3.4.1 Moisture transport

Our starting point is the continuity equation for moisture transport in a porous medium [126]

$$\frac{\partial \Theta_{w,3D}}{\partial t} + \nabla \cdot (\rho_w \vec{\mathbf{v}}_w) = 0, \quad (3.1)$$

where $\Theta_{w,3D}$ is the mass of water contained in a unit volume of porous medium, $\rho_w = 1000$ kg/m³ the mass density of liquid water, and $\vec{\mathbf{v}}_w$ the volumetric water flux given by the Darcy equation

$$\vec{\mathbf{v}}_w = -\frac{k_w}{\mu_w} \nabla p_w. \quad (3.2)$$

Here, k_w is the permeability, $\mu_w = 1$ mPas the viscosity of liquid water, and p_w the pressure in the liquid phase. Because the paper is oriented horizontally in our experiments and has a very small thickness t_p , there is no gravity term in Eq. (3.2). We assume that evaporation occurs at the surface only, i.e. there is no gas flow through the paper, such that there is no sink term in Eq. (3.1).

Due to the small thickness of paper, we assume that the moisture content is uniform in the z -direction. This neglects the short transient effects corresponding to vertical imbibition upon deposition of a droplet (typical timescale ≤ 1 s), which is appropriate for the description of lateral imbibition processes governed by longer timescales. Our next step is to integrate Eq. (3.1) in the thickness direction

$$\int_{-t_p/2}^{t_p/2} \left[\frac{\partial \Theta_{w,3D}}{\partial t} + \nabla \cdot (\rho_w \vec{v}_w) \right] dz = 0 , \quad (3.3)$$

which yields

$$\frac{\partial \Theta_w}{\partial t} - j + \rho_w \int_{-t_p/2}^{t_p/2} \left(\frac{\partial v_{w,x}}{\partial x} + \frac{\partial v_{w,y}}{\partial y} \right) dz = 0 . \quad (3.4)$$

Here, we introduced the mass of water per unit *area* of paper

$$\Theta_w \equiv \int_{-t_p/2}^{t_p/2} \Theta_{w,3D} dz \quad (3.5)$$

and the influx or loss of water due to droplet deposition and evaporation

$$\begin{aligned} j &\equiv \rho_w v_{w,z}(z = -t_p/2) - \rho_w v_{w,z}(z = t_p/2) \\ &= j_{IJ} - k_\infty (\rho_s - \rho_\infty) , \end{aligned} \quad (3.6)$$

where k_∞ is a mass transfer coefficient, ρ_∞ is the ambient water vapor concentration and ρ_s is the water vapor concentration at the paper top surface. The term j_{IJ} denotes the mass influx due to the inkjet-deposited droplets, which is described in Section 3.4.4.

Evaluating the integral in Eq. (3.4) we get

$$\frac{\partial \Theta_w}{\partial t} - \frac{\rho_w}{\mu_w} \nabla_{2D} \cdot [t_p k_w \nabla_{2D} p_w] = j , \quad (3.7)$$

where $\nabla_{2D} \equiv (\frac{\partial}{\partial x}, \frac{\partial}{\partial y})$ is the in-plane gradient operator.

As the paper is translating relative to the inkjet printhead, we transform the above equation into a moving reference frame defined by the new coordinates $(x', y', t') = (x + U_{IJ}t, y, t)$. After dropping the primes, this effectively yields an

extra term $U_{IJ} \frac{\partial \Theta_w}{\partial x}$ on the left side of Eq. (3.7). In the new coordinate system, the inkjet impingement location is stationary and j_{IJ} is a function of position only, but independent of time for $t > 0$.

For the permeability $k_w(\Theta_w)$ and the capillary pressure $p_w(\Theta_w)$ we adopt the van Genuchten relations [75] [127]

$$k_w = k_s \left[\frac{\Theta_w}{\Theta_{w,\max}} \right]^{k_c} \left[1 - \left[1 - \left[\frac{\Theta_w}{\Theta_{w,\max}} \right]^{1/m_g} \right]^{m_g} \right]^2 \quad (3.8)$$

$$p_w = p_g \left(\left(\frac{\Theta_w}{\Theta_{w,\max}} \right)^{-1/m_g} - 1 \right)^{(1/n_g)}, \quad (3.9)$$

where $m_g = 1 - 1/n_g$. Here, $k_s = 1 \cdot 10^{-13} \text{m}^2$, $k_c = 0.3$, $n_g = 4$ and $p_g = 2000 \text{Pa}$ and were treated as fit parameters. We neglect effects due to hygroexpansion.

3.4.2 Heat transfer

The equation for heat transfer inside a porous medium is [128]

$$(\rho c_p)_{av} \frac{\partial T}{\partial t} + \rho_w c_{p,w} \vec{\mathbf{v}}_w \cdot \nabla T = \nabla \cdot (k_{av} \nabla T) + \phi_s. \quad (3.10)$$

The thermal material properties are assumed to be given by the following weighted averages

$$k_{av} = \frac{\Theta_w k_w + \Theta_s k_s}{\Theta_w + \Theta_s} \quad (3.11)$$

$$(\rho c_p)_{av} = \frac{\Theta_w (\rho c_p)_w + \Theta_s (\rho c_p)_s}{\Theta_w + \Theta_s}, \quad (3.12)$$

where k_w and k_s are the thermal conductivities and $c_{p,w}$ and $c_{p,s}$ are the specific heat capacities of liquid water and cellulose, respectively. In Eqs. (3.11,3.12) we have neglected the contributions of air for an unsaturated medium, because the thermal conductivity and mass density of air are negligible compared to those of water and cellulose.

The source term in Eq. (3.10) $\phi_s = \Delta H_s \frac{\partial \Theta_{w,3D}}{\partial t}$ accounts for sorptive heating. [119] Here, ΔH_s is the differential heat of wetting, [129–135] which we represent by the empirical equation

$$\Delta H_s = C_1 \exp(-C_2 \theta_w) \quad (3.13)$$

with fit parameters $C_1 = 1500 \text{kJ/kg}$ and $C_2 = 40$.

Assuming all quantities are vertically uniform, we get

$$\begin{aligned} (\rho c_p)_{av} \frac{\partial T}{\partial t} - c_{p,w} \frac{j_{IJ}}{t_p} (T_{IJ} - T) + \rho_w c_{p,w} \vec{v}_{2D} \cdot \nabla_{2D} T = \\ = \frac{q_{2D}}{t_p} + \Phi_s + \nabla_{2D} \cdot (k_{av} \nabla_{2D} T) . \end{aligned} \quad (3.14)$$

The second term on the left of Eq. (3.14) accounts for the thermal mass of the inkjet deposited droplets. The transformation to the moving reference frame effectively adds an extra term $(\rho c_p)_{av} U_{IJ} \frac{\partial T}{\partial x}$ on the left hand side of Eq. (3.14). Similarly, the sorption term becomes

$$\Phi_s = \frac{1}{t_p} \left(\frac{\partial \Theta_w}{\partial t} + U_{IJ} \frac{\partial \Theta_w}{\partial x} \right) \Delta H_s . \quad (3.15)$$

The heat flux

$$q_{2D} \equiv -h_N (T - T_\infty) - k_\infty (\rho_s - \rho_\infty) E_{ev} \quad (3.16)$$

accounts for Newtonian heat exchange with the ambient with corresponding heat transfer coefficient $h_N = 9 \text{ W}/(\text{m}^2 \text{ K})$, mass transfer with the ambient with the corresponding mass transfer coefficient $k_\infty = 2.8 \cdot 10^{-3} \text{ m/s}$ and evaporative cooling, where $E_{ev} = 2441.7 \text{ kJ/kg}$ is the enthalpy of evaporation of water.

The parameter $\rho_s(\Theta_w)$ is determined by the moisture sorption isotherm of the paper substrate, which we assume to be given by a Guggenheim-Anderson-de Boer (GAB) isotherm, which can reproduce the behavior of cellulosic materials very well [134, 136–139]

$$\theta_w = \frac{M_0 C_g k a_w}{(1 - k a_w)(1 + (C_g - 1) k a_w)} . \quad (3.17)$$

Here, a_w the water activity and $M_0 = 0.061$, $C_g = 18.647$ and $k = 0.85$ are typical fit-parameters for paper. [134, 136–139] In local thermodynamic equilibrium, the water activity is equal to the local relative humidity

$$a_w = \rho_s / \rho_{sat}(T) , \quad (3.18)$$

where the saturated water vapor density ρ_{sat} is determined by the following empirical relation for the saturated vapor pressure [140]

$$p_{sat}(\text{Pa}) = 610.78 \exp \left(17.2694 \frac{T(^{\circ}\text{C})}{T(^{\circ}\text{C}) + 238.3} \right) \quad (3.19)$$

and the ideal gas law $\rho_{sat} = p_{sat} M_w / (RT)$. Here, $M_w = 18 \text{ g/mol}$ is the molecular weight of water and $R = 8.314 \text{ J}/(\text{mol K})$ is the universal gas constant.

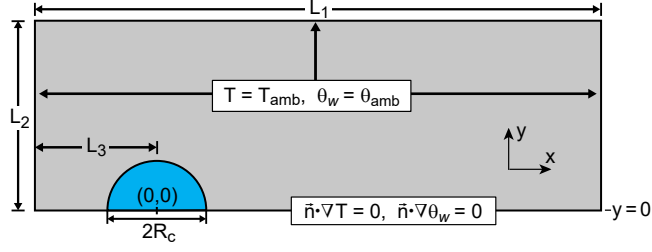


Figure 3.12: Sketch of the two-dimensional computational domain and the applicable boundary conditions.

3.4.3 Boundary conditions

The two-dimensional computational domain and the applicable boundary conditions are sketched in Fig. 3.12. The blue circle of radius R_c centered around the impingement point $(x, y) = (0, 0)$ is the moisture source region. The dimensions L_1 , L_2 and L_3 are chosen sufficiently large such that neither the moisture front nor the temperature changes can reach the lateral or the top boundaries. Correspondingly, Dirichlet boundary conditions corresponding to a sheet of paper maintained at ambient conditions apply

$$T(x = -L_3) = T_{amb} = T(y = L_2) = T(x = L_1 - L_3), \quad (3.20)$$

$$\theta_w(x = -L_3) = \theta_{amb} = \theta_w(y = L_2) = \theta_w(x = L_1 - L_3). \quad (3.21)$$

The bottom boundary $y = 0$ is the centerline of the printed line, where symmetry conditions hold

$$\vec{\mathbf{n}} \cdot \nabla T(x, y = 0) = 0 \quad \text{and} \quad \vec{\mathbf{n}} \cdot \nabla \theta_w(x, y = 0) = 0, \quad (3.22)$$

where $\vec{\mathbf{n}}$ is the outward unit normal vector of the computational domain.

3.4.4 The inkjet deposition term j_{IJ}

An important aspect of the simulations is the implementation of the inkjet deposition. For a given drop frequency f , the droplet density per unit length of paper substrate is the smaller, the higher U_{IJ} . Therefore, for speeds U_{IJ} higher than a critical value $U_c(f)$, the moisture content will not reach the saturation value. In this regime, we implemented the droplet deposition as a flux function

$$j_{IJ}(x, y) = C_0 \text{flc2hs} \left(R_c - \sqrt{x^2 + y^2}, R_c/100 \right) \quad (3.23)$$

that is different from zero only in the blue circle sketched in Fig. 3.12. Here, the function $\text{flc2hs}(x, \epsilon)$ is a smoothed Heaviside function with transition width

ϵ . The prefactor C_0 is adjusted such that the area integral $\iint j_{IJ} dA$ equals the total mass deposition rate $\rho_w V_{drop} f$. We neglect the discrete nature of the individual droplets and assume that j_{IJ} is constant in time, i.e. it is effectively a time-averaged quantity.

For speeds $U_{IJ} < U_c(f)$, the water content will reach saturation. In this regime a Dirichlet boundary condition

$$\theta_w \left(\sqrt{x^2 + y^2} \leq R_c \right) = 0.99\theta_{w,\max} \quad (3.24)$$

was applied. The dimension of the sub-domain where the water content was kept constant (i.e. the radius R_c of the blue circle in Fig. 3.12) was adjusted such that the line integral of the Darcy flux over the circular arc

$$\int \rho_w \vec{v} \cdot \vec{n} dl = \rho_w V_{drop} f - \iint k_\infty (\rho_s - \rho_\infty) dA \quad (3.25)$$

was equal the mass deposition rate of the inkjet corrected for evaporative losses over the source region.

The initial condition for temperature was $T(x, y, t = 0) = T_{amb}$. Depending on whether U_{IJ} is smaller or larger than $U_c(f)$ and the moisture content reaches the maximum holding capacity, the initial condition for the moisture content was either $\theta_w(x, y, t = 0) = \theta_{w,amb}$ uniformly or

$$\theta_w(x, y, t = 0) = 0.99\theta_{w,\max} \quad \text{if} \quad \sqrt{x^2 + y^2} \leq R_c \quad (3.26)$$

$$\theta_w(x, y, t = 0) = \theta_{w,amb} \quad \text{if} \quad \sqrt{x^2 + y^2} > R_c \quad (3.27)$$

3.5 Discussion

In this section, the numerical results and some comparison with experimental results presented in 3.3 will be discussed for the cases of changing substrate speed, changing frequency of deposition and transient evolution of an inkjet deposited line.

3.5.1 The effect of the frequency of deposition

In this subsection we discuss the effect of the frequency of deposition for a constant substrate speed $U_{IJ} = 0.05$ mm/s. Figures 3.13(a,b) show two computed moisture content maps for frequencies of 100 and 500 Hz. In Fig. 3.13(c,d) we present longitudinal cross-sections of the moisture content distribution $\theta_w(x, y = 0)$ and the temperature distribution $\Delta T(x, y = 0)$ for different frequencies f .

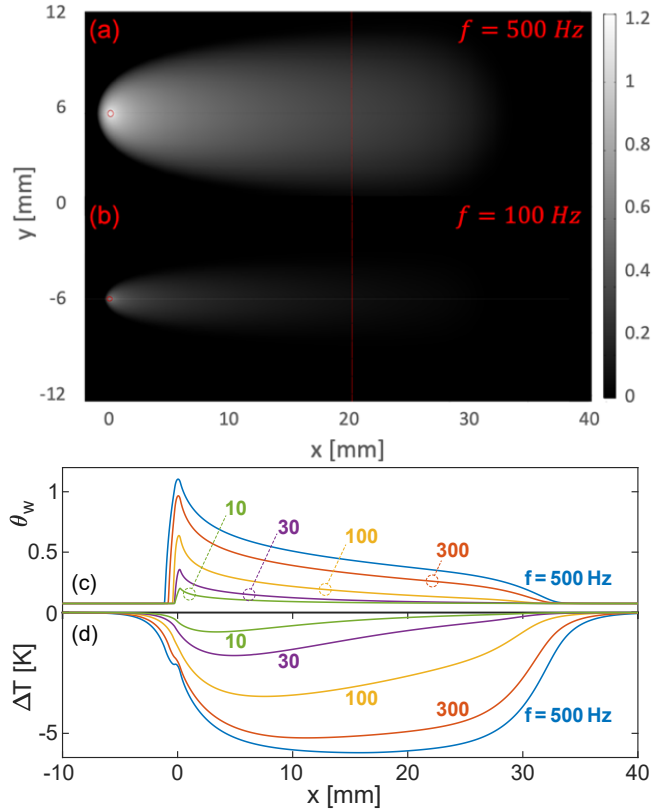


Figure 3.13: (a,b) Two-dimensional numerical simulations of the moisture distribution θ_w for $U_{IJ} = 0.05$ mm/s and two values of the deposition frequency $f = 500$ and 100 Hz. The data correspond to a printed length $U_{IJ}t = 3$ cm. The red circles represent the impingement point. (c,d) Longitudinal cross-sections of (c) the moisture content $\theta_w(x, y = 0)$ and (d) the temperature distribution $\Delta T(x, y = 0)$ for $U_{IJ} = 0.05$ mm/s and different frequencies f . The data correspond to a printed length $U_{IJ}t = 3$ cm.

Lower frequencies induce shorter and narrower moisture distributions, because a smaller quantity of water is deposited per unit length. For small f , the length of the wet zone l_{wet} can become significantly shorter than the printing distance $U_{IJ}t$. This is visible in Fig. 3.13(c) for $f \leq 100$ Hz, as well as in Fig. 3.6(b), where l_{wet} is plotted as a function of f . This also forces the minimum in temperature to occur closer to the impingement point as f decreases, consistent with Fig. 3.13(d).

In Fig. 3.6(a) we show the maximum moisture content $\max(\theta_w) - \theta_{amb}$, which occurs close to the impingement point, as a function of droplet frequency f for $U_{IJ} = 0.05$ mm/s and a printed length of $U_{IJ}t = 30$ mm. The numerical

simulations (red diamonds) agree well with the experimental data (blue asterisks). Also the numerical simulations (red diamonds) for the length of the wet zone l_{wet} as a function of f in Fig. 3.6(b) agree qualitatively well with the experimental data (blue asterisks), but appear to be displaced along the abscissa by a constant factor of 3. For large f , l_{wet} tends to saturate at a value that slightly exceeds the printed length $U_{IJ}t$, owing to wicking in the x -direction.

In Fig. 3.6(c) we present the maximum temperature difference ΔT_{max} as a function of frequency f . For large f , ΔT_{max} tends to saturate at a value determined by $q_{2D} = 0$, i.e. the balance of evaporative cooling and heat input from the ambient environment, see Eq. (3.16). In steady state, all other terms in Eq. (3.14) become negligible in the limit of large f , because the spatial temperature derivatives vanish, as a large zone of approximately uniform moisture content forms. In the limit of $f \rightarrow 0$, ΔT_{max} decreases. This is because the maximum moisture difference $\Delta\theta_{max} \equiv \theta_w - \theta_{amb}$ at the impingement point decreases with decreasing f (smaller liquid influx). Consequently, the term ρ_s in Eq. (3.16) stays closer to ρ_∞ , thus reducing the evaporative cooling.

3.5.2 The effects of the substrate velocity

In Fig. 3.14, we present two-dimensional numerical simulations of the moisture content θ_w and the corresponding temperature distributions ΔT for $U_{IJ} = 0.2$ mm/s and $f = 1000$ Hz at a time $t = 150$ s after commencement of deposition. The solid lines in Fig. 3.14(c,d) represent longitudinal cross-sections of the moisture content $\theta_w(x, y = 0)$ and the corresponding temperature distribution $\Delta T(x, y = 0)$ for a printed length $U_{IJ}t = 3$ cm and different values of U_{IJ} . The general shape of the curves closely resembles that of the experimental data in Fig. 3.8.

For low speeds, the moisture distribution is fully saturated near the impingement point $x = 0$, i.e. $\theta_w(x \approx 0) = \theta_{w,max}$. The length of this zone decreases as U_{IJ} increases, as in the experiments in Fig. 3.8. For low speeds, the temperature distribution in the wet zone becomes uniform, whereas for high speeds ΔT decreases with increasing x and exhibits a minimum near the end of the printed line $x = U_{IJ}t$. The temperature profiles reveal an interesting feature near the impingement point $x = 0$: a peak for high speed which resembles a shoulder for low U_{IJ} . It is caused by a combination of the heat of sorption described by Eq. (3.13) as well as the thermal mass of the deposited droplets described by the second term in Eq. (3.14). We have assumed that the inkjet-deposited droplets reach a temperature of $T_{IJ} = T_{amb} - 0.5$ K due to evaporative cooling along their flight path of 5 – 10 mm length. In the region close to $x = 0$, the

thermal influence of the liquid deposition from the printhead is felt strongest. The liquid in the printhead is at ambient temperature T_{amb} . According to the manufacturer, the initial ejection velocity of the drops at the nozzle is 2 m/s. Their flight distance is about 5 – 10 mm, during which in-flight evaporative cooling reduces the drop temperature. Droplets with a diameter of 40 μm reach their terminal velocity in the order of 5 cm/s within approximately 10 ms, [141] therefore a rough estimate of their flight time is 5 – 10 ms. Based on the results of Gonzalez Pedraza *et al.*, a reasonable estimate for the reduction of the droplet temperature is $T_{IJ} = T_{amb} - 0.5 \text{ K}$. [142] Although this is below ambient temperature, it is still significantly warmer than the temperature induced by evaporative cooling at the low speed values (typically 6 K below T_{amb}), and thus causes local heating. The sorptive heating term is more pronounced at high speeds, because the term $U_{IJ} \frac{\partial \theta_w}{\partial x}$ increases, whereas the thermal droplet mass effect dominates at low speeds when the term $T_{IJ} - T$ in Eq. (3.14) is highest. For a direct comparison of experiments and simulation we also plotted the measured data for $U_{IJ} = 0.05 \text{ mm/s}$ (dotted lines), which shows good agreement. Figure 3.9(a,b) shows the transverse widths (FWHM) of the moisture and the temperature distributions as a function of U_{IJ} , respectively. The data were extracted from two-dimensional maps of θ_w and ΔT as shown in Fig. 3.8(a,b) at a position $x = 2 \text{ cm}$ at different times when the printed line length was $U_{IJ}t = 3 \text{ cm}$. Blue stars correspond to experimental data, red open diamond to numerical simulations with fixed $H_p = 1 \text{ cm}$. The numerical results for y_w scale with substrate speed as $U_{IJ}^{-0.7}$, in perfect agreement with the experiments. The scaling of y_h , however, is stronger in the simulations compared to the experimental observations. A possible reason for the deviation is that we have assumed the heat transfer coefficient h_N to be constant. In Fig. 3.9(c) we present the maximum temperature drop ΔT_{\max} extracted from Fig. 3.8(d) as a function of U_{IJ} . Blue stars represent experimental data. Red open diamonds represent numerical simulations with a fixed mass transfer distance $H_p = 10 \text{ mm}$. Violet and green symbols correspond to $H_p = 5 \text{ mm}$ and 2 mm , respectively. The simulations match the experimental data very well up to a speed of approximately 1 mm/s. For higher speeds the simulations significantly underestimate the temperature amplitude. We attribute this discrepancy to a reduction of the mass transfer distance H_p that is induced by the progressively swifter substrate motion. Reducing H_p for the two highest speeds and thus increasing the evaporation rate, improves the agreement with the experiments.

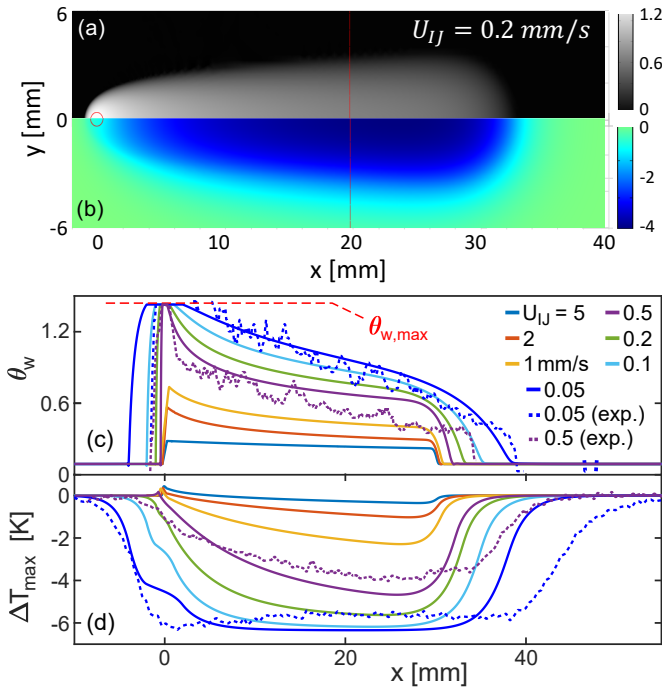


Figure 3.14: (a,b) Numerical simulations of (a) the moisture content θ_w and (b) the temperature distribution ΔT for $U_{IJ} = 0.2 \text{ mm/s}$ and $f = 1000 \text{ Hz}$ at a time $t = 150 \text{ s}$ after commencement of deposition. (c,d) Longitudinal cross-sections of (c) the moisture content $\theta_w(x, y = 0)$ and (d) the corresponding temperature distribution $\Delta T(x, y = 0)$ for a printed length $U_{IJ}t = 3 \text{ cm}$ and different values of U_{IJ} . Solid lines correspond to numerical simulations, the dotted lines are measured data for $U_{IJ} = 0.05 \text{ mm/s}$.

3.5.3 Transient evolution

The temporal evolution of the moisture distribution and the temperature is illustrated in Fig. 3.15 for the case of $f = 500 \text{ Hz}$ and $U_{IJ} = 0.05 \text{ mm/s}$. Near the origin, the deposition process causes the moisture content to quickly increase with time. At a time of $t \approx 2R_c/U_{IJ} \approx 10 \text{ s}$, $\theta_w(0, 0)$ begins to saturate, whereas the length of the wet zone keeps increasing, until l_{wet} reaches a steady-state value that depends on deposition frequency and substrate velocity as visible in Fig. 3.16(a). The temperature distribution develops a bell-shaped antipeak with the temperature minimum located initially near the impingement point. As time increases, the antipeak deepens until ΔT_{max} reaches a steady value. Due to the low substrate speed, an effect of the heat of wetting is not noticeable. The shoulder at $x = 0$ is induced by the thermal mass of the deposited droplets with temperature T_{IJ} .

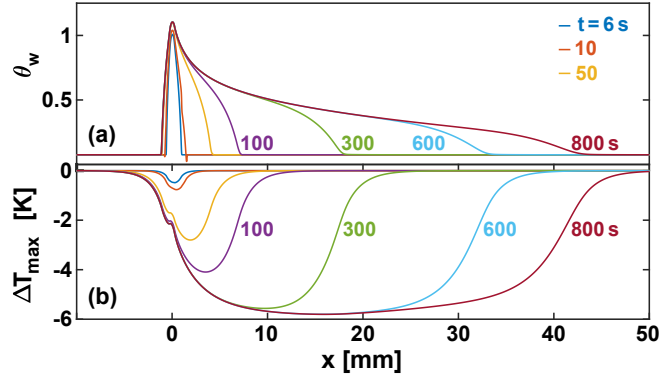


Figure 3.15: Longitudinal cross-sections of (a) the moisture content $\theta_w(x, y = 0)$ and (b) the temperature distribution $\Delta T(x, y = 0)$ for different times after commencement of printing. The data correspond to $f = 500$ Hz and $U_{IJ} = 0.05$ mm/s.

The slope of the curves in the double-logarithmic plot in Fig. 3.16(a) is sublinear prior to saturation, due to the low substrate speed. This is perfectly consistent with the experimental behavior seen in Fig. 3.11(a). There is no saturation visible in Fig. 3.16(b) owing to the high drop frequency of $f = 1000$ Hz. For high substrate speeds such as $U_{IJ} = 2$ mm/s, l_{wet} increases linearly in time. In contrast, for low speeds and primarily for early times a powerlaw exponent of 0.5 is a better match, which is due to the effect of wicking. The maximum temperature amplitudes $\Delta T_{max}(t)$ in Fig. 3.16(c,d) are lower for lower frequencies and higher substrate speeds, as in both limits the moisture content is lower, which corresponds to a lower vapor pressure and thus reduced evaporative cooling. The fact that the curves for $U_{IJ} \leq 0.5$ mm/s approximately collapse in Fig. 3.16(d) in the interval $10 \leq t \leq 50$ s can be understood from a Lagrangian viewpoint. An area element of the paper substrate receives an identical initial moisture content of $\theta_{w,max}$ at the impingement point [see Fig. 3.8(a) or Fig. 3.14(a)] and subsequently undergoes approximately the same temperature change in the same time. The collapse is not perfect due to the different degree with which wicking affects the moisture redistribution.

3.5.4 Scaling behavior

The numerical data in Fig. 3.9(c) suggest that $\Delta T_{max} \sim U_{IJ}^{-1}$ for large U_{IJ} and a constant value of H_p . This can be rationalized by considering the fact that the spatial gradients of θ_w in the x -direction decrease for increasing U_{IJ} (high Peclet numbers), as can be seen clearly in Fig. 3.14(c). This means that the term ρ_s in Eq. (3.16) becomes constant and thus a uniform cooling heat flux

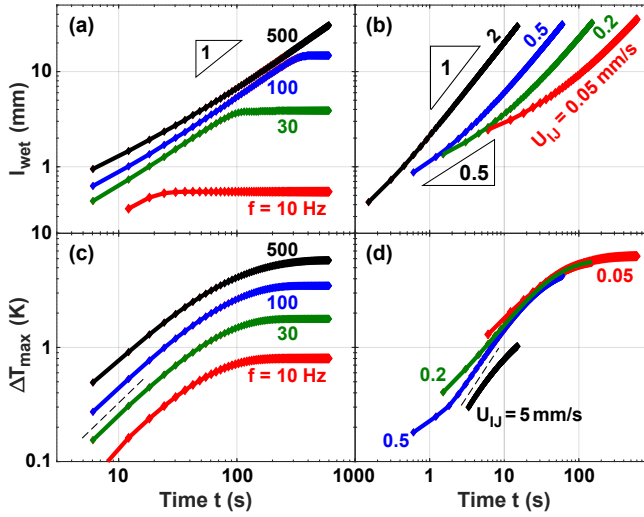


Figure 3.16: Temporal evolution of (a,c) the length of the wet zone $l_{wet}(t)$ and (b,d) the maximum temperature amplitude $\Delta T_{max}(t)$ for different values of (a,b) the drop frequency f and (c,d) the substrate speed U_{IJ} . The substrate speed in (a,c) was $U_{IJ} = 0.05$ mm/s and the drop frequency in (b,d) was $f = 1000$ Hz.

results along the wet zone. For increasing U_{IJ} the temperature drop $|\Delta T|$ at a fixed value of x decreases. Consequently, the maximum temperature amplitude remains below saturation and the heat exchange term with the ambient can be neglected in Eq. (3.16) in the limit of large U_{IJ} . In Eq. (3.14) the sorptive term is negligible for a uniform θ_w , the conduction term is negligible in the limit of high thermal Peclet numbers and the second term does not play a role at the end of the printed line $x \approx l_{wet}$, because j_{IJ} is zero there. The balance of the remaining terms in Eq. (3.14) indeed yields a temperature amplitude inversely proportional to U_{IJ} .

3.5.5 Including the gas phase – 3D simulations

Murali *et al.* explicitly incorporated the gas phase in their model and found an intricate interplay of buoyancy effects and substrate-motion induced convection regarding moisture transport. [119] The incorporation of the gas phase on top of the paper into the present 2D model of the paper domain would require 3D simulations with a large gas domain to reproduce buoyancy effects. This turned out to be computationally too expensive. Moreover, the stream of inkjetted droplets induces gas phase convection (typical speed 1 m/s, which may suppress or overshadow the buoyancy-induced flows that would be present in a stagnant

atmosphere (on order 5 mm/s [119, 143]).

Therefore, we accounted for heat and mass exchange with the ambient atmosphere via the heat- and mass transfer coefficients h_N and k_∞ . This implies that our model does not take recondensation effects into account, which would induce extra heating in the vicinity of the wet-dry boundaries. [119] However, such recondensation effects are not prominently visible in the infrared data. Our model reproduces evaporative cooling to the extent that the linear mass transfer law with constant k_∞ is realistic. The values of k_∞ and h_N are, however, expected to increase with increasing U_{IJ} and f , because both factors increase convection in the ambient atmosphere.

3.6 Summary and conclusions

We have systematically studied the deposition of lines of water by means of inkjet printing onto paper substrates. Water is used because it is the main constituent of eco-friendly aqueous-based inks. We used optical transmission imaging to determine the moisture distribution and infrared thermography to obtain the temperature distribution as well as their time-dependencies. Moreover, we have developed a numerical model coupling unsaturated flow in thin porous media with evaporative mass loss and heat transfer. The numerical simulations could reproduce most of the experimental results well. This combination of experiments and numerical simulations gives comprehensive insight into the water penetration dynamics in the paper substrate. The latter determines the coalescence time scale of latex-based ink patterns [144] and is thus at the heart of achieving high resolution and pattern fidelity.

Acknowledgements

This work is part of the research programme ‘*The role of surfactants in spreading, imbibition and sorption of water-based printing inks*’ with project number 14666, which is (partly) financed by the Netherlands Organisation for Scientific Research (NWO). The author thanks Nicolae Tomozeiu and Herman Wijshoff of Canon Production Printing for the fruitful discussion sessions. The author is grateful to Gerald Oerlemans for helping with the design of the ink-jet holder that has lead to a substantial increase in the degrees of freedom in setting-up of and imaging the inkjet deposition process. Jorgen van der Veen is thanked for his suggestions towards choosing the appropriate camera and optical accessories needed for successful completion of the experiments in this chapter.

Contribution statement

The results discussed in this chapter are from the publication Ref. [145]. The author of this thesis developed the experimental set-up, the calibration procedures and the measurement protocols. The author conducted and performed all the experiments and analyzed all the experimental data. The theoretical model discussed was a joint effort between the author and his theoretical counterpart Venditti, G. The latter performed all the numerical simulations and analyzed the numerical data that were discussed in this chapter. Both the author and his theoretical counterpart wrote the aforementioned manuscript.

Table 3.2: List of symbols and parameters

Symbol	Name	Value	Units
a_w	Water activity	-	-
c_g	GAB Isotherm constant	18.647	-
$c_{p,av}$	Average specific heat capacity	-	J/kgK
$c_{p,s}$	Specific heat capacity of solid	1400	J/kgK
$c_{p,w}$	Specific heat capacity of water	4180	J/kgK
C_1	Prefactor of heat of wetting	$1.5 \cdot 10^6$	J/kg
C_2	Coefficient of heat of wetting	40	-
D_{H_2O}	Water vapour diffusivity in air	$2.8 \cdot 10^{-5}$	m^2/s
ΔH_s	Heat of wetting	-	J/kg
E_{evap}	Enthalphy of evaporation of water	$2.44 \cdot 10^6$	J/kg
f	Deposition frequency	-	Hz
h_N	Heat transfer coefficient	9	W/m^2K
H_p	Convection length scale	-	m
I	Transmitted light intensity	-	-
I_0	Primary light intensity	-	-
j	Total mass flux of water vapor	-	kg/m^3s
j_{IJ}	Mass influx of deposited droplets	-	kg/m^3s
k	GAB isotherm constant	0.85	-
k_{air}	Thermal conductivity of air	0.025	W/mK
k_{av}	Average thermal conductivity	-	W/mK
k_c	Relative permeability parameter	0.3	-
K_{rw}	Relative permeability	-	-
k_s	Thermal conductivity of solid	0.4	W/mK
K_s	Absolute permeability	$1.2 \cdot 10^{-12}$	m^2
k_w	Thermal conductivity of water	0.6	W/mK
k_∞	Mass transfer coefficient	$2.8 \cdot 10^{-3}$	m/s
l_{wet}	Length of the wet zone.	-	m/s
M_0	GAB isotherm parameter	0.061	-
m_g	Van Genuchten exponent	$1-1/n_g$	-
M_w	Molar mass of water	$18 \cdot 10^{-3}$	kg/mol
n_g	Capillary pressure exponent	4	-
p_{amb}	Ambient pressure	$1 \cdot 10^5$	Pa
p_g	Pressure scaling parameter	-2000	Pa
p_{sat}	Saturation vapor pressure	-	Pa
p_w	Pressure of water phase	-	Pa
q_{2D}	Heat source	-	W/m^3
R	Gas constant	8.314	$J/(Kmol)$
R_c	Radius of deposition zone	-	m
RH	Ambient relative humidity	0.3	-
T	Temperature of porous medium	-	K
T_{amb}	Ambient temperature	298.15	K
T_{ij}	Droplet temperature	297.65	K
t_p	Paper thickness	0.1	mm
$\langle \vec{u} \rangle$	Darcy velocity	-	m/s
U_{IJ}	Speed of the substrate	-	m/s
x	Longitudinal coordinate	-	m
y	Transverse coordinate	-	m
μ_w	Dynamic viscosity of water	$8.9 \cdot 10^{-4}$	$Pa \cdot s$
ρ_{av}	Volume averaged density	-	kg/m^3
ρ_s	Mass density of solid	1500	kg/m^3
ρ_{sat}	Saturation conc. of water vapor	0.02287	kg/m^3
ρ_w	Mass density of water	1000	kg/m^3
ϕ	Porosity	-	-
θ_{amb}	Equil. moisture content @ $RH=0.3$	-	kg/kg
θ_w	Moisture content	-	kg/kg
$\theta_{w,max}$	Maximum moisture content	1.21	kg/kg
Θ_s	Area mass density of dry paper	77	g/m^2
Θ_w	Area mass density of water	-	g/m^2
$\Theta_{w,max}$	Maximum water holding capacity	94	g/m^2

Chapter 4

Inkjet deposition of lines of surfactant solutions onto thin moving porous media

In this chapter, the role of surfactants in inkjet printing is explored. The combined imbibition and evaporation of surfactant solutions into thin porous media are studied by means of experiments and numerical simulations. Solutions of anionic and non-ionic surfactants were deposited onto moving sheets of paper by a droplet-on-demand inkjet system. Drop casting experiments, where a drop of surfactant solutions, cast onto a stationary substrate guide the interpretation of the inkjet deposition experiments. Optical transmission imaging and infrared thermography were used to monitor the lateral transport and evaporation of the surfactant-laden solutions. The description of the experimental procedure, the discussion of the results obtained and some comparison with the numerical model developed by the theoretical counterpart of this work form the crux of this chapter.

4.1 Introduction

Surfactants are added to inkjet inks for a number of reasons [146]. They tend to affect the contact angle on partially wetting substrates [147–157] and thus control the ink wettability and the degree of droplet spreading [158, 159]. Surfactants can be used also as a dispersion agents that improve the colloidal suspension stability of colorant pigment particles [160]. Surfactants can serve as emulsifiers [161], desizing or anti-foaming agents [162] or promote the solubilization of dyes. Surfactants can reduce inter-color bleed [163, 164] and improve the ejection stability of ink droplets [165]. Usually more than one surfactant species is present in a commercial ink formulation, and typically concentrations above the critical micelle concentration (cmc) are used.

Tschapek and Boggio showed that inhomogeneous surfactant distributions

cause moisture migration in unsaturated porous media [166]. Zartman and Bartsch used anionic, cationic, and non-ionic surfactants in dewatering experiments of unsaturated sand columns and found no significant performance difference between the different classes of surfactants [167]. In contrast, Karkare *et al.* found considerable differences in the water displacement efficiencies of a large number of long-chain ionic and non-ionic surfactant species [168]. They showed that there is a strong correlation between water displacement and the equilibrium spreading pressure for a subset of surfactants, but not all species adhered to it. Karkare and Fort showed that the water displacement showed a strong correlation with the capillary pressure differences induced by the inhomogeneous surfactant distribution [169]. Smith and Gillham [170] and Henry *et al.* [171] considered the effect of soluble surface-active species. Brown *et al.* [172], Henry *et al.* [173,174] and Rathfelder *et al.* [175] performed two- and three-dimensional simulations of surfactant-induced flows in bulk porous media in the context of contaminant transport and aquifer remediation. Hodgson and Berg [176] studied the wicking of surfactant solutions into paper sheets by means of systematic experiments using anionic, cationic and non-ionic surfactants. In all cases, a Washburn-like scaling of the front position $h \sim kt^{1/2}$ was found. The variation of the prefactor k with surfactant concentration indicated the importance of surfactant depletion near the wetting front due to adsorption on the fiber walls.

Several authors have studied the simultaneous spreading and imbibition of droplets on porous substrates [8, 26, 149, 177–187]. However, the ambition and focus of these studies was primarily on an accurate and in-depth description of the dynamics of the liquid films and droplets on top of the substrate and less on the details of solvent loss due to imbibition and evaporation. In contrast, the ambition and focus of this manuscript is on an in-depth description of the moisture and multi-component transport inside the porous medium. We study the deposition of lines of inkjet-deposited droplets of an aqueous surfactant solution on a moving paper substrate by means of experiments and numerical simulations. We use light transmission [120] and infrared thermography [119] to characterize the moisture and temperature distributions due to wicking and evaporative cooling. In our model, we disregard the presence of liquid on top of the paper and thus effectively focus on the late stage of the simultaneous processes of imbibition of a surfactant solution into a paper substrate and evaporation of the solvent. We use a dual-porosity model of unsaturated flow based on the Richards equation, which explicitly accounts for the exchange between liquid residing in the pores and in the paper fibers. Moreover, we solve for surfactant adsorption on the fibers as well as for heat transfer to compare

with the thermography measurements.

4.2 Materials and methods

We have used the same experimental setup and procedures for inkjet printing onto a horizontal, moving sheet of paper at a constant droplet frequency as described in detail in Ref. [145] (see also previous chapter). The horizontal speed of motion U_{IJ} was varied between 0.05–5 mm/s. The paper types studied are Mondi DNS HSI CF (calendered, thickness $t_p = 93 \mu\text{m}$) and Mondi DNS HSI NF (thickness $t_p = 104 \mu\text{m}$) printing papers, which both contain CaCl_2 to aid the inkjet print quality.

4.2.1 Surfactant properties

As surfactants we have used sodium dodecyl sulfate (SDS, Sigma-Aldrich, product number 436143, molecular weight (MW) 288.38 g/mol) and Triton X-100 (Sigma-Aldrich, product number T9284, average MW 625 g/mol), which are anionic and non-ionic, respectively.

The surface tension of solutions of soluble surfactants depends sensitively on the surfactant bulk concentration c . It starts from the surface tension of pure water for $c = 0$ and decreases to an asymptotic value γ_∞ for c exceeding the so-called critical micelle concentration (cmc). The cmc of SDS is 8.1 mM or 0.234 wt%, that of Triton X-100 is 0.24 mM or 0.019 wt% [188, 189]. The value of γ_∞ of SDS depends on the purity of the material - literature values range between 34 and 38 mN/m. [188, 190, 191] A comparable variation is observed for Triton X-100 [189, 192, 193].

The viscosity of SDS solutions is only a very weak function of concentration. Up to 15 cmc the viscosity increases only by 30% compared to the value of pure water [194]. The following linear fit is an accurate representation of the data in Ref. [194]

$$\mu_{\text{SDS}} = \mu_{\text{H}_2\text{O}}(0.003002 c[\text{mM}] + 0.9756) . \quad (4.1)$$

For Triton X-100, Pal has measured the viscosity up to a weight fraction of 26% [195]. We used the following fit/extrapolation to the data in Ref. [195]

$$\mu_{\text{TX100}} = \mu_{\text{H}_2\text{O}} \exp\left(0.03791 \frac{c}{\text{cmc}}\right). \quad (4.2)$$

The molecular diffusion coefficient D_m of SDS varies between $(2-8) \cdot 10^{-10} \text{ m}^2/\text{s}$ for concentrations up to 13.5 wt% [196]. That of Triton X-100 drops from $D_m = 3 \cdot 10^{-10} \text{ m}^2/\text{s}$ for values below the cmc to $0.8 \cdot 10^{-10} \text{ m}^2/\text{s}$ for concentrations up to 1 wt% [197].

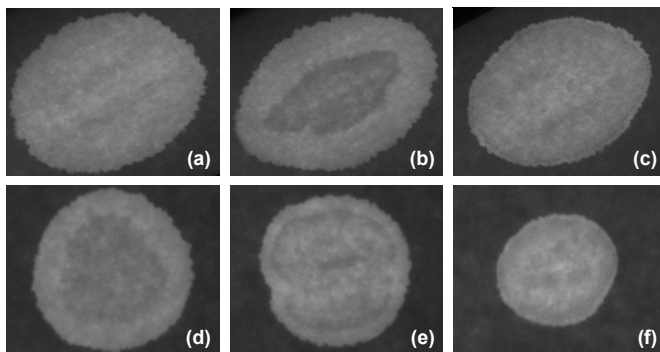


Figure 4.1: Optical transmission images of wet zones in stationary NF paper substrates 300 s after deposition of $5\ \mu\text{l}$ droplets of (a) pure water and (b,c) SDS solutions of concentration $c = 1$ and $10\ \text{cmc}$, respectively. (d-f) Same for Triton X-100 solutions of concentration $c = 2, 5$ and $10\ \text{cmc}$, respectively, but non-constant droplet volumes.

4.2.2 Surfactant adsorption

Paria *et al.* measured the adsorption of Triton X-100 and sodiumdodecylbenzenesulfonate (SDBS) onto filter paper [198]. The best-fit values for the sorption capacity are $C_\infty = 0.75\ \text{mg}/(\text{g cellulose})$ for Triton X-100 and $C_\infty = 0.3\ \text{mg}/\text{g}$ for SDBS, respectively. We expect that the corresponding value for SDS is slightly lower than that of SDBS.

Hodgson and Berg [176] reported on depletion of surfactant at the spreading front due to its adsorption on the paper fibers during wicking. Only for concentrations exceeding the cmc could this depletion be overcome. They quantified this effect by determining the wicking-equivalent surface tension [176], but did not provide any direct visualization or measurement of the surfactant distribution. Figure 4.1 shows optical transmission images of wet zones in a paper substrate after deposition of droplets of pure water and surfactant solutions of various concentrations. The wet zone for pure water [Fig. 4.1(a)] is characterized by a relatively homogeneous grayscale value. In contrast, the presence of surfactants induces the formation of sharp grayscale transitions, which we attribute to the presence of well-defined fronts in the surfactant distribution, beyond which surfactant is essentially not present. For a $1\ \text{cmc}$ SDS solution [Fig. 4.1(b)] the extension of the dark region coincides with the maximum footprint area of the droplet deposited on top of the paper. For a $10\ \text{cmc}$ SDS solution [Fig. 4.1(c)] a dark ring is visible close to the perimeter of the wet zone, i.e. the SDS front has reached much further distances from the point of deposition, consistent with the observations of Hodgson and Berg [176]. The equivalent behavior is observed for Triton X-100 solutions of increasing con-

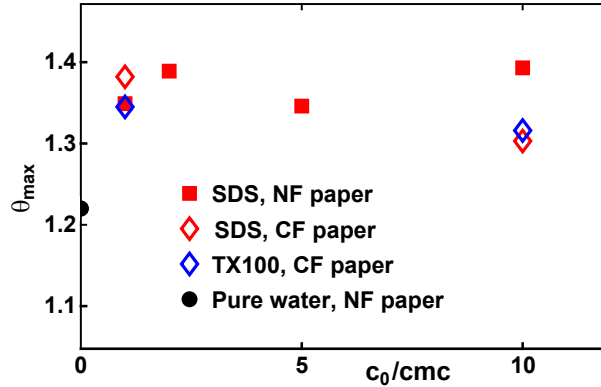


Figure 4.2: Maximum holding capacity θ_{max} for CF and NF paper as a function of initial surfactant concentration c_0 for both SDS and Triton X-100 solutions.

centration in Fig. 4.1(d-f). The physical origin of the darkening is discussed in Section 4.2.5.

4.2.3 Evaporation of surfactant solutions

It is well known that surfactants can retard the evaporation of water by up to 65% [199–202]. This, however, holds for insoluble surfactants that form a closed monolayer at the liquid-air interface at sufficiently high surface pressures. Soluble surfactants do not produce a measurable reduction of evaporation [203, 204]. This is consistent with the water vapor pressure p_{vap} of aqueous solutions of soluble surfactants being only a very weak function of concentration c up to several mol/kg. In this manuscript we are primarily interested in the moisture penetration dynamics, rather than the ink-solidification phase (i.e. the complete dry-out). Therefore, we neglect any dependence of p_{vap} on c [205–207] and assume that the moisture sorption isotherm of pure water [119] also applies to the drying of paper containing an imbibed surfactant solution.

4.2.4 Maximum holding capacity of paper

Figure 4.2 shows measurements of the dimensionless maximum holding capacity θ_{max} (units: kg of water per kg of dry paper) of CF and NF paper types as a function of the surfactant concentration for both SDS and Triton X-100. The quantity θ_{max} is determined by the ratio of the maximum amount of liquid that can be contained in the paper

$$\Theta_{tot,max} \equiv \Theta_{w,max} + \Theta_{f,max}$$

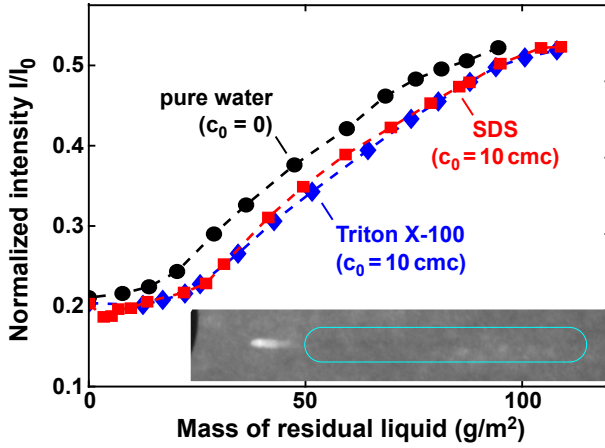


Figure 4.3: Normalized transmitted intensity I/I_0 of NF paper as a function of the residual mass of liquid for an SDS solution ($c_0 = 10$ cmc), a Triton X-100 solution ($c_0 = 10$ cmc) and pure water. Inset: snapshot corresponding to 300 s after commencement of deposition of a Triton X-100 solution ($c_0 = 70$ cmc) printed at $U_{IJ} = 0.05$ mm/s and with $\dot{m} = 0.78$ $\mu\text{g/s}$ on CF paper.

(units kg/m^2) and the mass of the dry paper sample initially in equilibrium with the ambient atmosphere $\Theta_s \approx 77$ g/m^2 . Here, $\Theta_{w,max}$ and $\Theta_{f,max}$ are the maximum holding capacities of the pores and the permeable fibers, respectively. The measurement procedure is described in detail in Ref. [145]. For an initial surfactant concentration c_0 exceeding 1 cmc, the value of θ_{max} remains approximately constant for both SDS and Triton X-100 and is approximately $(12 \pm 3)\%$ higher than for pure water ($c = 0$). Shepherd and Xiao [208] and Kim and Hsieh [209] observed a comparable increase of the absorption capacity of paper towels and cotton fabrics upon addition of certain surfactants. Shepherd and Xiao [208] attribute this effect to an increased debonding of the fiber network, that allows individual fibers to swell more.

4.2.5 Calibration of transmitted intensity vs. moisture content

Figure 4.3 shows quasi-equilibrium values of the transmitted intensity normalized by the incident intensity I/I_0 as a function of the mass of the residual liquid. The calibration procedure relies on the slow evaporation of the aqueous phase to attain different values of moisture content and is described in detail in Ref. [145]. The shape of the curve and the span of the data on the ordinate closely resemble results for Whatman filter paper by Forughi *et al.* [120]. The normalized intensity obtained with SDS and Triton X-100 solutions is slightly

lower compared to that of pure water. The origin of this reduction is unclear. Possible hypotheses are listed in Section. 4.2.6. It is, however, evident that the variation of the moisture content has a far greater influence on I/I_0 than the presence of SDS or Triton X-100 surfactants, even at concentrations exceeding 10 cmc.

The maximum attained transmission intensity is approximately the same for pure water and the surfactant solutions. At very low moisture contents, the transmission signal becomes darker than that of dry paper. The inset in Fig. 4.3 shows a contrast-enhanced transmission image of a line printed at $U_{IJ} = 0.05$ mm/s with a rather high Triton X-100 surfactant concentration of $c_0 = 70$ cmc. To the right of the wet zone, a dark line is visible as indicated by the bluish-green rectangle. We ascribe it to the reduction of light transmission caused by residual surfactant after the water has evaporated.

Surprisingly, during inkjet printing, the transmission intensities for surfactant solutions were routinely observed to be significantly *higher* than the calibrated quasi-equilibrium values shown in Fig. 4.3, especially for large deposition rates per unit length. This intensity overshoot is most pronounced close to the impingement point. We verified that it is not caused by residual liquid on top of the papersheet that has not been imbibed, yet. Fig. 4.4 shows optical reflection images of lines being printed at $U_{IJ} = 0.05$ mm/s for different values of the mass-deposition rate \dot{m} for a solution of SDS with a concentration $c_0 = 10$ cmc. It is clearly seen that only for \dot{m} values greater than $50 \mu\text{g/s}$ the pooling of liquid on top of the substrate occurs. The systematic results that will be discussed in the forthcoming sections are performed at an \dot{m} equal to $26 \mu\text{g/s}$, which negates the formation of the liquid pool on top of the substrate.

The overshoot unfortunately precludes a conversion of I/I_0 to θ_w for surfactant solutions, which was possible for inkjet printing of pure water [145]. We conclude that SDS and Triton X-100 solutions require a substantially longer time for quasi-equilibration in a paper matrix than pure water. We suspect that the rate limiting step may be the transfer of surfactants from the pores to the interior of the fibers [210].

4.2.6 Possible reasons for surfactant-induced reduction of light transmission

A higher degree of swelling induced by the presence of surfactants, which would be consistent with the increased holding capacity described in section 4.2.4. More swelling implies a larger paper thickness, which according to the Beer-Lambert law would result in an exponentially lower transmission. Shepherd and Xiao [208] concluded that the presence of most surfactants increases the

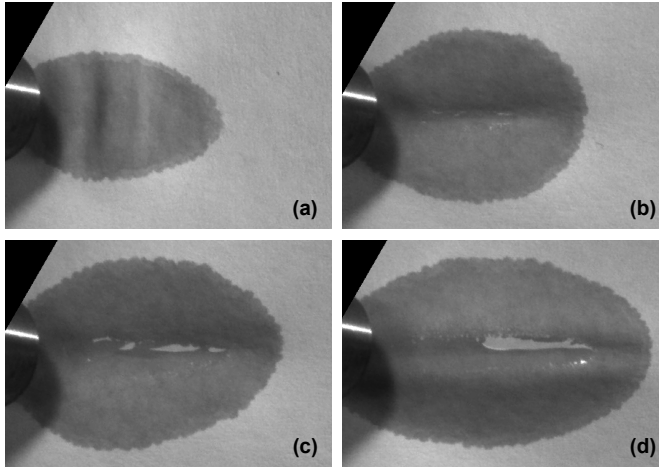


Figure 4.4: Top-view reflection images of the wet zone after printing an SDS solution ($c_0 = 10 \text{ cmc}$) on coated paper for a deposition time $t_d \approx 150 \text{ s}$ and different mass deposition rates \dot{m} of (a) 26, (b) 52, (c) 78 and (d) $104 \mu\text{g/s}$. Image width approx. 24 mm.

fraction of water residing in the fibers compared to that in the pores. Since light scattering is determined by the material interfaces with the highest refractive index contrast (the cellulose-air interface in the case of paper), shifting water from the pores to the interior of the fibers will tend to reduce transmission.

4.3 Experimental results

In our experiments we systematically varied the substrate speed U_{IJ} , the deposition rate \dot{m} (proportional to droplet frequency), the initial surfactant concentration c_0 and the paper type.

4.3.1 Variation of substrate speed

Figure 4.5 shows optical transmission images and corresponding temperature distributions of lines of SDS and Triton X-100 surfactant solutions printed at a constant mass deposition rate $\dot{m} = 26 \mu\text{g/s}$ and different values of the substrate speed U_{IJ} ranging from 0.05 to 5 mm/s. In Fig. 4.6 we present longitudinal cross-sections of the optical transmission signal $I(x, y = 0, t_d)/I_0$ and the temperature change $\Delta T(x, y = 0, t_d) \equiv T(x, y = 0, t_d) - T_{amb}$ for SDS and Triton X-100 solutions of initial concentration $c = 10 \text{ cmc}$ for a constant mass deposition rate $\dot{m} = 26 \mu\text{g/s}$ and different values of the substrate speed ranging from $U_{IJ} = 0.05$ to 5 mm/s. The deposition time t_d was varied to maintain

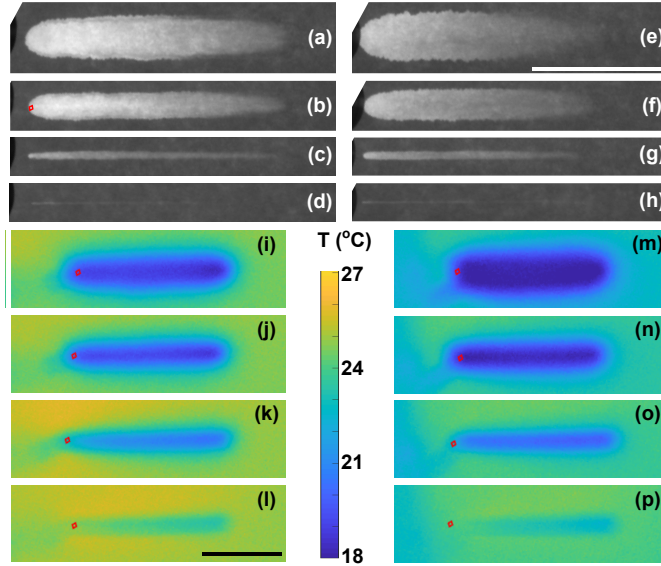


Figure 4.5: Optical transmission images of lines printed with (a-d) SDS and (e-h) Triton X-100 solutions of concentration $c = 10$ cmc. (i-p) Corresponding temperature distributions for SDS (i-l) and Triton X-100 (m-p). The red diamonds indicate the position of the jet impingement point $(x, y) = (0, 0)$. The mass deposition rate \dot{m} was $26 \mu\text{g/s}$. The scalebars in (e) and (l) correspond to 2 cm and apply to all transmission and IR images. The substrate speeds were $U_{IJ} = 0.05$ (a,r,i,m), 0.1 (b,f,j,n), 0.5 (c,g,k,o) and 5 mm/s (d,h,l,p). All images were obtained with CF paper.

a constant printing distance $U_{IJ}t_d = 4$ cm. We note that the fluctuations in Fig. 4.6(a,b) are not noise, but rather reflect random heterogeneities of paper. SDS exhibits a noticeably higher intensity overshoot than Triton X-100 in Fig. 4.6(a,b), which is also reflected in the higher brightness levels of Figs. 4.5(a,b) compared to (e,f).

Figure 4.7 shows the dependence of the transverse full-width at half-maximum values (FWHMs) of the moisture and temperature distributions, Δy_w and Δy_h , as well as the maximum cooling amplitude along the centerline i.e. $|\Delta T|_{\max} \equiv \max(|\Delta T(x, y = 0, t_d)|)$ as a function of the substrate speed U_{IJ} . The dashed line in Fig. 4.11 represents a powerlaw relation $\Delta y_w \sim U_{IJ}^{0.75}$, which is a good approximation to the data. There appears to be no systematic difference in Δy_w or Δy_h between experiments with SDS or Triton X-100. However, SDS systematically induces lower cooling amplitudes than Triton X-100 at $c_0 = 10$ cmc for substrate speeds $U_{IJ} \geq 0.5$ mm/s. SDS is an ionic surfactant that essentially completely dissociates in water, whereas Triton X-100 is a non-ionic surfactant which does not dissociate. Moreover, the cmc of SDS (8 mM) is

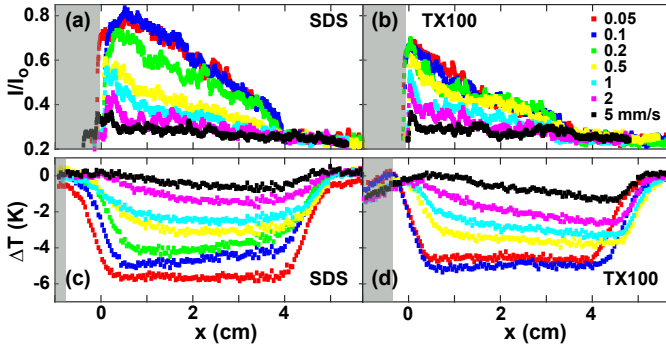


Figure 4.6: Longitudinal cross-sections of the optical transmission data $I(x, y = 0, t_d)/I_0$ of 4 cm long lines printed on CF paper with (a) SDS and (b) Triton X-100 solutions of initial concentration $c_0 = 10$ cmc for different values of the substrate speed ranging from $U_{IJ} = 0.05$ to 5 mm/s. (c,d) Corresponding longitudinal cross-sections of the temperature distributions $\Delta T(x, y = 0, t_d)$ for (c) SDS and (d) Triton X-100. The gray shaded rectangles indicate the location of the printhead. The mass deposition rate was kept constant at $\dot{m} = 26 \mu\text{g/s}$.

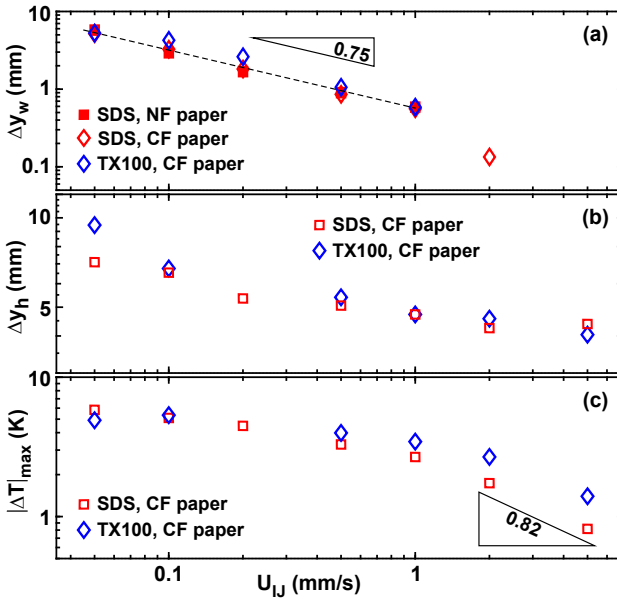


Figure 4.7: (a,b) Transverse FWHM of (a) the moisture distribution Δy_w and (b) the temperature distribution Δy_h as a function of U_{IJ} . The data were obtained at position $x = 2$ cm for a printing distance of $\Delta x = U_{IJ}t_d = 4$ cm. (c) Maximum cooling amplitude $|\Delta T|_{\text{max}}$ as a function of U_{IJ} . Red symbols represent SDS, blue diamonds Triton X-100 solutions of initial concentration $c_0 = 10$ cmc. All experiments were performed with a constant mass deposition rate of $\dot{m} = 26 \mu\text{g/s}$.

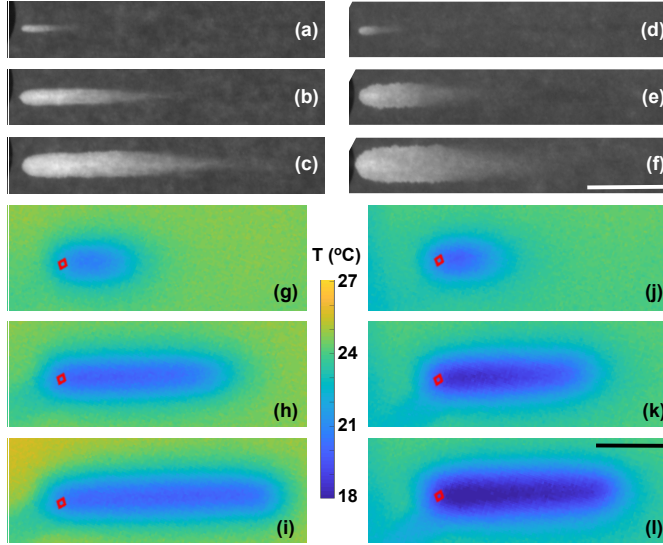


Figure 4.8: Optical transmission images of lines printed with (a-c) SDS and (d-f) Triton X-100 solutions of concentration $c_0 = 10 \text{ cmc}$. (g-l) Corresponding temperature distributions for SDS (g-i) and Triton X-100 (j-l). The red diamonds indicate the position of the jet impingement point $(x, y) = (0, 0)$. The scalebars correspond to 2 cm. The substrate speed was $U_{IJ} = 0.05 \text{ mm/s}$ and the printed length $U_{IJ}t_d = 3 \text{ cm}$. The mass deposition rates were 2.6 (a,d,g,j), 7.8 (b,e,h,k) and $13 \mu\text{g/s}$ (c,f,i,l). All SDS experiments were performed with NF paper and all Triton X-100 experiments with CF paper. The scalebars in (f) and (l) represent 1 cm.

much higher than that of Triton X-100 (0.23 mM). For both reasons one would expect a stronger reduction of the vapor pressure p_{vap} for SDS according to Raoult's law. Nevertheless this is not the reason for the observed difference in $|\Delta T|_{\max}$, because p_{vap} of SDS solutions decreases by less than 1% up to concentrations of 1.8 M [211].

4.3.2 Variation of deposition rate

Figure 4.8 shows optical transmission images and corresponding temperature distributions of lines of SDS and Triton X-100 solutions of initial concentration $c_0 = 10 \text{ cmc}$ printed with a constant substrate speed $U_{IJ} = 0.05 \text{ mm/s}$ and different values of the mass deposition rate \dot{m} . It is apparent that the transverse width of lines printed with the Triton X-100 solution on CF paper is systematically larger than for the SDS solution on NF paper, for all values of \dot{m} shown. At the same time, the transmitted intensity in the vicinity of the impingement point is again systematically higher for SDS than for Triton

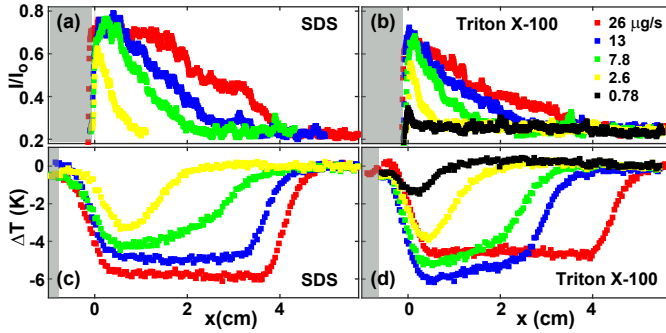


Figure 4.9: Longitudinal cross-sections of the optical transmission data $I(x, y = 0, t_d)/I_0$ of lines printed with (a) SDS on NF paper and (b) Triton X-100 on CF paper with initial concentration $c_0 = 10$ cmc for different values of the mass deposition rate ranging from $\dot{m} = 0.78$ to $26 \mu\text{g/s}$. (c,d) Corresponding longitudinal cross-sections of the temperature distributions $\Delta T(x, y = 0, t_d)$ for (c) SDS and (d) Triton X-100. The gray shaded rectangles indicate the location of the printhead. The substrate speed and the line length were kept constant at $U_{IJ} = 0.05$ mm/s and 3 cm, respectively.

X-100 at high values of \dot{m} .

Figures 4.9(a,b) show longitudinal cross-sections of the normalized transmission intensity $I(x, y = 0, t_d)/I_0$ along the centerline, while Figs. 4.9(c,d) show the corresponding temperature distribution $\Delta T(x, y = 0, t_d)$.

Figure 4.10 presents the dependence of the maximum cooling amplitude $|\Delta T|_{\max}$ and the length of the wet zone l_{wet} on the mass deposition rate \dot{m} . The parameter l_{wet} is defined as the distance along which I/I_0 remains above a level of 0.3. The values of $|\Delta T|_{\max}$ and l_{wet} are rather similar for SDS and Triton X-100 for $c_0 = 10$ cmc. The horizontal green line in Fig. 4.10(b) corresponds to the printing distance $U_{IJ}t_d = 30$ mm. The length of the wet zone can exceed $U_{IJ}t_d$ especially for small U_{IJ} and large \dot{m} due to wicking in the longitudinal direction. The horizontal line in Fig. 4.10(a) indicates that the cooling amplitude seems to approach a constant for large \dot{m} and thus high moisture content, as the water vapor pressure approaches its maximum value in this regime.

4.3.3 Variation of surfactant concentration

Figure 4.10 shows $|\Delta T|_{\max}$ and l_{wet} for lines printed with Triton X-100 solutions of different initial concentrations $c_0 = 0$ (pure water), 1, 10 and 70 cmc as a function of the deposition rate \dot{m} . There is little difference in the values of $|\Delta T|_{\max}$ except for the lowest deposition rate. In contrast, surfactant solutions induce systematically higher values of l_{wet} compared to pure water, especially

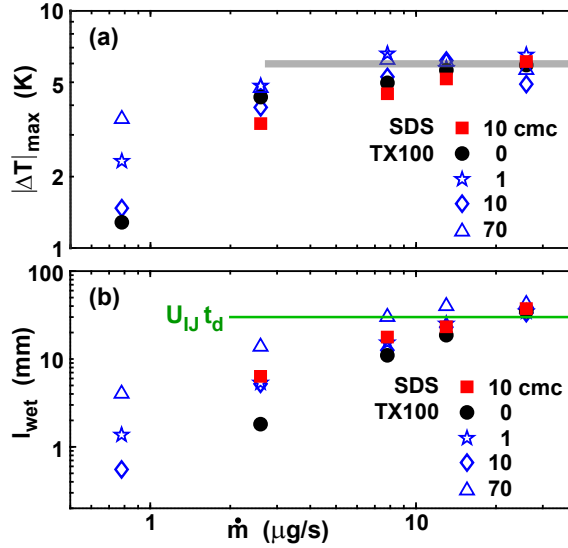


Figure 4.10: Experimental data for (a) the maximum cooling amplitude $|\Delta T|_{max}$ and (b) the length of the wet zone l_{wet} as a function of the deposition rate \dot{m} . The horizontal green line corresponds to the printing distance $U_{IJ}t_d = 30$ mm. Data for SDS ($c_0 = 10$ cmc, NF paper) are represented by filled red squares, and for pure water (NF paper) by filled black circles. Data for Triton X-100 solutions (CF paper) are represented by open asterisks for $c_0 = 1$ cmc, by open diamonds for $c_0 = 10$ cmc, and by open triangles for $c_0 = 70$ cmc. The substrate speed was kept constant at $U_{IJ} = 0.05$ mm/s.

for $c_0 = 70$ cmc. Figure 4.11 shows the variation of Δy_w , Δy_h and $|\Delta T|_{max}$ as a function of U_{IJ} for Triton X-100 solutions of different initial concentration c_0 and a constant deposition rate \dot{m} . Again there is little systematic variation in Δy_w , Δy_h and $|\Delta T|_{max}$ with surfactant concentrations. This is consistent with the findings of Hodgson and Berg for Whatman No. 40 filter paper [176]. As in Fig. 4.10(b), the exception is again the highest value of $c_0 = 70$ cmc, which induces systematically higher values of Δy_w . The dashed line in Fig. 4.11 represents a powerlaw relation $\Delta y_w \sim U_{IJ}^{0.8}$, which is a good approximation to the data. The exponent of 0.8 is close to the value of 0.75 in Fig. 4.7 (a).

4.3.4 Effect of paper type

From our experiments, we find the differences in the behavior of the two studied paper types to be minimal. Figure 4.2 indicates that the maximum holding capacity of both paper types are very close. Figure 4.7(a) illustrates that the widths of the wet zones in both paper types are within 10% for the same printing parameters and the same surfactant solution composition.

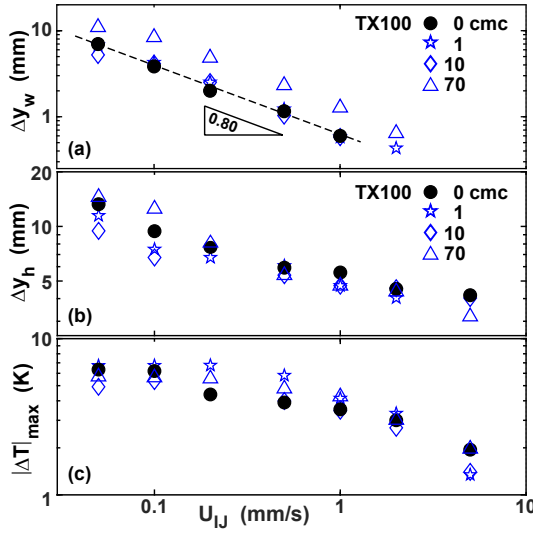


Figure 4.11: Experimental data for (a) the FWHM of the wet zone Δy_w at a location 2 cm behind the impingement point, (b) Δy_h and (c) the maximum cooling amplitude $|\Delta T|_{max}$ as a function of U_{1J} for Triton X-100 solutions with $c_0 = 0$ (pure water on NF paper, filled circles), 1 cmc (open asterisks), 10 cmc (open diamonds) and 70 cmc (open triangles) on CF paper. The deposition rate and the printed distance were kept constant at $\dot{m} = 26 \mu\text{g/s}$ and $U_{1J}t_d = 4 \text{ cm}$, respectively.

4.4 Theoretical model

The description of the transport of moisture and heat is based on the model and notation introduced in Ref. [145]. This model has been extended to account for the presence of a surface-active solute as well as for the exchange of liquid between the pore space and the interior of the paper fibers. Detailed description of the model and the development of the equations governing the transport mechanisms are presented in [145, 212]. The governing equations (to be introduced in the forthcoming subsections) are solved numerically using the finite-element software Comsol Multiphysics 5.6. A droplet radius of $18 \mu\text{m}$ is assumed in the simulations, i.e. a deposition frequency $f = 1000 \text{ Hz}$ corresponds to a mass deposition rate of $\dot{m} = 24.4 \mu\text{g/s}$. For the deposition frequencies $f \leq 1000 \text{ Hz}$ studied, the width of the temperature distribution is always larger than that of the moisture distribution. A typical maximum temperature change $|\Delta T|_{max}$ due to evaporative cooling is in the range of several Kelvin.

In the forthcoming sub-sections, the key equations and parameters are introduced which are used in the discussion section.

4.4.1 Modified Darcy velocity

The key quantity in the moisture transport equation is the Darcy velocity $\vec{v}_w = -\frac{K_w}{\mu} \nabla p_w$, which is proportional to the permeability K_w and the gradient in capillary pressure p_w of the pore space. The latter depends not only on the moisture content, but also on the temperature T and the surfactant concentration c in the aqueous phase (i.e. the mass of solute per unit volume of liquid phase, with units kg/m^3). Thus, we can write

$$\vec{v}_w = -\frac{K_w}{\mu} \left(\frac{\partial p_w}{\partial \Theta_w} \nabla \Theta_w + \frac{\partial p_w}{\partial c} \nabla c + \frac{\partial p_w}{\partial T} \nabla T \right). \quad (4.3)$$

Here, Θ_w is the pore moisture content per area of paper with units of kg/m^2 . The third term on the right represents thermocapillary pumping [213] of a meniscus by temperature non-uniformities. The second term on the right is its solutocapillary analog and couples the equations for moisture and solute transport. We shall neglect the third term, because for concentrated surfactant solutions p_w is a strong function of c , but only a very weak function of T . For p_w and K_w we adopt the Van Genuchten relations [75, 127]. The value of the maximum holding capacity of the pore space is assumed to be $\Theta_{w,max} = 58 \text{ g}/\text{m}^2$. We assume that the permeability K_w is unaffected by the presence of the surfactant.

4.4.2 Dual-porosity description of pore-fiber exchange

Paper is a porous material made up of fibers that are themselves permeable. Upon imbibition, a fraction of the water being transported along the pores is lost into the fibers, where its mobility is greatly reduced. Therefore, we adapted models introduced by Barenblatt *et al.*, Bandyopadhyay *et al.* and Zapata *et al.* to our case of moisture transport in paper [9–11]. We assume that the absolute magnitude of the capillary pressure in the fibers p_f is higher owing to the smaller effective pore size

$$p_f = a_f p_g(c_f) \left(\left(\frac{\Theta_f}{\Theta_{f,max}} \right)^{-1/m_g} - 1 \right)^{(1/n_g)}. \quad (4.4)$$

Here, the maximum moisture holding capacity of the fibers is set to $\Theta_{f,max} \equiv b_f \Theta_{w,max}$ and the dimensionless parameters were chosen to be $a_f = 1.5$ and $b_f = 1$. For simplicity we assume that the moisture content Θ_f inside the fibers is immobile [11]. Consequently, the dynamic equation, integrated along the

thickness direction of the paper substrate [145], for the moisture content in the fibers Θ_f

$$\frac{\partial \Theta_f}{\partial t} = s_{pf} - j_{ev,f} \quad (4.5)$$

contains only source and sink terms, but no transport terms. Evaporation-induced losses are described by the flux term $j_{ev,f}$. Following Ref. [9], we assume the pore-fiber moisture exchange rate to be governed by the difference in capillary pressure

$$s_{pf} = \frac{K_{pf}}{\mu} [p_w(\Theta_w) - p_f(\Theta_f)] . \quad (4.6)$$

The coefficient K_{pf} (typical value $1 \cdot 10^{-8} \text{ kg/m}^2$) determines the time constant of the exchange process. In an equilibrium configuration, characterized by $s_{pf} = 0$, the pore-fiber distribution is determined by the equality of the capillary pressures, which biases the system towards higher saturation values in the fibers than in the pores. Correspondingly, the Richards equation for the time evolution of the pore moisture content, integrated along the thickness direction of the paper substrate [145], now also contains a corresponding extra flux term

$$\begin{aligned} \frac{\partial \Theta_w}{\partial t} + U_{IJ} \frac{\partial \Theta_w}{\partial x} - \frac{\rho_w}{\mu} \nabla_{2D} (t_p K_w \nabla_{2D} p_w) = \\ j_{IJ} - j_{ev,w} - s_{pf} . \end{aligned} \quad (4.7)$$

Here, t_p is the thickness of the paper substrate, j_{IJ} is the time-averaged mass flux representing the inkjet droplet deposition, $j_{ev,w}$ is the mass flux corresponding to solvent evaporation from the pore space and $\nabla_{2D} \equiv \left(\frac{\partial}{\partial x}, \frac{\partial}{\partial y} \right)$. The total evaporative flux j_{ev}

$$j_{ev} \equiv j_{ev,w} + j_{ev,f} = k_\infty (\rho_v - \rho_{amb}) \quad (4.8)$$

is split between pores and fibers according to the ratio of the local moisture contents

$$j_{ev,w} = j_{ev} \frac{\Theta_w}{\Theta_w + \Theta_f} \quad \text{and} \quad j_{ev,f} = j_{ev} \frac{\Theta_f}{\Theta_w + \Theta_f} . \quad (4.9)$$

The heat transfer is developed in the same fashion as discussed in the previous chapter.

4.4.3 Solute transport in unsaturated porous media

Starting from 3-D transport equations for solute transport, performing vertical integration and introducing substrate motion, the 3-D equations can be

transformed into thickness averaged 2-D version leading to

$$\begin{aligned} \frac{\partial}{\partial t} (c\Theta_w) + U_{IJ} \frac{\partial}{\partial x} (c\Theta_w) + \rho_w \nabla_{2D} \cdot (t_p c \vec{\mathbf{v}}_w) - j_{IJ} c_0 = \\ = \nabla_{2D} \cdot \left[\Theta_w \underline{D}_{2D} \cdot \nabla_{2D} c \right] - e_{pf} - S_{ad} \rho_w \Theta_s , \end{aligned} \quad (4.10)$$

$$\frac{\partial}{\partial t} (c_f \Theta_f) + U_{IJ} \frac{\partial}{\partial x} (c_f \Theta_f) = e_{pf} , \quad (4.11)$$

$$\frac{\partial C_{ad}}{\partial t} + U_{IJ} \frac{\partial C_{ad}}{\partial x} = S_{ad} . \quad (4.12)$$

The pore-fiber exchange term e_{pf} is the 2D equivalent of the expressions in [212]. i.e. S_{pf} is replaced with s_{pf} . The right hand side of Eq. (4.12)

$$S_{ad} \equiv k_{ad} c \left[1 - \frac{C_{ad}}{C_\infty} \right] - k_{de} c_{cmc} \frac{C_{ad}}{C_\infty} \quad (4.13)$$

corresponds to a Langmuir adsorption isotherm [214] with adsorption and desorption rate constants k_{ad} and k_{de} . The adsorption process described by Eq. (4.13) is completely reversible, i.e. flushing with pure water will eventually desorb the surfactant completely. We assumed a sorption capacity $C_\infty = 0.5$ g/kg, which is a typical value for surfactants on paper, and a ratio $k_{ad}/k_{de} = 10$. For a thorough treatment leading to the 2-D system of equations from the 3-D equations and for an in-depth description of the governing equations, the reader is directed to [212].

4.4.4 Initial and boundary conditions

A detailed description of initial and boundary conditions are presented in [212].

4.5 Discussion

In the following subsections we will systematically investigate the influence of key parameters such as the deposition frequency f , the substrate speed U_{IJ} , the initial surfactant concentration c_0 as well as the effect of surfactant adsorption with the goal of comparing the numerical results with the experimental results. Furthermore, we discuss the phenomena of intensity overshoot and surfactant precipitation.

4.5.1 Variation of the droplet deposition frequency

In this section we focus on the effect of the droplet deposition frequency, while keeping the substrate speed and the surfactant concentration constant

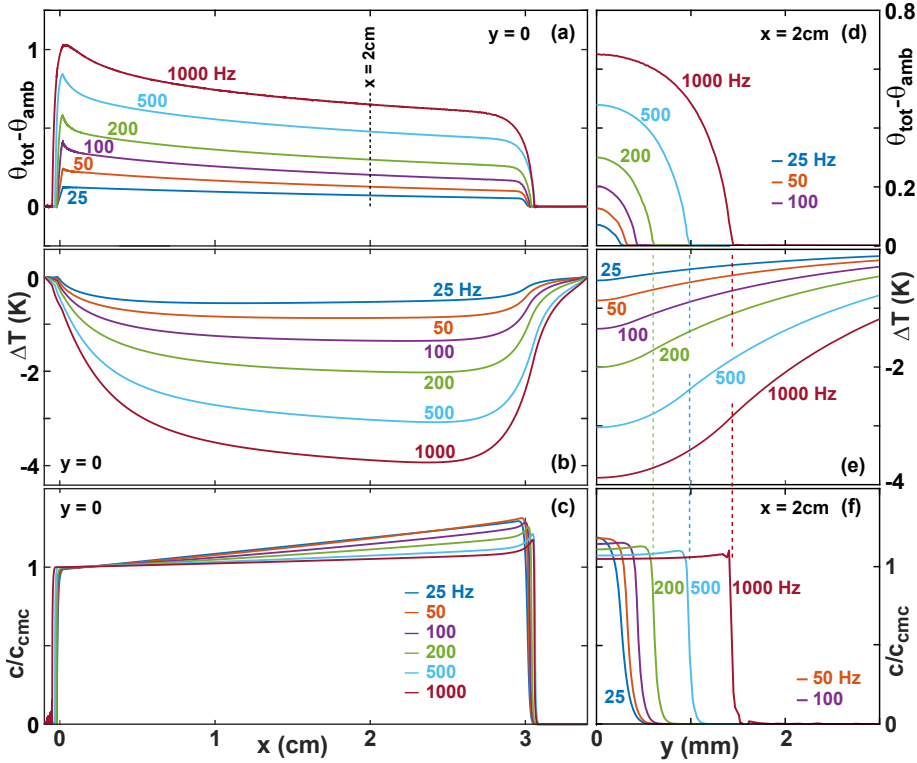


Figure 4.12: (a-c) Longitudinal cross-sections of (a) the total moisture content $\theta_{tot}(x, y = 0) - \theta_{amb}$, (b) the temperature distribution $\Delta T(x, y = 0)$ and (c) the surfactant concentration in the pores $c(x, y = 0)$ for different values of f . (d-f) Transverse cross-sections of (d) $\theta_{tot}(x = 2 \text{ cm}, y) - \theta_{amb}$, (e) $\Delta T(x = 2 \text{ cm}, y)$ and (f) $c(x = 2 \text{ cm}, y)$ at $x = 2$ cm from the impinging point for different values of f . All simulations were performed with $U_{IJ} = 0.2 \text{ mm/s}$, $c_0 = 1 \text{ cmc}$ and a printed length $U_{IJ}t_d = 3 \text{ cm}$.

at values of $U_{IJ} = 0.2 \text{ mm/s}$ and $c_0 = 1 \text{ cmc}$. We consider a printed line length of $\Delta x \equiv U_{IJ}t_d = 3 \text{ cm}$ and thus a deposition time $t_d = \Delta x/U_{IJ} = 150 \text{ s}$. We assume that no surfactant adsorption occurs, $S_{ad} = 0$.

In Fig. 4.12(a) and (d) we show longitudinal and transverse profiles of the total moisture content $\theta_{tot} - \theta_{amb}$ along the centerline $y = 0$ and at a fixed distance from the deposition point $x = 2 \text{ cm}$. It is evident that the maximum moisture content and width of the printed lines both grow with increasing frequency f . Figure 4.12(b) and 4.12(e) show the temperature decrease ΔT along the centerline $y = 0$ and in the y -direction at $x = 2 \text{ cm}$, respectively. Higher deposition frequencies induce a higher maximum temperature amplitude $|\Delta T|_{max}$ due to the larger quantity of water that can evaporate. Along the

centerline, the temperature minima are located near the end of the printed line, i.e. near the point $x = U_{IJ}t_d = 3$ cm for high frequencies. Regarding the transverse profiles in Fig. 4.12(d,e) we note that the maximum extensions of the wet zones coincide with the location of inflection points in the temperature distributions, as indicated by the vertical dashed lines. In other words, the width of the wet zone can also be inferred from thermography data alone. Overall it is seen that the simulation results qualitatively resemble the data presented in fig. 4.9. The surfactant concentration in the pores is plotted in Fig. 4.12(c,f) along the centerline and in the transverse direction at $x = 2$ cm, respectively. Far away from the impingement point the surfactant concentration exceeds $c_0 = 1$ cmc, because some of the water has evaporated, whereas the surfactant is not volatile. Since relatively more water evaporates for lower deposition rates, the increase in c is more pronounced for lower frequencies. In the transverse direction and in the absence of adsorption, the surfactant distribution in Fig. 4.12(f) is rather uniform until the perimeter of the wet zone, at which point it goes to zero rather abruptly. A detailed description about the origins of such abrupt transitions are presented in [212].

4.5.2 Variation of the substrate speed

In this subsection we study the effect of the substrate speed U_{IJ} for constant values of the deposition frequency $f = 1000$ Hz, the surfactant concentration $c_0 = 1$ cmc and the printed line length $\Delta x = U_{IJ}t_d = 3$ cm, which corresponds to varying deposition times of $t_d = \Delta x/U_{IJ}$. We assume that no surfactant ad-/absorption occurs, $S_{ad} = 0$.

For increasing substrate speeds, the moisture distribution tends to be lower in amplitude but progressively more uniform, because both evaporation and lateral wicking have less time to cause removal or redistribution of liquid away from the centerline. Regarding the temperature profiles, for high speeds, a localized increase in temperature occurs in the vicinity of the impingement point at $x = 0$ (similar to the results discussed in previous chapter), which is due to the sorptive heating term proportional to U_{IJ} . The minima of the temperature distribution are located near $x = U_{IJ}t_d = 3$ cm for all values of U_{IJ} .

The surfactant concentration increases towards larger values of x most prominently for the slower speeds, because evaporation has more time to remove part of the water. For high speeds, the level of c near the injection point $x = 0$ falls below c_0 . This is because less water is deposited per unit length for higher speeds and the initially present moisture content θ_{amb} serves to slightly dilute c to a value below c_0 . The transverse cross-sections of the moisture distributions

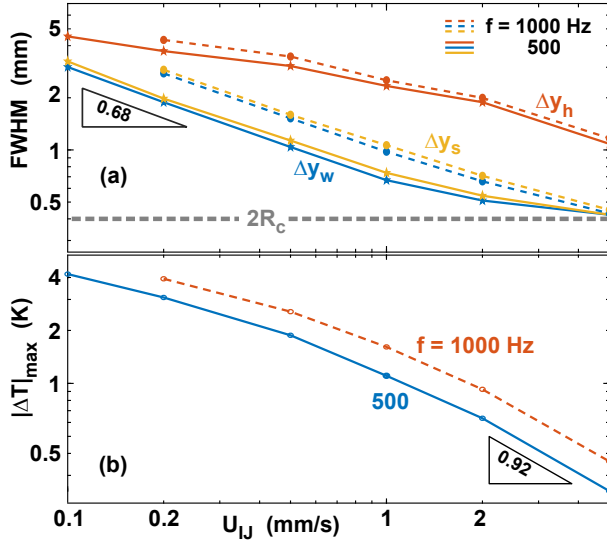


Figure 4.13: (a) FWHM of the total moisture-, temperature- and surfactant concentration distributions Δy_w , Δy_h and Δy_s at $x = 2$ cm as a function of the substrate speed U_{IJ} for $f = 1000$ Hz. (b) Maximum cooling amplitude $|\Delta T|_{\max}$ as a function of U_{IJ} for two values of the droplet frequency $f = 500$ and 1000 Hz. In both (a,b) we assumed a constant printed length $U_{IJ}t_d = 3$ cm, $c_0 = 1$ cmc, and that no surfactant adsorption occurs, $S_{ad} = 0$.

and surfactant concentrations at $x = 2$ cm resemble those in Fig. 4.12(d,f). Especially for the slowest speed considered, the surfactant concentration slightly increases towards the perimeter of the wet zone. The lower moisture content near the perimeter leads to a larger relative water loss due to evaporation and thus a higher concentration.

In the absence of solid adsorption, the values of Δy_w and Δy_s are again quite close. In the limit of high speeds, Δy_w , Δy_s and Δy_h all approach the limit $2R_c$, because less time is available for transverse spreading. Since the thermal diffusivity is a weak function, but the permeability and thus the effective moisture diffusivity a strong function of θ_{tot} , Δy_h exceeds Δy_w in the range of speeds shown. In the range where Δy_w is much larger than $2R_c$, a powerlaw relation $\Delta y_w \sim U_{IJ}^{0.68}$ is a reasonable approximation to the numerical data. The exponent 0.68 is close to the experimental value of 0.75 observed in Fig. 4.7(a). Moreover, the magnitude of Δy_w closely matches the experimental data in Fig. 4.7(a)

Figure 4.13(b) presents the maximum cooling amplitude $|\Delta T|_{\max}$ as functions of the substrate speed. $|\Delta T|_{\max}$ increases with decreasing speed and increasing f , because more water is then deposited per unit length. If a pow-

erlaw relation $|\Delta T|_{\max} \sim U_{IJ}^\epsilon$ were fitted through the datapoints for the 2 highest values of U_{IJ} , the exponent would have a value of -0.92. This is close to the experimental value of -0.82 in Fig. 4.7(c). Moreover, the magnitude of $|\Delta T|_{\max}$ agrees well with the data in Fig. 4.7(c).

4.5.3 Variation of the surfactant concentration

In this subsection, we study the effect of variations in the initial surfactant concentration c_0 for constant values of $U_{IJ} = 5 \text{ mm/s}$ and $f = 500 \text{ Hz}$. We assume that no surfactant ad-/absorption occurs, $S_{ad} = 0$.

For high speeds that are simulated, it is the case that the transverse moisture-distributions collapse for increasing surfactant concentration, which might appear to indicate that the surfactant concentration level c_0 has no effect on the dynamics of the moisture and thus surfactant redistribution. The actual reason is that due to the high speed, the moisture and surfactant distributions have not had a chance, yet, to spread beyond the initial value of R_c . However, since the capillary pressure ceases to depend on c for concentrations exceeding the cmc, we do not expect qualitative differences as a function of c_0 even at lower speeds for $c_0 > 1 \text{ cmc}$, as in the absence of adsorption the surfactant is not depleted.

4.5.4 Effect of surfactant adsorption

In this subsection, we study the effect of surfactant adsorption $S_{ad} \neq 0$. Figure 4.14(a) compares the centerline profiles of the surfactant concentration $c(x, y = 0, t_d)$ for two 2D simulations with and without surfactant adsorption. While without adsorption the concentration slowly increases away from the deposition point due to evaporation, it quickly decreases to a level of about 0.3 cmc for an absorption capacity of $C_\infty = 0.5 \text{ g/kg}$ and rate constants $k_{ad} = 1 \cdot 10^{-4} \text{ m}^3/\text{kg s} = 10k_{de}$. Similarly, the transverse profile $c(x = 2 \text{ cm}, y, t_d)$ in Fig. 4.14(b) is rather uniform at a concentration close to $c_0 = 1 \text{ cmc}$ and drops rather abruptly to zero at the perimeter of the wet zone in the absence of adsorption. In the presence of adsorption, $c(x = 2 \text{ cm}, y, t_d)$ approaches zero in a smooth and continuous fashion at the boundary of the wet zone.

We have also performed one-dimensional simulations of the lateral imbibition of surfactant solutions in paper substrates. For this case we assumed a sorption capacity $C_\infty = 0.5 \text{ g/kg}$ and rate constants of $k_{ad} = 1 \cdot 10^{-4} \text{ m}^3/(\text{kg s}) = 10k_{de}$. In spirit, these simulations describe the broadening dynamics of a line printed at high speed, for which longitudinal gradients of all quantities are negligible, sufficiently far from the deposition point. The dashed lines in Fig. 4.15(a,b)

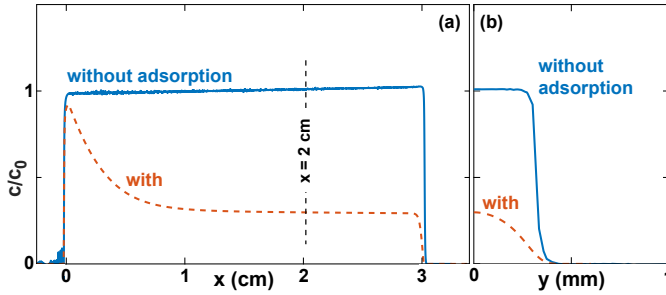


Figure 4.14: (a) Longitudinal ($y = 0$) and (b) transverse ($x = 2$ cm) cross-sections of 2D numerical simulations of the surfactant concentration in the pores c for $U_{IJ} = 1$ mm/s, $f = 1000$ Hz, $c_0 = 1$ cmc and a printed length $U_{IJ}t_d = 3$ cm. Solid and dashed lines correspond to simulations without and with adsorption, respectively.

represent the ICs of the total moisture distribution $\theta_{tot}(x, t = 0) - \theta_{amb}$ and the surfactant concentration $c(x, t = 0)$ for four different values of $c_0 = 0, 1, 5$ and 10 cmc. The solid lines in Fig. 4.15 correspond to the solutions at $t = 300$ s. Within that time, the wet zone spread by approximately 2 mm for $c_0 = 1$ and 5 cmc, but by only about 1.6 mm for $c_0 = 0$ and 10 cmc.

Figure 4.15(b) shows that the surfactant essentially does not spread beyond the initially wet region for $c_0 = 1$ cmc, whereas it spreads further for $c_0 = 10$ cmc. However, the surfactant front lags significantly behind the moisture front, even for $c_0 = 10$ cmc. This behavior is qualitatively equivalent with the one seen in Fig. 4.1. The IC for the adsorbed concentration was $C_{ad}(y, t = 0) = 0$. Figure 4.15(c) shows that for $c_0 = 1$ cmc, C_{ad} stays far below C_∞ , whereas for $c_0 = 10$ cmc, it reaches the maximum adsorption capacity and drops rather abruptly to zero at $y \approx 1.9$ mm.

The total moisture content in Fig. 4.15(a) exhibits local maxima and minima close to the surfactant concentration front at $t = 300$ s, which are most pronounced for $c_0 = 1$ and 5 cmc. These are caused by capillary pressure gradients induced by the surfactant concentration gradients. They have not been observed in our previous simulations without adsorption, because there the surfactant front coincided with the moisture front. Analogous local maxima and minima in moisture content near the surfactant front have been observed in [169, 171, 215–217]. Since a higher moisture content gives rise to an increased light transmission, these curves are consistent with Fig. 4.1 and the inset in Fig. 4.15(a), where a dark zone is visible at the centerline. Filenkova *et al.* observed a very similar solvent content distribution with a depression along the centerline of a printed line of an aqueous solution of a non-ionic surfactant - see Fig. 4(a) in Ref. [33].

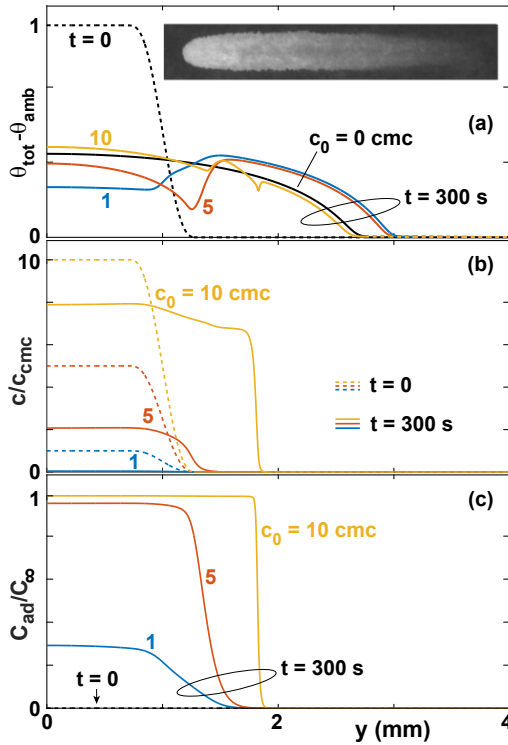


Figure 4.15: 1D numerical simulations of (a) the total moisture distribution $\theta_{\text{tot}} - \theta_{\text{amb}}$, (b) the surfactant concentration c and (c) the adsorbed concentration C_{ad} for four different values of $c_0 = 0, 1, 5$ and 10 cmc. Solid and dashed lines correspond to solutions at $t = 0$ and $t = 300$ s, respectively. Inset: optical transmission image of a printed line of a Triton X-100 solution of initial concentration $c_0 = 1$ cmc ($U_{\text{IJ}} = 0.1$ mm/s, $\dot{m} = 26$ $\mu\text{g/s}$).

4.5.5 Intensity overshoot

SDS is an ionic surfactant that stabilizes foam lamellae [218], whereas Triton X-100 as a non-ionic surfactant does not. The geometry of an unsaturated moisture distribution where water in the pores is sucked into the surrounding fibers resembles the geometry of the so-called *thin film balance* that is used to stabilize and study foam layers by means of a porous ring-shaped support [219, 220]. During the transition of liquid from the pores to the fibers, the area of the air-water interface is likely increasing, which implies that surface elasticity effects could play a role.

The process of imbibition of a surfactant solution into a porous medium under unsaturated conditions also shares common aspects with the flow of foams in porous media. Aranda *et al.* have studied the injection of foam into an

unsaturated bulk porous medium partially filled with a surfactant solution [221]. They observed the formation of a ‘weak’ and a ‘strong’ foam zone separated by a sharp boundary. Foam flow in porous media has been studied primarily for systems with essentially impermeable pore walls such as sand columns and rocks. Even then it can take a long time to approach a steady state [222–225].

We visualized the imbibition of surfactant solutions into paper using optical reflection microscopy. In contrast to the case of pure water, we observed a large number of small, abrupt changes in grayscale on a lengthscale comparable to the size of the large pores. We interpret them as the disintegration of menisci and lamellae. These events were more numerous and longer lasting for SDS than for Triton X-100, which correlates with the larger intensity overshoot for SDS than for Triton X-100.

When liquid enters a porous medium, the pores are filled first, due to their higher permeability. Due to the higher absolute magnitude of the capillary pressure of liquid inside the fibers, liquid is subsequently transferred into the fibers [210]. Since the spatial dimensions of the pores are comparable to the wavelength of light λ and the dominant lengthscales inside the fibers are much smaller than λ , the presence of air-filled pores is the dominant scattering mechanism that determines the light transmission intensity. When air is replaced by water, the scattering efficiency decreases and the transmitted intensity first increases and later decreases due to pore-fiber redistribution. We believe the origin of the observed intensity overshoot to be the surfactant-induced delay of the pore-fiber redistribution effect.

4.5.6 Surfactant precipitation

Hodgson and Berg [176] reported that the imbibition rate of an SDS solution with $c_0 \approx 0.6$ cmc into Whatman No. 40 filter paper is less than 70% of that of pure water, whereas the imbibition rate of a Triton X-100 solution with $c_0 \approx 0.6$ cmc is only 5% slower compared to pure water. The imbibition rate thus does not correlate with c_0 /cmc, i.e. the surface activity. Rather, the key property is the adsorption capacity. The value of C_∞ of Triton X-100 is approximately three times higher than that of SDS, which is in part related to its higher MW. Moreover, the cmc of Triton X-100 in molar units is substantially lower than that of SDS. Consequently, compared to SDS a 0.6 cmc solution of Triton X-100 contains substantially fewer molecules, which in addition have a higher tendency to get adsorbed.

In our experiments, however, we often do not observe a significant difference in the imbibition rates between SDS and Triton X-100. The two paper types we studied are both loaded with CaCl_2 in order to accelerate and improve ink

fixation [226–229]. It is well known that Ca^{2+} ions also induce the precipitation of anionic surfactants [230–234]. Paria *et al.* measured a strong increase of C_∞ of SDBS on cellulose upon addition of Ca^{2+} ions [198]. We therefore conclude that in our experiments the presence of Ca^{2+} ions induces precipitation of the anionic surfactant SDS, which in turn substantially increases its tendency to get adsorbed. Interesting visualization of the effect of precipitation can be better observed with dyes (to be discussed in the next chapter)

4.6 Summary and conclusions

We have conducted systematic experiments regarding the effect of surfactants on the inkjet deposition of long lines in paper substrates. We have used both anionic and non-ionic surfactants and varied the substrate speed, deposition frequency and surfactant concentration.

Moreover we have constructed a corresponding numerical model that accounts for the presence of permeable fibers, solvent evaporation, surfactant transport and adsorption as well as evaporative cooling. The presence of permeable fibers renders the moisture distributions more abrupt and reduces the imbibition rate compared to a porous medium comprising impermeable fibers of equal holding capacity.

We found that the imbibition dynamics of surfactant solutions in the two paper types studied were virtually identical. However, both paper types we used were optimized by the manufacturer for inkjet printing applications using water-based inks. Preliminary investigations into a larger range of paper types hint towards a much stronger material dependence, especially for more hydrophobic paper types. This is the subject of ongoing investigations.

For the case of deposition of pure water, the moisture distribution tends to monotonically decrease away from the impingement point. In contrast, the presence of surfactants can induce non-monotonic moisture distributions. This occurs especially when the surfactant front lags behind the moisture front as a consequence of adsorption, because surfactant concentration gradients induce capillary pressure gradients. At low concentrations, the surfactant remains essentially localized to the deposition area due to adsorption. Only above a threshold concentration that depends on the adsorption capacity of the paper and is of order of 1-2 cmc for SDS and Triton X-100 can the surfactant spread beyond the deposition area.

Acknowledgements

This work is part of the research programme ‘*The role of surfactants in spreading, imbibition and sorption of water-based printing inks*’ with project number 14666, which is (partly) financed by the Netherlands Organisation for Scientific Research (NWO). The author thanks Nicolae Tomozeiu, Herman Wijshoff and Louis Saes of Canon Production Printing for the fruitful cooperation.

Author contribution statement

The results discussed in this chapter are from the publication Ref [212]. The author of this thesis developed the experimental setup and the measurement protocols. He conducted all the experiments and analyzed the experimental data. The theoretical model was developed by Gianmarco Venditti who also performed all the numerical simulations and analyzed the numerical data. The manuscript was written by the author and Gianmarco Venditti.

Table 4.1: List of symbols and parameters.

Symbol	Name	Value	Units
a_f	Fiber pressure scaling factor	1.5	-
b_f	Water fraction fibers	0.5	-
b_p	Water fraction pores	0.5	-
c	Surfactant concentration (pores)	-	kg/m ³
C_{ad}	Adsorbed surfactant concentration	-	g/kg
c_f	Surfactant concentration (fibers)	-	kg/m ³
$c_{p,av}$	Average specific heat capacity	-	J/(kg K)
$c_{p,w}$	Specific heat capacity of water	4180	J/(kg K)
c_{cmc}	Critical micelle concentration	150	mg/l
C_∞	Sorption capacity of paper	0.5	g/kg
e_{pf}	2D pore-fiber surfactant flux	-	kg ² /(m ⁵ s)
f	Deposition frequency	-	Hz
j_{ev}	Total evaporative mass flux	-	kg/m ² s
j_{IJ}	Mass influx of deposited droplets	-	kg/m ² s
k_{ad}	Adsorption rate coefficient	10 ⁻⁴	m ³ /(kg s)
k_{av}	Average thermal conductivity	-	W/mK
k_c	Van Genuchten parameter	0.3	-
k_{de}	Desorption rate coefficient	0.1 · k_{ad}	m ³ /(kg s)
K_{pf}	Pore-fiber exchange coefficient	2.6 · 10 ⁻⁹	kg/m ²
K_s	Absolute permeability	1.2 · 10 ⁻¹²	m ²
K_w	Permeability	-	m ²
k_∞	Mass transfer coefficient	2.8 · 10 ⁻³	m/s
l_{wet}	Length of the wet zone	-	m
\dot{m}	Mass deposition rate	-	g/s
m_g	Van Genuchten exponent	1-1/ n_g	-
MW	Molecular weight	-	g/mol
p_g	Pressure scaling parameter	-	Pa
p_{sat}	Saturation vapor pressure	-	Pa
p_f	Capillary pressure (fibers)	-	Pa
p_w	Capillary pressure (pores)	-	Pa
q_{2D}	2D heat flux	-	W/m ²
S_{ad}	Wall adsorption flux	-	1/s
s_{pf}	2D pore-fiber moisture flux	-	kg/(m ² s)
S_{pf}	3D pore-fiber moisture flux	-	kg/(m ³ s)
T	Temperature of porous medium	-	K
T_{IJ}	Droplet temperature	297.65	K
\vec{v}_w	Darcy velocity	-	m/s
α	Contact angle	-	deg.
β	Surfactant affinity coefficient	1	-
γ_{ls}	Liquid-solid interfacial tension	-	N/m
γ_{lv}	Liquid-vapor interfacial tension	-	N/m
γ_{sv}	Solid-vapor interfacial tension	-	N/m
Θ_f	Areal density moisture in fibres	-	g/m ²
$\Theta_{f,3D}$	Volumetric fiber moisture content	-	g/m ³
$\Theta_{f,amb}$	Ambient fiber moisture content	-	g/m ²
$\Theta_{f,max}$	Maximum holding capacity (fibers)	58	g/m ²
θ_{max}	Non-dim. max. moisture content	-	kg/kg
Θ_s	Area mass density of dry paper	77	g/m ²
$\Theta_{s,3D}$	Mass density of dry paper	-	g/m ³
Θ_{tot}	Total areal moisture density	-	g/m ²
Θ_w	Areal density moisture in pores	-	g/m ²
$\Theta_{w,3D}$	Volumetric pore moisture content	-	g/m ³
$\Theta_{w,amb}$	Ambient pore moisture content	-	g/m ²
$\Theta_{w,max}$	Maximum holding capacity (pores)	58	g/m ²
ζ_c	Surfactant scaling factor	0.0047	l/mg

Chapter 5

Chromatographic effects in inkjet printing

We have studied the chromatographic separation of solvents and dyes after deposition of a dye solution on a paper substrate. Due to their larger molecular size, dyes exhibit a stronger interaction with the paper constituents. Consequently, the imbibition process of the dye is delayed compared to that of the solvent. This has impact on the achievable resolution and color homogeneity in inkjet printing. We present experiments and a comprehensive numerical model to illustrate and quantify these effects. The model accounts for the solvent evaporation, heat transfer, multicomponent unsaturated flow, dye adsorption as well as the presence of permeable fibers in the paper substrate.

5.1 Introduction

Chromatography is an analytical technique for the separation of a multicomponent liquid or gaseous sample during flow through a polymeric or porous matrix based on the different molecular interactions of the individual components with the host matrix [235]. The individual components move at smaller average speeds than the solvent and accumulate into bands or peaks. The shape of the peaks and the speed of propagation contains information on the specific interactions. In thin-layer chromatography, paper substrates are frequently used [236, 237]. In corresponding paper-based microfluidic devices, the flow mechanism is usually based on spontaneous capillary imbibition [238, 239].

Printing inks are typically multicomponent solutions of colorants, surfactants, humectants and numerous other additives in aqueous or organic solvents [12]. Upon contact with paper, capillary imbibition causes flow of the solution. While progressive absorption of the solvent into the paper is usually desirable, it is generally undesirable if the ink colorants are transported significant distances from the ink deposition zone, as this diminishes the achievable resolution of the printing process. Similarly undesirable are a chromatographic separation

of dye mixtures or non-homogeneous dye concentration profiles, because these degrade the color uniformity and contribute to edge mottle.

Donigian *et al.* studied the chromatographic retention of dyes on thin coating layers as frequently used as topcoats on high-quality paper types optimized for inkjet printing [240]. They studied the effect of binder concentration for coatings containing either silica or calcium carbonate nanoparticles. Sodhi *et al.* and Filenkova *et al.* applied secondary ion mass spectroscopy (SIMS) to characterize the spatial distributions of various ink components after inkjet printing of a long line with an approximate width of $200\ \mu\text{m}$ [241, 242]. For a coated paper the line width is homogeneous, whereas for an uncoated paper, the line edges are ragged. In both cases, however, the dye front clearly lags behind the ink vehicle front.

Lamminmäki *et al.* studied the chromatographic separation of an anionic dye in thin porous layers composed of porous CaCO_3 microparticles and either anionic or cationic binders [13]. These materials are commonly used as coating top layers in photo-quality papers optimized for inkjet printing. The porous layer was oriented vertically and dipped into a horizontal reservoir filled with an aqueous solution of an anionic dye. Depending on whether the charges of the dye and the host matrix were of equal or opposite polarity, the retention of the dye molecules was either weak or very strong during the propagation of the water front up the porous layer.

The purpose of this study is to present a numerical model for the imbibition and evaporation of a dye-based model ink containing a molecularly dissolved colorant in a solvent into and from paper substrates. The presence of fibers in the paper substrate is explicitly taken into account. The dye-paper interaction is described by a Langmuir-type rate equation for adsorption and desorption. The experimental goals are to complement the numerical simulations. Experiments are performed using anionic and cationic fluorescent dyes deposited either by drop-casting or inkjet printing.

5.2 Materials and methods

The paper type we used was Mondi DNS HSI NF with a thickness $t_p = 104\ \mu\text{m}$, which contains CaCl_2 to aid the inkjet print quality. We used two different fluorescent dyes: the cationic red dye Rhodamine B (Sigma-Aldrich, product number R6626, molecular weight (MW) 479.02) and the anionic green dye Fluorescein sodium salt (FSS, Sigma-Aldrich, product number 46960, MW 376.27). Their molecular structures are shown in Fig. 5.1. Solutions of various initial concentrations c_0 were prepared with demineralized water.

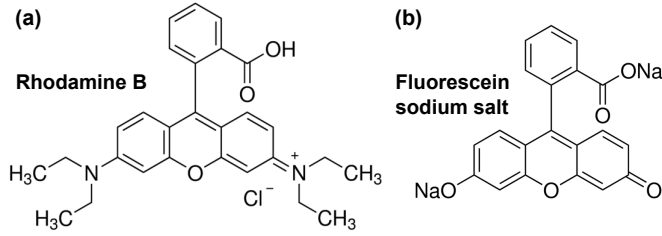


Figure 5.1: Molecular structures of (a) Rhodamine B and (b) Fluorescein sodium salt (FSS).

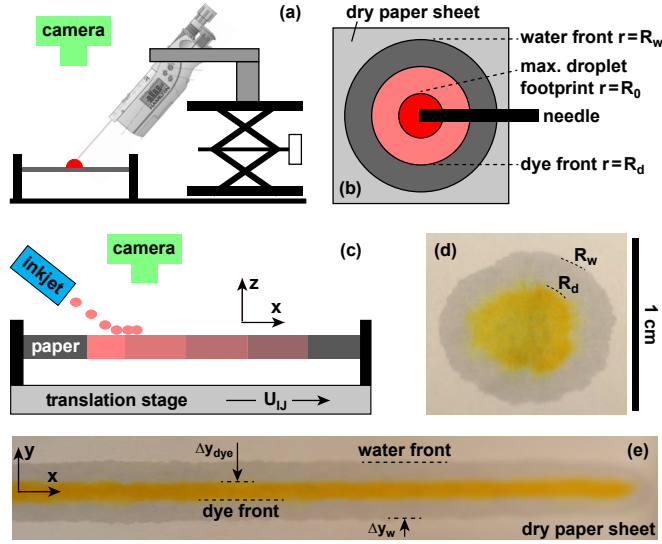


Figure 5.2: (a) Sketch of the drop casting setup. (b) Definitions of relevant positions. (c) Sketch of inkjet deposition setup (d,e) Top-view photographs after (d) drop-casting of an FSS solution ($c_0 = 0.025$ wt%) and (e) inkjet printing an FSS line ($c_0 = 0.05$ wt%, $U_{IJ} = 0.5$ mm/s). The water and dye fronts are indicated.

For our experiments we used two different deposition methods: drop casting using a digital syringe (Hamilton, product number 80065, capacity $10 \mu\text{l}$) and inkjet deposition using a droplet-on-demand printhead (Microdrop, model MDK-140-020). The corresponding experimental setups are sketched in Fig. 5.2(a,c). In both cases the paper substrates are mounted about 6 mm above a solid surface, i.e. both sides of the paper are surrounded by air rather than being in contact with a solid surface. In the inkjet setup the paper is mounted on a motorized translation stage, which allows moving the paper substrate laterally with a speed U_{IJ} ranging from 0.05 to 5 mm/s. The inkjet setup and corresponding experimental procedures are described in detail in Ref. [145]. In

the drop casting experiments, a droplet of approximate volume $5 \mu\text{l}$ was first formed at the nozzle of a syringe. Subsequently, the syringe was lowered using a labjack (Thorlabs, product number L490) until the drop made contact with the horizontal paper substrate. The syringe was maintained in this position for the entire duration of the experiment. Since it was not oriented exactly vertically, the drop footprint shape deviated from an exact circle, which explains the slightly oblong proportions of the water and dye fronts in Fig. 5.2(d).

Fig. 5.2(d,e) present typical results of the drop-casting and inkjet-deposition experiments using FSS solutions. It is clearly visible that the dye front fell behind the water front. For drop-casting experiments, we quantify this separation of the water and dye fronts by means of the retardation factor R_f defined as the ratio of the maximum propagation distances of the dye front and the water front

$$R_f \equiv \frac{\max(R_d) - \max(R_0)}{\max(R_w) - \max(R_0)}. \quad (5.1)$$

Here, R_d , R_w and R_0 are the positions of the dye front, the water front and the footprint radius of the dispensed droplet as illustrated in Fig. 5.2(c). Due to drop spreading, capillary imbibition and evaporation, these parameters are time-dependent, which motivates the use of the maximum operators.

5.3 Experimental results

5.3.1 Drop casting

We performed drop-casting experiments using FSS and Rhodamine B solutions of different initial concentration c_0 and the setup sketched in Fig. 5.2(a,b). Figure 5.3 shows the extracted retardation factor R_f as a function of c_0 . The results qualitatively resemble those obtained by Koivunen *et al.* using imbibition of tartrazine and safranin solutions from infinite reservoirs into porous layers comprised of calcium carbonate microparticles and polymeric binders [243].

5.3.2 Inkjet deposition of colorant lines

We performed inkjet deposition experiments using FSS and Rhodamine B solutions and the setup sketched in Fig. 5.2(c). We varied the substrate speed and the droplet ejection frequency, as quantified by the mass deposition rate \dot{m} . Figure 5.4(a-e) shows top-view photographs of inkjet deposited lines of an FSS solution ($c_0 = 0.025 \text{ wt}\%$) for a substrate speed $U_{IJ} = 0.2 \text{ mm/s}$ and different values of \dot{m} . Figure 5.4(f) shows the transverse widths of the wet zone Δy_w and the dye line Δy_c as functions of \dot{m} . The solid lines correspond to powerlaw

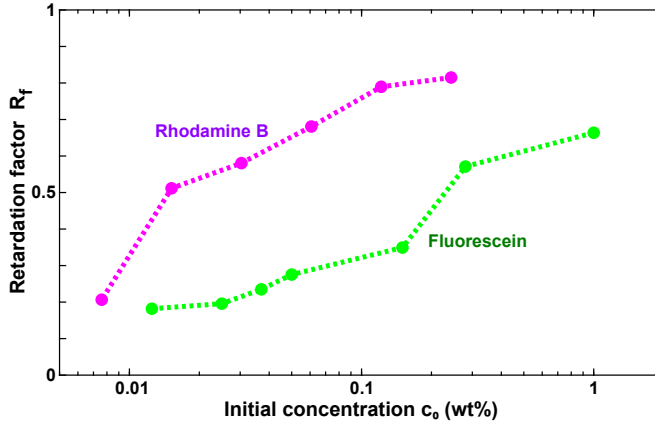


Figure 5.3: Retardation factor R_f for Rhodamine B and FSS solutions on Mondi DNS HSI NF paper as a function of initial concentration c_0 extracted from drop-casting experiments.

relations $\Delta y_w \sim \dot{m}^{0.81}$, $\Delta y_{c,FSS} \sim \dot{m}^{0.59}$ and $\Delta y_{c,RB} \sim \dot{m}^{0.81}$, respectively, which represent the experimental data very well. The gray horizontal line corresponds to the approximate deposition width Δy_0 , which is the equivalent parameter of $2R_0$ in the drop-casting experiments. We estimated $\Delta y_0 \approx 0.2$ mm from a high-speed deposition experiment at $U_{IJ} = 5$ mm/s. For the two lowest values of \dot{m} , Δy_c remains close to Δy_0 . This is due to two reasons: for lower moisture contents, the permeability of the porous medium is much smaller, such that the moisture front progresses relatively less far before evaporation is complete. Moreover, in the limit of low ink mass deposition, the quantity of the colorant per unit mass of paper eventually falls below the effective dye sorption capacity.

Figure 5.5(a-e) shows top-view photographs of inkjet deposited lines of an FSS solution ($c_0 = 0.025$ wt%) for a mass deposition rate of $\dot{m} = 27 \mu\text{g/s}$ and different values of the substrate speed U_{IJ} . Figure 5.5(f) shows Δy_w and Δy_c as functions of U_{IJ} . The solid lines correspond to powerlaw relations $\Delta y_w \sim \dot{m}^{-0.79}$ and $\Delta y_{c,FSS} \sim \dot{m}^{-0.56}$ and $\Delta y_{c,RB} \sim \dot{m}^{-0.79}$, respectively, which represent the experimental data very well. The absolute values of the powerlaw exponents are very close to the ones found in Fig. 5.4(f). This is because the mass of ink deposited per unit length of printed line scales as \dot{m}/U_{IJ} . The powerlaw exponents for Rhodamine B in both Fig. 5.4(f) and Fig. 5.5(f) match those of the solvent front, whereas the absolute magnitude of those for FSS are smaller.

The data in Fig. 5.4(f) and Fig. 5.5(f) imply that the retardation factor essentially approaches zero for small \dot{m} and large U_{IJ} values. In the limits of

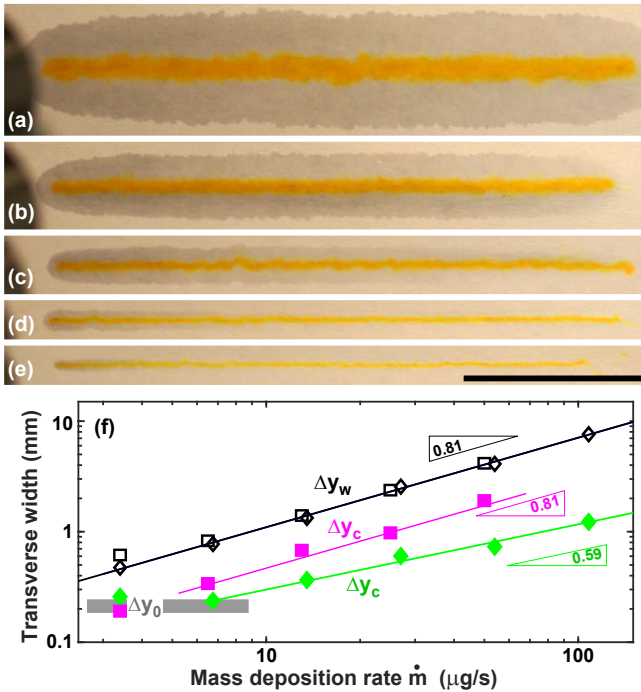


Figure 5.4: Top-view photographs after inkjet deposition of lines of an FSS solution ($c_0 = 0.025 \text{ wt}\%$) for a substrate speed of $U_{IJ} = 0.2 \text{ mm/s}$ and different mass deposition rates \dot{m} of (a) 108, (b) 54, (c) 27, (d) 13.5 and (e) $6.75 \mu\text{g/s}$ on Mondi DNS HSI NF paper. The scalebar in (e) represents 1 cm. (f) Transverse widths of the wet zone Δy_w (open symbols) and the dye line Δy_c (filled symbols) as functions of \dot{m} . Diamonds correspond to FSS ($c_0 = 0.025 \text{ wt}\%$), squares to Rhodamine B ($c_0 = 0.015 \text{ wt}\%$).

large \dot{m} or small U_{IJ} values, R_f approaches a constant value for Rhodamine B, because the powerlaw exponents of Δy_c and Δy_w are to good approximation identical. For FSS the exponents are different, which implies that R_f will eventually approach zero for large \dot{m}/U_{IJ} . Consequently, from the perspective of preventing line broadening and maximizing resolution, printing at small values of \dot{m}/U_{IJ} is preferable.

5.4 Theoretical model

Murali *et al.* and Venditti *et al.* developed a theoretical model for the *in-plane* transport of moisture, surface-active solutes and heat in thin, fibrous, moving porous media [145,212]. This model developed (in the previous two chapters) are adapted to describe the absorption and evaporation of an inkjet ink consisting

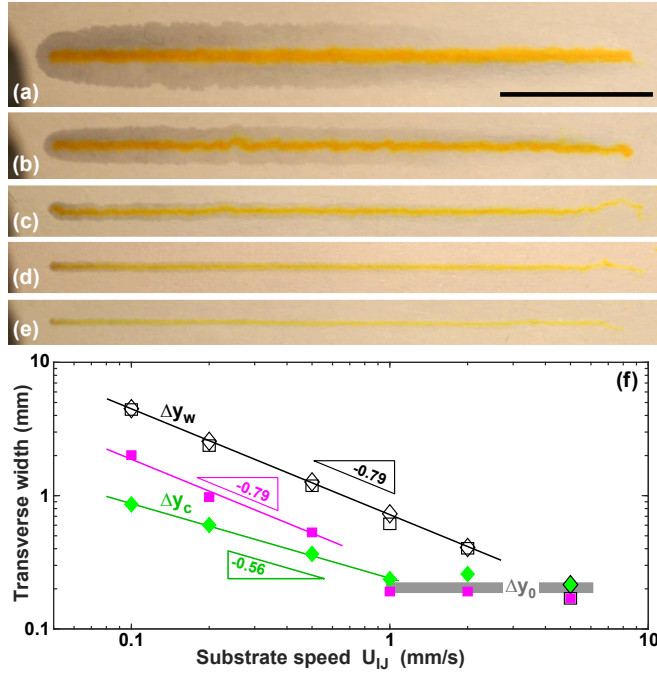


Figure 5.5: Top-view photographs after inkjet deposition of lines of an FSS solution ($c_0 = 0.025$ wt%) for $\dot{m} = 27 \mu\text{g/s}$ and different substrate speeds U_{IJ} of (a) 0.1, (b) 0.2, (c) 0.5, (d) 1 and (e) 2 mm/s on Mondi DNS HSI NF paper. The scalebar in (a) represents 1 cm. (f) Transverse widths of the wet zone Δy_w (open symbols) and the dye line Δy_c (filled symbols) as functions of U_{IJ} . Diamonds correspond to FSS ($c_0 = 0.025$ wt%), squares to Rhodamine B ($c_0 = 0.015$ wt%).

of a non-surface-active colorant that is molecularly dissolved in a solvent after deposition onto a stationary horizontal sheet of paper.

We use a Cartesian coordinate system with an x -axis parallel to the printing direction. The vertical z -axis is perpendicular to the horizontal paper sheet.

The model explicitly accounts for the presence of permeable fibers by means of a dual-porosity description. The moisture content Θ_f inside the fibers is assumed immobile [11]. Consequently, the dynamic equation for Θ_f (units kg/m^2) contains only flux terms but no transport terms. Moreover, the crucial difference between this model and the model developed for a surface active solute is that the Darcy velocity does not depend on the concentration of the solute. The time evolution of the pore moisture content Θ_w is governed by the Richards equation [126], integrated along the thickness direction of the paper

substrate [145]

$$\frac{\partial \Theta_w}{\partial t} - \frac{\rho_w}{\mu_w} \nabla_{2D} (t_p K_w \nabla_{2D} p_w) = -j_{ev,w} - s_{pf} , \quad (5.2)$$

where ρ_w and μ_w are the mass density and viscosity of the ink, t_p is the thickness of the paper, K_w is the permeability, p_w is the capillary pressure, $j_{ev,w}$ the evaporative flux from the pores to the ambient atmosphere and $\nabla_{2D} \equiv \left(\frac{\partial}{\partial x}, \frac{\partial}{\partial y} \right)$. We assume that K_w is unaffected by the presence of the colorant. Moreover, we assume that the ink viscosity increases with dye concentration according to the empirical relation

$$\mu(c) = \mu_{H_2O} \exp(c/c_1) . \quad (5.3)$$

where $c_1 = 51.44 \text{ kg/m}^3$.

The evaporation process is assumed to be diffusion-limited. The total evaporative flux j_{ev} is developed similar to the previous chapter.

The total moisture content is defined as $\Theta_{tot} \equiv \Theta_w + \Theta_f$. Its value for paper in equilibrium with ambient conditions is denoted Θ_{amb} . In the following we shall also be referring to the dimensionless total moisture content defined as $\theta_{tot} \equiv \Theta_{tot}/\Theta_s$, where $\Theta_s \approx 77 \text{ g/m}^2$ is the mass density of dry paper. The maximum water holding capacity of the paper substrate is denoted Θ_{max} . Its dimensionless variant is θ_{max} , which is assumed to have a value of 1.5 [212].

The heat transfer and solute transport equations are developed in the same fashion as in the previous chapters, for more details on the governing equations and the corresponding heat sources and fluxes, see [145]. A detailed description of the boundary and initial conditions are described in detail in [212].

5.4.1 Scales and dimensionless parameters

Concentration

The colorant concentration c of the ink is expressed in mass per unit volume of liquid (units kg/m^3). The sorption capacity C_∞ is usually given in mass of dye per unit mass of porous material (units mg/g). Consequently, a natural choice for a non-dimensionalized concentration is

$$\chi \equiv \frac{c \Theta_{tot}/\Theta_s}{\rho_w C_\infty} , \quad (5.4)$$

where ρ_w is the mass density.

Length- and timescales

The relevant geometric lateral lengthscale is the halfwidth of the line y_0 , which we assume to be on order of 1 mm. Moreover, several timescales can be devised:

an evaporation timescale given by the quantity of water present initially divided by the evaporative flux $\tau_{evap} \equiv \theta_{tot}(y=0, t=0)/(k_\infty[\rho_s(t=0) - \rho_{amb}])$, an adsorption timescale $\tau_{ad} \equiv (k_{ad}c_0)^{-1}$, a desorption timescale $\tau_{de} \equiv (k_{de}c_{ref})^{-1}$, a convective timescale $\tau_{flow} \equiv y_0/v_{Darcy}(t=0)$, a diffusive timescale $\tau_{diff} \equiv y_0^2/D_{2D}$.

There is also a thermal timescale associated with evaporative cooling and heat exchange with the ambient environment, however, in this study we do not focus on thermal effects. Typical values of the various timescales are summarized in Table 5.1. For the relatively large lengthscales considered, the diffusive

timescale	τ_{evap}	τ_{ad}	τ_{de}	τ_{flow}	τ_{diff}
typ. value (s)	10^3	10^3	10^5	100	10^4

Table 5.1: Typical values of timescales.

timescale is typically longer than the others, which implies that diffusive effects are negligible. Since $\tau_{diff} \sim y_0^2$, this may not hold for smaller linewidths.

One can also define an evaporation-induced lengthscale as $L_{evap} \equiv v_{Darcy}(t=0)\tau_{evap}$, which is on order of several cm and which quantifies the maximum possible displacement of an imbibition front before complete evaporation.

5.4.2 Definition of water and colorant front positions

We performed one- and two-dimensional numerical simulations using the computational domains in Fig. 5.6(a,b). The corresponding initial conditions (ICs) are depicted as the blue curve in Fig. 5.6(a) and the red distribution in Fig. 5.6(b). At time $t=0$ we assume that imbibition of the ink in the thickness direction of the paper is already complete and that no ink is left on top of the paper. The water fronts and colorant fronts still coincide, i.e. we assume that no adsorption has occurred, yet. Moreover, we assume that the water in the pores is in capillary equilibrium with the water in the fibers.

The blue curve in Fig. 5.6(a) corresponds to the cross-section of a printed line as depicted in Fig. 5.2(e). The computational domain extends from the center of the printed line $y=0$ to $y=L$, where L is chosen sufficiently large such that the water front never reaches the right boundary prior to complete evaporation

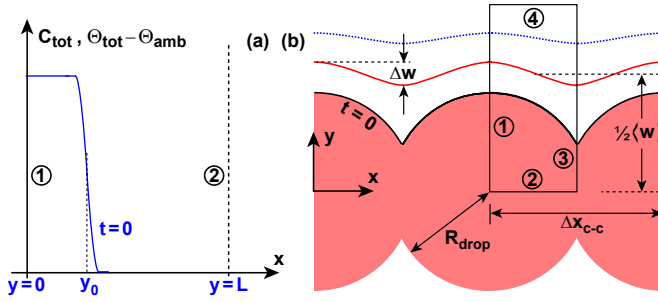


Figure 5.6: Sketch of the computational domains for the (a) 1D and (b) 2D simulations.

For the definition of the water and the colorant front positions, we need to define appropriate concentration thresholds. Since evaporation is taken into account in the model, the quantity of water in the paper will decrease as a function of time. Due to the IC and the inherent symmetries, the moisture distribution will always assume its maximum at $y = 0$. Therefore, if a moisture content threshold relative to $\theta_{tot}(y = 0, t)$ is defined, the corresponding front position will at all times be on order of y_0 , irrespective of the evaporative moisture loss. Therefore, a threshold relative to the *initial* dimensionless total moisture content is set as $0.035 [\theta_{tot}(y = 0, t = 0) - \theta_{amb}]$. This implies that the moisture front position y_w , defined as the maximum y -coordinate for which

$$\theta_{tot}(y, t) - \theta_{amb} > 0.035 [\theta_{tot}(y = 0, t = 0) - \theta_{amb}] \quad (5.5)$$

holds, will start from y_0 , first increase due to imbibition, reach a maximum and eventually approach zero due to evaporation.

The colorant is assumed non-volatile. Consequently, the colorant concentration will tend to increase in time as the solvent evaporates. For this reason we define the colorant threshold as 30% of the *current* maximum of the dye concentration. Analogously, the colorant front position y_c is defined as the largest y -coordinate for which

$$C_{tot}(y, t) > 0.3 \max[C_{tot}(y, t)] . \quad (5.6)$$

Here, the total mass of colorant per unit area of paper is defined as

$$C_{tot} \equiv \frac{c\Theta_w + c_f\Theta_f}{\rho_w} + C_{ad}\Theta_s . \quad (5.7)$$

Figures 5.7(a,b) contrast the dimensionless total moisture content profiles $\theta_{tot}(y) - \theta_{amb}$ for the cases of no evaporation ($k_\infty = 0$) and $k_\infty = 1.3 \cdot 10^{-2}$ m/s.

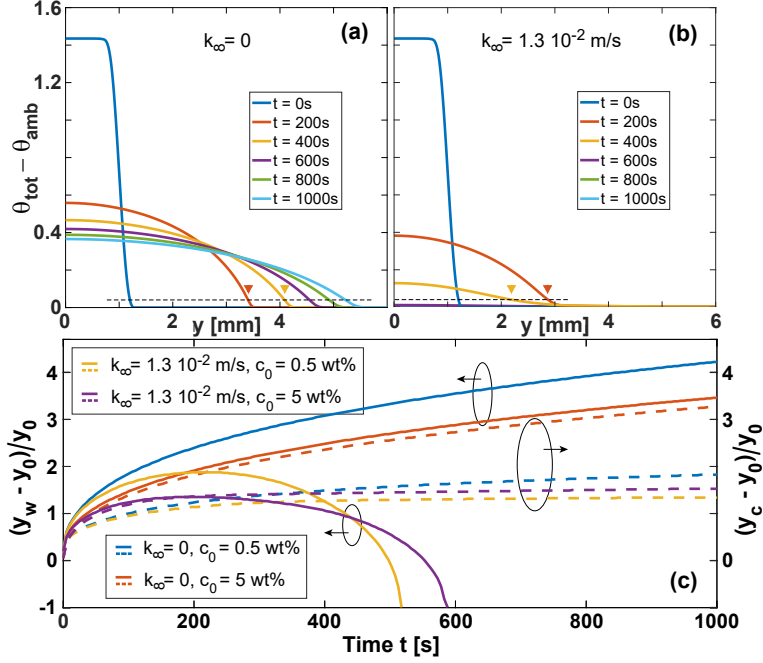


Figure 5.7: (a,b) Dimensionless total moisture content $\theta_{tot}(y) - \theta_{amb}$ for different times and (a) $k_\infty = 0$ (no evaporation) and (b) $k_\infty = 1.3 \cdot 10^{-2}$ m/s. The dashed horizontal lines indicate the threshold level defining the water front position. (c) Relative displacement of the moisture and colorant front positions $(y_w - y_0)/y_0$ (solid lines) and $(y_c - y_0)/y_0$ (dashed lines) as a function of time for different values of k_∞ and c_0 .

Figure 5.7(c) shows typical examples of the time evolution of the water and the colorant front positions for different values of k_∞ and c_0 . The blue and orange sets of curves correspond to simulations for $k_\infty = 0$, i.e. the absence of evaporation. The water and colorant front increase monotonically in time. The yellow and purple curves correspond to simulations for $k_\infty = 1.3 \cdot 10^{-2}$ m/s. In this case, the water front reaches a maximum extension before retracting. At $t \approx 550$ s the curves terminate, because the moisture content everywhere falls below the threshold value of $0.035 \theta_{tot}(y = 0, t = 0)$. The colorant front position saturates roughly when y_w reaches its maximum. Finally, we can express the retardation factor as

$$R_f = \frac{\max(y_c) - y_0}{\max(y_w) - y_0}. \quad (5.8)$$

5.5 Discussion

In the following we present systematic, 1D and 2D numerical simulations of colorant and moisture transport in a sheet of paper. In each plot, we focus on the effect of varying a single parameter while keeping all others constant, on the chromatographic separation of dye and solvent. Moreover, we discuss the phenomenon of dye-precipitation and outline the technological relevance of this work in the context of ink-jet printing. Unless specified otherwise, the values of the relevant parameters used in the simulations are those given in Tab. 5.2. Typical experimental values of the sorption capacity C_∞ for cellulosic

Parameter	Value
k_{ad}	$1 \cdot 10^{-4} \text{ m}^3/(\text{kg s})$
k_{de}	$1 \cdot 10^{-6} \text{ m}^3/(\text{kg s})$
C_∞	1 mg/g
T_{amb}	298.15 K
k_∞	$2.8 \cdot 10^{-3} \text{ m/s}$
y_0	1 mm
$\theta_{tot}(y = 0, t = 0)$	$0.98 \theta_{max}$

Table 5.2: Parameter values of the base case considered in the numerical simulations.

materials range between 0.5 and 100 mg/g [244–247]. Typical experimental values of the dye adsorption timescale τ_{ad} for cellulosic materials range between 5 and 100 min [246–250]. The larger values are typically ascribed to diffusive intra-material transport processes before adsorption can take place.

5.5.1 Variation of the adsorption/desorption rates

In Fig. 5.8(a,b) we present the retardation factor R_f as a function of the initial concentration c_0 for different values of k_{ad} and k_{de} as extracted from 1D simulations. All curves exhibit a characteristic S-shape, i.e. R_f is independent of c_0 for both low and high values of c_0 and exhibits a transition zone from a lower to a higher value of R_f that spans roughly one decade on the abscissa. The high-concentration value of R_f is generally close to 1, because the dye concentration eventually exceeds the sorption capacity of the paper. The low-concentration value of R_f strongly depends on the values of the adsorption rate k_{ad} and the desorption rate k_{de} . The transition zone is well described by the limits $1 \leq \chi_0 \equiv \chi(t = 0) \leq 10$.

An increase of k_{ad} reduces the low-concentration value of R_f , because the dye is taken out of solution faster, which implies it will be transported a shorter

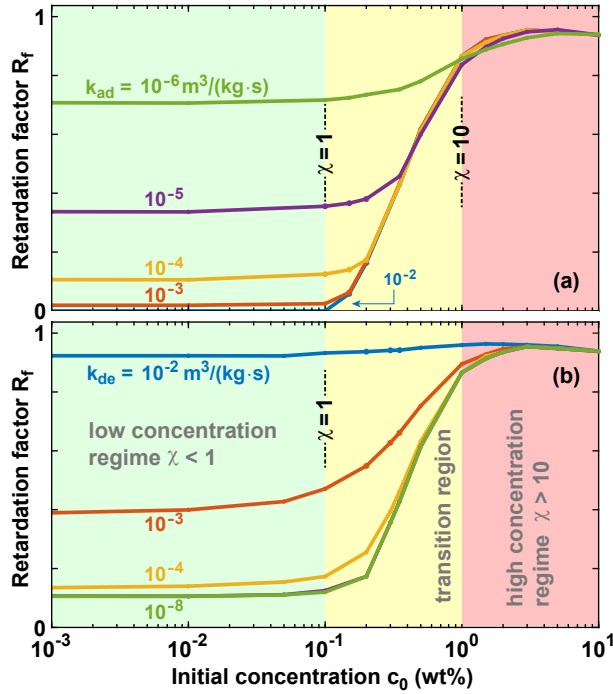


Figure 5.8: Retardation factor R_f as a function of the initial concentration c_0 as extracted from 1D simulations for different values of (a) the adsorption rate k_{ad} and (b) the desorption rate k_{de} .

distance by the flow. An increase of k_{de} tends to increase the low-concentration value of R_f , because adsorbed colorant enters back into the mobile liquid phase faster. Conversely, the limit of $k_{de} \rightarrow 0$ (i.e. $\tau_{de} \rightarrow \infty$) implies that the colorant is irreversibly adsorbed, which reduces its transport distance and thus R_f . The adsorption and desorption rate are therefore an antagonistic pair of parameters as far as their effect on R_f is concerned.

We note that while R_f approaches 0 for sufficiently large k_{ad} , R_f may approach a non-zero value in the limit of small k_{de} as observed in Fig. 5.8(b). This is because desorption is only relevant after adsorption has taken place and a relatively small value of k_{ad} (i.e. when $\tau_{ad} > \tau_{flow}$) can already enforce a finite value of $R_f > 0$.

5.5.2 Variation of the sorption capacity C_∞

Primarily, an increase of C_∞ shifts the transition zone towards proportionally higher values of c_0 .

5.5.3 Variation of y_0 and the initial moisture content

In the line deposition experiments described in Section 5.3.2, the variation of \dot{m} and U_{LJ} effectively changes the width and the moisture content of the deposited line, which serves as the IC for the 1D simulations of the dye redistribution. Therefore, we varied the parameters y_0 (line half width) and the initial dimensionless moisture content $\theta_{tot}(x=0, t=0)$ that characterize the IC [see Fig. 5.6(a)]. The highest sensitivity of R_f with respect to parameter variations is observed in the transition region. A higher moisture content leads to an increase of R_f over the entire range of initial concentrations. In contrast, a larger value of y_0 induces an increase of R_f in the transition region and a decrease in the low-concentration regime. Furthermore, a higher moisture content always leads to a higher relative line broadening. In the limit of y_0 exceeding L_{evap} , R_f no longer depends on y_0 for large y_0 . For small $y_0 < 0.5$ mm, $\max(y_w) - y_0$ scales approximately as $y_0^{1/2}$, whereas the colorant front displacement scales linearly $\max(y_c) - y_0 \sim y_0$. For small $y_0 < 0.5$ mm, which is the regime relevant to the printing of text documents and line drawings, R_f thus increases with increasing y_0 . The linewidth broadening is proportional to the linewidth, which implies that the *relative* linewidth broadening $[\max(y_c) - y_0]/y_0$ is constant in this regime. This makes it particularly easy to compensate for broadening effects in the development of print strategies for a given combination of dye, solvent and substrate.

5.5.4 Variation of the evaporation rate

In inkjet printing the evaporation rate can be enhanced e.g. by measures that increase the mass transfer coefficient k_∞ - such as adding external convection in the gas phase - or by increasing the ambient temperature, which increases the solvent vapor pressure and thus the difference between ρ_s and ρ_{amb} . Evaporation has a strong effect on the time-evolution of the water front position and thus the time available for dye redistribution. The retardation factor tends to increase with higher values of k_∞ and T_{amb} , except in the region where $R_f \geq 0.85$. The biggest increment of R_f occurs in the transition region. The distance over which the water front spreads strongly depends on the effective evaporation rate. In contrast, the corresponding variation in $[\max(y_c) - y_0]/y_0$ is much weaker for initial concentrations c_0 below the transition region.

5.5.5 Line formation in dye-based inkjet printing on paper

In inkjet printing, individual droplets are deposited to generate arbitrary patterns. In the case of straight lines, it is usually desirable that the linewidth

is as homogeneous as possible and does not exhibit undulations. If droplets are deposited with overlap, i.e. with a center-to-center distance Δx_{c-c} smaller than the footprint diameter $2R_{drop}$ (for definitions, see fig 5.6), then undulations tend to be reduced. However, the minimum achievable linewidth then increases. This is the regime relevant to our inkjet deposition experiments in Section 5.3.2.

For a small $R_f \leq 0.1$, the initial undulation amplitude remains essentially unchanged, while the solvent has spread to more than three times the initial line width $\langle w \rangle$. For a medium $R_f \sim 0.5$, the undulation amplitude has decreased to about 50% of the initial value. For a large $R_f \geq 0.9$, the undulation is essentially gone completely, however, at the expense of a colorant linewidth $\langle w \rangle$ increasing to about three times its initial value.

5.5.6 Dye precipitation

It is at first glance surprising that the retardation factors for Rhodamine B and FSS in Fig. 5.3 differ so strongly, although the molecular weights and chemical structures depicted in Fig. 5.1 are comparable. The values of c_0 , at which R_f reaches a level of 0.5, differ by approximately a factor of 10. We believe the origin of the difference to be due to the presence of divalent Ca^{2+} ions due to the CaCl_2 loading in the paper. Hou and Baughman and Vimonses *et al.* have studied the precipitation of anionic dyes in water containing Ca [251,252]. Analogous Ca-induced precipitation effects had previously been observed for anionic surfactants [230,231,233].

Figure 5.9(a-d) presents top-view photographs after deposition of FSS solution droplets of different initial concentrations. The dashed circles approximately outline the maximum droplet footprint as illustrated in Fig. 5.2(b). It is apparent that the color density and thus the dye concentration (per area of paper) has a local maximum at $r = R_0$ for all values of c_0 . We interpret this as a consequence of a concentration maximum of Ca ions, which dissolve from the paper surface into the liquid droplet. Near the droplet contact line, the liquid thickness is smallest. Thus, the ion concentration will be highest (because the dilution of the Ca ion concentration will be smallest) and FSS precipitation will primarily occur there. A second reason is that after a brief initial phase, after ink imbibition in the thickness direction is complete, there is flow inside the droplet towards the contact line, because non-zero moisture content gradients in the paper then exist only beyond $r \geq R_0$. This phenomenon is akin to the evaporation-induced coffee-stain effect and transports precipitated dye towards the contact line.

Figure 5.9(e-h) shows analogous images for Rhodamine-B solution droplets.

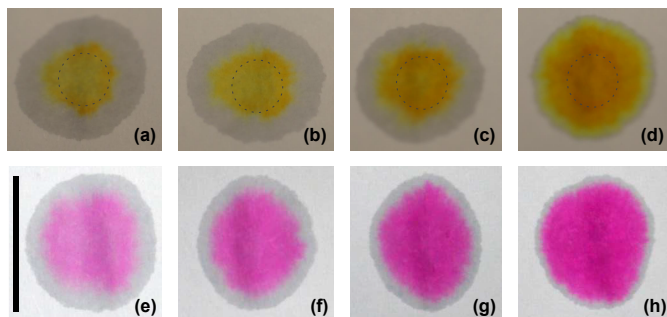


Figure 5.9: (a-d) Top-view photographs after deposition of FSS solution droplets of initial concentrations (a) 0.0125, (b) 0.025, (c) 0.05 and (d) 0.28 wt%. The dashed circles approximately outline the maximum droplet footprint as illustrated in Fig. 5.2(b). (e-h) Analogous images after deposition of Rhodamine-B solution droplets of initial concentrations (a) 0.015, (b) 0.03, (c) 0.06 and (d) 0.12 wt%. The scalebar in (e) corresponds to 1 cm and is valid for all panels.

The color density appears to be rather uniform for $r < R_{dye}$ i.e. behind the dye front and no contact-line enhancement of the dye concentration is observed. This points at the absence of CaCl_2 induced precipitation for the cationic dye.

5.5.7 Technological relevance

In principle chromatographic effects are relevant to all printing processes. However, this is particularly true for inkjet printing because of the typically much lower solid content and much higher solvent concentration in inkjet inks, that provide increased colorant mobility. A number of techniques have been developed in order to optimize the achievable resolution and pattern fidelity by improving and accelerating dye fixation. These include

- [(1)] pretreatments by corona discharges and other plasmas [253–259],
- [(2)] the incorporation of ionic compounds into paper that have the opposite charge polarity as the dye [240, 260–263], [(3)] the use of reactive dyes that form covalent bonds [264–266], [(4)] the use of nanoporous coating layers that increase the effective surface area [240], [(5)] the use of binders that reduce the permeability and thus the ink absorption rate [240], or [(6)] an increase of the solvent evaporation rate by raising the temperature or by using microwave or infrared irradiation to reduce the time available for ink transport [267–272].

In the framework of our adsorption model, strategies (1) to (4) aim at an increase of c_∞ and k_{ad} and/or a decrease of k_{de} , all of which tend to reduce R_f . Strategies (5) and (6) directly aim at minimizing solvent transport.

Our results are not only relevant to dye-based printing inks, but also to pigment-based inks, because the latter typically contain a number of molecularly dissolved additives that are subject to the same retardation phenomena as the dyes we investigated.

5.6 Summary and conclusions

We have studied the transport and chromatographic separation of a model ink consisting of a dilute solution of a colorant in a solvent in thin porous media. We conducted systematic experiments using drop-casting and inkjet deposition of solutions of an anionic and a cationic dye in water on a commercial paper type. The paper was loaded with CaCl_2 in order to facilitate colorant fixation. This leads to a precipitation reaction of the anionic colorant on top of and inside the paper, while the cationic dye was apparently unaffected. The chromatographic retardation as a function of initial concentration of the two dyes differed by an order of magnitude despite that their similar molecular weights and molecular structures.

We developed a comprehensive numerical model that accounts for unsaturated flow and chromatographic separation of a dye solution as well as the presence of permeable fibers, solvent evaporation and heat transfer effects. The model qualitatively reproduces the dependence of the retardation factor on the dye concentration. We have systematically varied the key parameters and evaluated their effect on the broadening and width fluctuations of inkjet deposited colorant lines.

The sensitivity of the retardation factor R_f to changes in operating conditions is generally highest in the transition region, which spans roughly a decade in dye concentration in our model and where R_f changes from a low-concentration to a high-concentration value. In order to optimize pattern fidelity, printing should be performed with the minimal dye concentration, the smallest moisture content, the highest adsorption and the lowest desorption rates, and at the highest evaporation rate possible.

Acknowledgements

This work is part of the research programme ‘*The role of surfactants in spreading, imbibition and sorption of water-based printing inks*’ with project number 14666, which is (partly) financed by the Netherlands Organisation for Scientific Research (NWO). The authors thank Nicolae Tomozeiu, Herman Wijshoff and Louis Saes of Canon Production Printing for the fruitful cooperation.

Author contribution statement

Vignesh Murali developed the experimental setup and the measurement protocols. He conducted all the experiments and analyzed the experimental data. The theoretical model was developed by Gianmarco Venditti. Gianmarco Venditti performed all the numerical simulations and analyzed the numerical data. The manuscript was written by Vignesh Murali and Gianmarco Venditti.

Chapter 6

Concluding remarks

The goals of the research were primarily to develop experimental methods and perform experiments with which the process of ink-imbibition, solvent evaporation and solute adsorption can be studied. The experimental work detailed in this dissertation yields systematic insight into the transport mechanisms that govern the aforementioned processes. In this chapter, the main conclusions are drawn along with some recommendations for future study.

6.1 Conclusions

Infrared thermography to monitor solvent distribution

This dissertation began with a general introduction where the potential of infrared (IR) thermography was highlighted to monitor temperature changes of the paper that are related to the moisture content of the paper. More precisely, the temperature changes are closely related to the time-dependent change of the moisture content. As the first step, Chapter 2 was aimed at quantifying the thermal response of paper to changes in moisture content or moisture distribution. The focus was on attaining steady-state data for 1-D lateral temperature distribution $T(x)$ through infrared (IR) thermography, when paper was wetted through a stationary nozzle that is supplied with water from a syringe pump, and, with the initially dry zones of paper moving into the resulting wet-zone at a constant speed (U_{sub}). The substrate motion into the wet-zone leads to a steady distribution of moisture. Continuous supply from the pump ensures the maintenance of stationary boundary conditions. The obtained results clearly show that the temperature distribution $T(x)$ becomes bi-polar, as (1) the wet-zone becomes colder than ambient due to evaporative cooling and, (2) a temperature maximum (above ambient) occurs near the wet-dry transition. Quantifying the increase in temperature as a function of U_{sub} is the key objective.

A numerical model considering 1-D Richards' equation for unsaturated flow

in porous media with heat-transfer coupled to a 2-D gas-phase domain was developed where the velocity and pressure of the gas-phase, the transport of water-vapor in air and the temperature of the air were solved for. This model captures the thermal response as a function of U_{sub} very well. It is shown that for a given U_{sub} the temperature maximum occurs at low values of moisture content or water saturation (S_w). The water-saturation profiles- and consequently the temperature profiles- are influenced strongly by buoyancy effects induced in the gas-phase surrounding the paper. Buoyancy is induced in the gas phase both due to compositional gradients and because a temperature non-uniformity exists at the substrate. Convection-diffusion of the water-vapor in air therefore plays an important role in understanding the behavior of the system as U_{sub} changes. At low values of U_{sub} , the velocity profile in the gas-phase qualitatively changes. The thermal amplitude ceases to depend on U_{sub} . This shows that control of gas-phase on top of the substrate will be pivotal for robust process control. The results establish the viability of infrared thermography to monitor solvent distribution.

Quantifying moisture content and temperature of paper sheets during ink-jet deposition

Chapter 3 develops on the previous chapter by incorporating ink-jet deposition. The introduction of the ink-jet deposition allows experiments in this chapter to focus on two-dimensional moisture content profiles of the paper, as a finite amount of liquid is added. The amount of liquid deposited is quantified by measuring the flow-rate of the ink-jet at a particular frequency of deposition. The goals were to measure 2-D moisture content (θ_w) and temperature of moving sheets of paper onto which a stationary ink-jet deposits droplets to form lines. Optical light transmission imaging is used to visualize and measure the moisture content with IR thermography to measure the temperature field of the paper as functions of the speed of the substrate (U_{IJ}) and the frequency of deposition (f). Both U_{IJ} and f determine the amount of liquid added per unit length of the paper. The method of optical transmission imaging relies on the refractive index contrast that exist in paper between cellulose-fibres and air. Due to the geometry involved, evaporative cooling controls the evolution of the temperature profile of the paper.

The results of the ink-jet deposition experiments showed that for a fixed U_{IJ} when f decreases, the length of the tail (or the distance printed l_{wet}) decreases and can even fall below $U_{IJ} \times t_d$, with t_d being the printing duration. This shows that l_{wet} is controlled by the evaporation rate and f itself, and to a smaller extent by Darcy flow. The measured thermal response or the temperature

distribution $T(x)$ at a fixed value of t_d is such that for high values of f , the entire wet-zone is uniformly colder than ambient as a longer and a wider zone is approximately uniformly wet. When f decreases, because l_{wet} decreases, the location of the coldest point shifts closer to the impingement point. The thermal amplitude ΔT_{max} , quantifying the evaporative cooling, decreases with decreasing f .

The second mode of experiments involved varying U_{IJ} at a fixed f . Results are analyzed when the printed distance l_{wet} is 4cm long. For low values of U_{IJ} , the results are identical to that of the high f data with a longer, wider and uniformly colder wet-zone. As U_{IJ} increases, the moisture gradients become shallower. The transverse moisture width Δy_w decreases with increasing U_{IJ} . For this mode, the measured thermal response offers some interesting perspectives. As U_{IJ} increases, the coldest point shifts closer to the tail.

Along with the detailed and systematic experiments quantifying θ_w and T of moving paper sheets, a numerical model coupling 2-D Richards' equation for moisture transport and heat-transfer was also developed. The model is built on the same principles that were used for the model developed in the previous chapter. The model captures many of the experimental features to a good extent.

The role of surfactants in altering light-media interaction

In Chapter 4, we extend the ink-jet method to study the role of surfactants. The same type of experiments as discussed in Chapter 3 are performed using optical light transmission imaging and IR thermography. Both the anionic SDS surfactant and the non-ionic Triton-X-100 are used. Moreover, various surfactant bulk concentrations (c_0) are used ranging from 1 CMC to 70 CMC. Surfactants are surface-active solutes and are an important part of many, if not all, water based ink formulations. Their primary role is to reduce the surface tension of the ink. As a first step drop-casting experiments were performed. Drop-casting is essentially casting a drop onto the substrate and observing the light transmission to understand how the light-media interactions are altered by surfactants. The presence of surfactants induces sharp gray-scale transitions in the transmitted intensity that are absent for pure water. This manifests as a dark-zone within the wet-zone and is attributed to the presence of well-defined fronts in the surfactant distribution. The dark-zone is thus interpreted as the locations beyond which surfactant is essentially not present, yet.

During ink-jet deposition, the measured transmitted intensities were significantly higher for surfactant solutions, specifically for large amount of liquid/unit surface. It is also shown that the anionic surfactant SDS induces a higher in-

tensity overshoot than the non-ionic Triton-X-100. The cause of the intensity overshoot is the surfactant induced delay of pore-fiber moisture redistribution. Since the pores are more permeable, when fibrous media are wetted, the pores are filled first. Owing to the larger dimensions of the pores, they become the dominant length scale determining light scattering, because the wavelength λ of visible light is closer to the pores than to that of the fibers. This implies that when moisture enters the pores, light transmission intensity first increases (for the same reason as discussed earlier), then decreases as the liquid is re-distributed into the fibres.

The ink-jet deposition is performed as functions of U_{IJ} and the mass deposition rate \dot{m} . In order to compare the surfactant lines with that of the pure lines studied in the previous chapter, experiments are performed at an identical deposition rate. Overall, the differences in terms of the width of the wet-zones and the thermal amplitudes between the surfactant systems and pure system are small. A very high concentration of $c_0 = 70$ CMC however induces systematically higher values of ΔT_{max} , Δy_w and l_{wet} .

Effect of surfactant adsorption

Adsorption of surfactant molecules onto the fibres causes depletion of surfactant from the liquid-front. Thus, adsorption causes the surfactant front to always lag behind the solvent, because of the loss of surfactant from the pores to the fibres. Studying the spontaneous Darcy flow in the y-direction sheds insights on the surfactant adsorption induced moisture migration. The transverse profile of an ink-jet deposited line with the non-ionic surfactant shows that a dark region characterized by decreased transmission exists at the centre of the wet-zone. This is due to moisture migration away from the zone with locally higher surfactant concentration. Had there been no surfactant adsorption, then such dark zones will not occur because all of the surfactant would remain in the solution. With increasing concentration, the surfactant front can spread ahead of the deposition zone.

Quantifying colorant adsorption

In Chapter 5 the chromatographic separation of dye-based colorants that are molecularly dissolved in water is studied. Since the dyes have color, the adsorption and separation phenomena can be directly visualized and quantified. The non-surface active nature of the colorant implies that capillary pressure does not change as a function of colorant concentration. The chief goal is to measure the retardation of the dye behind the advancing solvent front. An

anionic (Sodium fluorescein salt) and a cationic (Rhodamine-B) dye are used. Both types of experiments that were done for surfactants, i.e., drop-casting and ink-jet deposition to form lines are also performed for the dye-water solutions. For all values of the dye concentration, the solute front falls behind the solvent front. This is quantified through the retardation factor (R_f) as a function of the concentration c_0 of the dye in water. The retardation factor quantifies the distance the solute has spread from the initial zone of deposition to that of the distance the solvent has advanced. It is shown that R_f increases with increasing c_0 because the dyes get transported along with the solvent (due to the Darcy-flow). The characteristic S- shape is attained. It is also seen that Rhodamine-B has significantly higher values of R_f compared to Sodium fluorescein salt for roughly the same values of c_0 . Ink-jet deposition experiments were performed. As the amount of solvent added per unit area of the substrate increases, increase in R_f occurs because the solvent spreads ahead, and the effect of evaporation is relatively weaker. As the amount of ink deposited decreases, the dye-front has not spread beyond the initial deposition zone because the solvent has been rapidly removed by evaporation. Conceptually, this means that R_f is lower. From the perspective of increasing resolution or preventing the broadening of the line, it is beneficial to ink-jet deposit at low values of \dot{m} or high values of U_{IJ} . The results obtained are most relevant for understanding the interplay of phenomena that govern high fidelity and high-resolution in ink-jet printing.

6.2 Recommendations for future study

Sorption induced by the vapor-phase

Infrared thermography was used to quantify phenomena involving solvent imbibition, evaporation and its subsequent condensation. The problem studied comprised of moisture changes induced by addition of the liquid phase into the paper along with removal of liquid content by evaporation and subsequently the addition of moisture from the vapor phase through condensation. The individual effects of these processes in temperature changes were not measured. An interesting aspect can be to study the moisture content increases due to vapor sorption alone. Thermogravimetric analysis (TGA) is a well-established method in which the mass of the sample is measured over time as the temperature of the sample changes. One can benefit from using IR thermography to monitor temperature changes of the paper as air-flow is induced on top of the paper. This may be advantageous than relying on the cumbersome TGA method. The amplitude induced by the heat of sorption will be small, but can

be measured by IR cameras that have very high resolutions. This will have enormous value for industrial ink-jet printing as air-flow on top of the paper is a common feature for enhancing solvent removal.

Measuring transport in the thickness direction of paper

In Chapter 3, ink-jet deposition was introduced and the formation of lines of pure water was studied. However, this study was limited only to lateral moisture distributions as the speed of the substrate was slow. Ink-jet printing is a fast, dynamic process with the droplet sizes being on the order of a few microns and the substrate speeds are substantially higher (on the order of a few m/s). The transient stages when the ink-drops penetrate into the thickness of the paper are paramount to understand. The challenge is that liquid penetration cannot be measured optically, as the paper is optically nontransparent. However, a set-up with high-speed cameras on both sides of the paper (top and bottom) can be used to measure the time taken for optical signals to arise on the underside of paper after a drop is placed on top of the paper.

Heat-moisture coupling

Throughout the work, moisture content history influencing the temperature field of the paper was an aspect heavily relied upon. However, an in-depth consideration is difficult and was not attained. By employing a multiple nozzle ink-jet deposition system, a given area can be wet in a controlled and pre-determined way. This allows one to impose $\theta_w(x, y)$ and then measure and compute $T(x, y)$ rather than measuring and computing both.

Electrical capacitance tomography

An alternative method to measure moisture distribution in the thickness direction of the substrate is electrical capacitance tomography (ECT) which works on the principle that external capacitance measurements can be used to measure electrical permittivity changes (due to moisture penetration) in the substrate of interest. Therefore, development of a combined optical (the one used in this dissertation) and tomographic set-up will go a long way towards 3-D dynamic moisture measurement in paper.

Flourescing surfactants

In Chapter 4 the role of surfactants was explored. The experimental characterization suffered from the limitation that the optical contrasts due to surfactants

were only marginal. Substantial improvement can be made if efforts are taken to find out the type of surfactants that can fluoresce on paper. This can lead to easier measurement of surfactant induced transport processes. Moreover, the surfactant concentration field can be independently measured.

Measuring capillary pressure as a function of moisture content

Throughout the work, modeling relied on parameterization, particularly for characterizing capillary pressure as a function of moisture content. Significant progress can be made if this were measured for systems with and without surfactants.

Different types of substrate

A detailed study on various types of substrates will be of considerable value, because contact angle will be higher for substrates that are partially hydrophobic. Addition of surfactants can therefore cause a reduction in the contact angle leading to changes in the imbibition rate of the solvent.

Coupling Richards equation and lubrication equation

A numerical model coupling transport in porous media and lubrication equation can describe the behaviour of liquid on top of and inside the substrate simultaneously. Such a model will be pivotal also in interpreting data associated with techniques for measuring moisture content in the thickness of the paper.

Pigment based inks

In Chapter 5 the lag of the molecularly dissolved colorants behind the solvent was measured. Such a study for pigment based inks will be crucial. Subsequently, understanding how surfactants alter color-fixation must follow, because the pigment particles can be stabilized by the surfactant. High fidelity printing depends crucially on the pigment-surfactant interactions. Moreover, porous substrates can filter the particles depending on their sizes. thus experiments along the lines shown in Chapter 5 will be required. It is to be noted that the behaviour of the solvent will be the same as discussed.

Viscoelastic response of paper

While this study focused on the transport processes governing ink-jet printing onto paper substrates, the material aspects were chiefly neglected. Paper is a viscoelastic material that can deform due to moisture penetration. Various modes of deformations can occur depending on the moisture gradients that are formed. Thus, an independent study featuring viscoelastic response of paper will be of paramount value for the end quality of ink-jet printed sheets.

Fundamental study of light scattering

A thorough study of light scattering through paper is most necessary. This can shed insights onto many phenomena that are not yet well understood.

Bibliography

- [1] Perelaer J. *PhD Thesis*. Eindhoven University of Technology, Eindhoven, The Netherlands. (Cited on pages 1, 3, 4, and 5.)
- [2] B.-J. de Gans, E. Kazancioglu, W. Meyer, et al. *Macromol. Rapid Commun*, 25:292, 2004. (Cited on page 1.)
- [3] Atasheh Soleimani-Gorgani. *Ink-jet printing*. Institute for Color Science and Technology, Tehran, Iran. (Cited on page 1.)
- [4] J Perelaer. *Ink-jet printing of Functional Polymers for Advanced Applications*. Friedrich-Schiller-University Jena, Jena, Germany US Schubert, Friedrich-Schiller University Jena, Jena, Germany; Jena Center for Soft Matter (JCSM), Jena, Germany. (Cited on page 1.)
- [5] Jungho Park and Jooho Moon. Control of colloidal particle deposit patterns within picoliter droplets ejected by ink-jet printing. *Langmuir*, 22:3506–3513, 2006. (Cited on page 1.)
- [6] C. Ainsley, N. Reis, and B. J. Mater Derby. *Sci*. 37:3155, 2002. (Cited on page 3.)
- [7] Herman Wijshoff. The dynamics of the piezo inkjet printhead operation. *Physics Reports*, 491(4):77–177, June 2010. (Cited on pages 3, 33, and 35.)
- [8] N. Alleborn and H. Raszillier. Spreading and sorption of a droplet on a porous substrate. *Chemical Engineering Science*, 59(10):2071 – 2088, 2004. (Cited on pages 7 and 62.)
- [9] G.I Barenblatt, Iu.P Zheltov, and I.N Kochina. Basic concepts in the theory of seepage of homogeneous liquids in fissured rocks [strata]. *Journal of Applied Mathematics and Mechanics*, 24:1286 – 1303, 1960. (Cited on pages 7, 75, and 76.)
- [10] A. Bandyopadhyay, H. Radhakrishnan, B. V. Ramarao, and S. G. Chatterjee. Moisture sorption response of paper subjected to ramp humidity changes: Modeling and experiments. *Industrial & Engineering Chemistry Research*, 39:219–226, 2000. (Cited on pages 7 and 75.)
- [11] Paula Andrea Marin Zapata, Maurice Fransen, Jan ten Thije Boonkamp, and Louis Saes. Coupled heat and moisture transport in paper with application to a warm print surface. *Applied Mathematical Modelling*, 37:7273 – 7286, 2013. (Cited on pages 7, 75, and 95.)
- [12] Shlomo Magdassi. *The Chemistry of Inkjet Inks*. World Scientific, 2009. (Cited on pages 7 and 89.)
- [13] T.T. Lamminmäki, J.P. Kettle, P.J.T. Puukko, and P.A.C. Gane. The chromatographic separation of anionic dye in inkjet coating structures. *Colloids and Surfaces A: Physicochemical and Engineering Aspects*, 377:304–311, 2011. (Cited on pages 8 and 90.)
- [14] G. Gavelin, editor. *Drying of Paper and Paperboard*. Lockwood (, New York, 1972. (Cited on page 11.)

- [15] S. A. Reardon, M. R. Davis, and P. E. Doe. Friction, heat and mass transfer for paper drying. *Int. J. Heat Mass Transfer*, 41:1313–1325, 1998. (Cited on page 11.)
- [16] O. Polat and A. S. Mujumdar. Drying of pulp and paper. In *Handbook of Industrial Drying*. CRC Press (Boca Raton, 2006. (Cited on page 11.)
- [17] T. Lu and S. Q. Shen. Numerical and experimental investigation of paper drying: Heat and mass transfer with phase change in porous media. *Appl. Thermal Eng*, 27:1248–1258, 2007. (Cited on page 11.)
- [18] D. Bezanovic, C. J. van Duijn, and E. F. Kaasschieter. Analysis of wet pressing of paper: the three-phase model. *Transp Porous Med*, 67:93–113, 2007. (Cited on page 11.)
- [19] K. Niskanen. Paper physics. In *2. Paper Engineers' Association* (Helsinki, 2008. (Cited on page 11.)
- [20] M. Karlsson. Papermaking part 2 - drying. In *2. Paper Engineers' Association* (Helsinki, 2010. (Cited on page 11.)
- [21] A. K Ghosh. Fundamentals of paper drying – theory and application from industrial perspective. In *Evaporation, Condensation and Heat Transfer*. by A. Ahsan, InTech (Rijeka, Croatia, 2011. (Cited on page 11.)
- [22] M. B. Lyne and J. S. Aspler. In *Colloids and Surfaces in Reprographic Technology*, pages 385–420. by M. Hair *et al.*; ACS Symp. Ser. 200, Ink-Paper Interactions in Printing: A Review, 1982. (Cited on page 11.)
- [23] J. F. Oliver, L. Agbezuge, and K. Woodcock. A diffusion approach for modelling penetration of aqueous liquids into paper. *Colloids Surfaces A: Physicochem. Eng*, 89:213–226, 1994. (Cited on page 11.)
- [24] B. E. Yoldas. A dense transparent ink-jet receptive film that provides instantaneous print drying. *J. Mater*, 14, 1999. (Cited on page 11.)
- [25] D. W. Bousfield and G. Karles. Penetration into three-dimensional complex porous structures. *J. Colloid Interface Sci*, 270:396–405, 2004. (Cited on page 11.)
- [26] R. C. Daniel and J. C. Berg. Spreading on and penetration into thin, permeable print media: Application to ink-jet printing. *Adv. Colloid Interface Sci*, 123-126:439–469, 2006. (Cited on pages 11 and 62.)
- [27] J. Hyväluoma, P. Raiskinmäki, A. Jäsberg, A. Koponen, M. Kataja, and J. Timonen. Simulation of liquid penetration in paper. *Phys. Rev*, 73, 2006. (Cited on page 11.)
- [28] A. Kulachenko, P. Gradin, and T. Uesaka. Basic mechanisms of fluting formation and retention in paper. *Mech. Mater*, 39:643–663, 2007. (Cited on page 11.)
- [29] A. M. Miranda, I. L. Menezes-Sobrinho, and M. S. Couto. Spontaneous imbibition experiment in newspaper sheets. *Phys. Rev*, 104, 2010. (Cited on page 11.)
- [30] T. T. Lamminmäki, J. P. Kettle, P. J. T. Puukko, and P. A. C. Gane. Absorption capability and inkjet ink colorant penetration into binders commonly used in pigmented paper coatings. *Ind. Eng*, 50:3287–3294, 2011. (Cited on page 11.)
- [31] T. Lamminmäki, J. Kettle, H. Rautkoski, A. Kokko, and P. Gane. Limitations of current formulations when decreasing the coating layer thickness of papers for inkjet printing. *Ind. Eng*, 50:7251–7263, 2011. (Cited on page 11.)
- [32] T. T. Lamminmäki, J. P. Kettle, and P. A. C. Gane. Absorption and adsorption of dye-based inkjet inks by coating layer components and the implications for print quality. *Colloids Surfaces A: Physicochem. Eng*, 380:79–88, 2011. (Cited on page 11.)

- [33] A. Filenkova, E. Acosta, P. M. Brodersen, R. N. S. Sodhi, and R. Farnood. Distribution of inkjet ink components via tof-sims imaging. *Surf. Interface Anal*, 43:576–581, 2011. (Cited on pages 11 and 82.)
- [34] S. Gao, Z.-W. Wang, C.-Y. Hu, and Y.-M. Wu. Investigation of migration model of printing inks on paper packaging. *J. Food Process Eng*, 37:146–159, 2014. (Cited on page 11.)
- [35] S. C. L. Sousa, A. de O. Mendes, P. T. Fiadeiro, and A. M. M. Ramos. Dynamic interactions of pigment-based inks on chemically modified papers and their influence on inkjet print quality. *Ind. Eng*, 53:4660–4668, 2014. (Cited on page 11.)
- [36] T. Gambaryan-Roisman. Liquids on porous layers: wetting, imbibition and transport processes. *Curr. Opinion Colloid Interface Sci*, 19:320–335, 2014. (Cited on page 11.)
- [37] T. Okubo. Wetting to drying patterns of a water droplet on a printed paper sheet. *Colloid Polym. Sci*, 294:19–26, 2016. (Cited on page 11.)
- [38] Z. Tao, B. Le Borgne, T. Mohammed-Brahim, E. Jacques, and M. Harnois. Spreading and drying impact on printed pattern accuracy due to phase separation of a colloidal ink. *Colloid Polym. Sci*, 296:1749–1758, 2018. (Cited on page 11.)
- [39] W. Hong, J. Zhou, M. Kanungo, N. Jia, and A. D. Dinsmore. Wax spreading in paper under controlled pressure and temperature. *Langmuir*, 34:432–441, 2018. (Cited on page 11.)
- [40] A. Swerin. Dimensional scaling of aqueous ink imbibition and inkjet printability on porous pigment coated paper - a revisit. *Ind. Eng*, 57:16684–16691, 2018. (Cited on page 11.)
- [41] B. Ghanbarian, H. Aslannejad, and A. Raoof. Modeling water imbibition into coated and uncoated papers. *Chem*, 189:33–42, 2018. (Cited on page 11.)
- [42] R. E. Hayes, F. H. Bertrand, and P. A. Tanguy. Modelling of fluid/paper interaction in the application nip of a film coater. In Porous Med, editor, *Transp*, pages 55–72. 40, 2000. (Cited on page 11.)
- [43] E. Levänen, T. Mäntylä, P. Mikkola, and J. B. Rosenholm. Layer buildup on two-layered porous substrate by dip-coating: Modeling and effect of additives on growth rate. *J. Colloid Interface Sci*, 230:186–194, 2000. (Cited on page 11.)
- [44] S. K. Deviseti and D. W. Bousfield. Fluid absorption during forward roll coating of porous webs. *Chem*, 65:3528–3537, 2010. (Cited on page 11.)
- [45] H. E. Yesilalan, S. B. Warner, and R. Laoulache. Penetration of blade-applied viscous coatings into yarns in a woven fabric. *Textile Res*, 80:1930–1941, 2010. (Cited on page 11.)
- [46] X. Ding, T. F. Fuller, and T. A. L. Harris. Predicting fluid penetration during slot die coating onto porous substrates. *Chem*, 99:67–75, 2013. (Cited on page 11.)
- [47] X. Ding, J. P. Ebin, T. A. L. Harris, Z. Li, and T. F. Fuller. Analytical models for predicting penetration depth during slot die coating onto porous media. *AIChE J.*, 60:4241–4252, 2014. (Cited on page 11.)
- [48] X. Ding and T. A. L. Harris. Review on penetration and transport phenomena in porous media during slot die coating. *J. Polymer Sci*, 55:1669–1680, 2017. (Cited on page 11.)

- [49] T. Goda, Y. Sasaki, M. Mizuno, K. Morizawa, H. Katakura, and S. Tomiya. Numerical analysis for predicting the operability window of slot-die coating onto porous media. *J. Coat*, 14:1053–1060, 2017. (Cited on page 11.)
- [50] N. D. Polychronopoulos and T. D. Papathanasiou. Fluid penetration in a deformable permeable web moving past a stationary rigid solid cylinder. In *Porous Med*, editor, *Transp.* 116, 393, 2017. (Cited on page 11.)
- [51] J. F. Pugh. The Infrared measurement of surface moisture in paper. *Tappi J.*, 63:123–135, 1980. (Cited on page 11.)
- [52] S. R. Delwiche, R. E. Pitt, and K. H. Norris. Sensitivity of near-infrared absorption to moisture-content versus water activity in starch and cellulose. *Cereal Chem*, 69:107–109, 1992. (Cited on page 11.)
- [53] S. J. Hashemi, V. G. Comes, R. H. Crotogino, and W. J. M. Douglas. In-plane diffusivity of moisture in paper. *Drying Technol.*, 15:265–294, 1997. (Cited on page 11.)
- [54] J. Berthold, R. J. O. Olsson, and L. Salmean. Water sorption to hydroxyl and carboxylic acid groups in carboxymethylcellulose (cmc) studied with nir-spectroscopy. *Cellulose*, 5:281–298, 1998. (Cited on page 11.)
- [55] O. Berntsson, T. Burger, S. Folestad, L.-G. Danielsson, J. Kuhn, and J. Fricke. Effective sample size in diffuse reflectance near-ir spectrometry. *Anal. Chem*, 71:617–623, 1999. (Cited on page 11.)
- [56] Y. Li, Y. M. Wei, B. Zhang, and Y. L. Yan. Study on the robust nir calibration models for moisture. *Spectroscopy Spectral Analysis*, 25:1963–1967, 2005. (Cited on page 11.)
- [57] H. Tufvesson, S. Eriksson, and T. Lindstrom. Determination of the in-plane wetting of a board structure using nir spectroscopy. *Nord. Pulp Pap*, 22:111–116, 2007. (Cited on page 11.)
- [58] J. Paaso. *Moisture depth profiling in paper using near-infrared spectroscopy*. PhD thesis, University of Oulu, 2007. (Cited on page 11.)
- [59] J. T. Keränen, J. Paaso, O. Timofeev, and H. Kiiskinen. Moisture and temperature measurement of paper in the thickness direction. *Appita J.*, 62:308, 2009. (Cited on page 11.)
- [60] C.-M. Tag, M. Toiviainen, M. Juuti, and P. A. C. Gane ‘dynamic analysis of temporal moisture profiles in heatset printing studied with near-infrared spectroscopy,’ meas. *Sci. Technol.*, 21:105602, 2010. (Cited on page 11.)
- [61] R. Aikio, H. Lindström, P. Suopajarvi, J. Malinen, and M. Mäntylä. Low-noise moisture meter with high speed led techniques. In *Proc. SPIE 7680*, pages 68008–1. 7-10, 2010. (Cited on page 11.)
- [62] D. E. Vickery, J. E. Luce, and J. W. Atkins. Infrared thermography - aid to solving paper-machine moisture profile problems. *Tappi J.*, 61:17–20, 1978. (Cited on page 11.)
- [63] H. T. Kiiskinen, P. I. Pakarinen, M. Luontama, and A.-L. Laitinen. Using infrared thermography as a tool to analyze curling and cockling of paper. In *Proc. SPIE 1682*. 134, 1992. (Cited on page 11.)
- [64] A. Tanaka, Y. Otsuka, and T. Yamauchi. In-plane fracture toughness testing of paper using thermography. *Tappi J.*, 80:222–226, 1997. (Cited on page 11.)
- [65] H. T. Kiiskinen, H. K. Kukkonen, P. I. Pakarinen, and A. J. Laine. Infrared thermography examination of paper structure. *Tappi J.*, 80:159–162, 1997. (Cited on page 11.)

- [66] H. T. Kiiskinen and P. I. Pakarinen. Infrared thermography at examination of paper structure. In *Proc. SPIE 3361*, pages 228–233, 1998. (Cited on page 11.)
- [67] B. Hojjatie, A. Abedi, and D. W. Coffin. Quantitative determination of in-plane moisture distribution in paper by infrared thermography. *Tappi J.*, 84:71–71, 2001. (Cited on page 11.)
- [68] C. Hyll, H. Vomhoff, and M. Nygard. Analysis of the plastic and elastic energy during the deformation and rupture of a paper sample using thermography. *Nord. Pulp Pap.*, 27:329–334, 2012. (Cited on page 11.)
- [69] C. Hyll, H. Vomhoff, and L. Mattsson. Directional emittance of dry and moist paper. *Nord. Pulp Pap.*, 29:294–303, 2014. (Cited on page 11.)
- [70] A. Tysen and H. Vomhoff. Method for the quantification of in-plane drying non-uniformity. *Nord. Pulp Pap.*, 30:286–295, 2015. (Cited on page 11.)
- [71] H. Aslannejad, A. Terzis, S. M. Hassanizadeh, and B. Weigand. Occurrence of temperature spikes at a wetting front during spontaneous imbibition. *Sci. Rep.*, 7:7268, 2017. (Cited on page 11.)
- [72] T. Enomae, H. Kataoka, and F. Onabe. In-plane distribution of paper absorbency measured by liquid absorption profilometer. *Sen'i Gakkaishi*, 55:65, 1999. (Cited on page 12.)
- [73] C. J. Kuijpers, T. A. P. van Stiphout, H. P. Huinink, N. Tomozeiu, S. J. F. Erich, and O. C. G. Adan. Quantitative measurements of capillary absorption in thin porous media by the automatic scanning absorptometer. *Chem*, 178:70–81, 2018. (Cited on page 12.)
- [74] A. Szymkiewicz. *Modelling Water Flow in Unsaturated Porous Media*. Springer, Berlin, 2013. (Cited on page 17.)
- [75] F. J. Leij, W. B. Russell, and S. M. Lesch. Closed-form expressions for water retention and conductivity data. *Ground Water*, 35:848–858, 1997. (Cited on pages 17, 47, and 75.)
- [76] A. Ashari and H. Vahedi Tafreshi. General capillary pressure and relative permeability expressions for throughplane fluid transport in thin fibrous sheets. *Colloids Surfaces A: Physicochem. Eng.*, 346:114–122, 2009. (Cited on page 17.)
- [77] H. Aslannejad and S. M. Hassanizadeh. Study of hydraulic properties of uncoated paper: Image analysis and pore-scale modeling. In *Porous Med*, editor, *Transp*, pages 67–81. 120, 2017. (Cited on page 17.)
- [78] H. Aslannejad, S. M. Hassanizadeh, A. Raouf, D. A. M. de Winter, N. Tomozeiu, and M. T. van Genuchten. Characterizing the hydraulic properties of paper coating layer using fib-sem tomography and 3d pore-scale modeling. *Chem*, 160:275–280, 2017. (Cited on page 17.)
- [79] D. A. Nield and A. Bejan. *Convection in Porous Media*. Springer (Cham, Switzerland, 5th edition, 2017. (Cited on page 18.)
- [80] S. A. Lavrykov and B. V. Ramarao. Thermal properties of copy paper sheets. *Drying Technol.*, 30:297–311, 2012. (Cited on page 18.)
- [81] M. C. Asensio, J. Yagoobi, and A. D. Stevens. Measurements of thermal contact conductance for a paper/metal interface and effective conductivity of machine samples. *Drying Technol.*, 11:1371–1384, 1993. (Cited on page 18.)

- [82] H. Imakoma, T. Yano, K. Kubota, N. Ohomura, and K. Kataoka. Moisture content dependence of anisotropic effective thermal conductivity for recycled paper. *Kagaku Kogaku Ronbunshu*, 26:105–107, 2000. (Cited on page 18.)
- [83] F. W. Murray and J. Appl. Meteor. **6**. pages 203–204, 1966. (Cited on page 19.)
- [84] G. R. Thorpe and S. Whitaker. Local mass and thermal equilibria in ventilated grain bulks. part i: The development of heat and mass conservation equations. *J. Stored Prod*, 28:15–27, 1992. (Cited on page 20.)
- [85] P. W. Gibson. Modeling convection/diffusion processes in porous textiles with inclusion of humidity-dependent air permeability. *Int. Comm*, 24:709–724, 1997. (Cited on page 20.)
- [86] W. R. Foss, C. A. Bronkhorst, and K. A. Bennett. Simultaneous heat and mass transport in paper sheets during moisture sorption from humid air. *Int. J. Heat Mass Transfer*, 46:2875–2886, 2003. (Cited on page 20.)
- [87] L. Zhongxuan, L. Fengzhi, L. Yingxi, and L. Yi. Effect of the environmental atmosphere on heat, water and gas transfer within hygroscopic fabrics. *J. Comp*, 163:199–210, 2004. (Cited on page 20.)
- [88] G. R. Thorpe. Heat and moisture transfer in hygroscopic porous media: Two contrasting analyses. In *Proc. 5th Int, Fluid Mechanics and Thermodynamics* (Sun City, South Africa, 2007. Conf. on Heat Transfer. (Cited on page 20.)
- [89] W. J. Brickman, H. B. Dunford, E. M. Tory, J. L. Morrison, and R. K. Brown. The reactivity of cellulose ii. *Can*, 31, 1953. (Cited on page 20.)
- [90] J. Greyson and A. A. Levi ‘calorimetric measurements of the heat of sorption of water vapor on dry swollen cellulose,’ j. *Polymer Sci*, 1:3333–3342, 1963. (Cited on page 20.)
- [91] S. Park, R. A. Venditti, H. Jameel, and J. J. Pawlak. Studies of the heat of vaporization of water associated with cellulose fibers characterized by thermal analysis. *Cellulose*, 14:195–204, 2007. (Cited on page 20.)
- [92] I. Portugal, V. M. Dias, R. F. Duarte, and D. V. Evtuguin. Hydration of cellulose/silica hybrids assessed by sorption isotherms. *J. Phys*, 114:4047–4055, 2010. (Cited on page 20.)
- [93] C. H. Heo, H. Cho, and Y.-K. Yeo. Dynamic modeling of paper drying processes. *Korean J. Chem*, 28:1651–1657, 2011. (Cited on page 20.)
- [94] A. H. Bedane, H. Xiao, M. Eic, and M. Farmahini-Farahani. Structural and thermodynamic characterization of modified cellulosefiber-based materials and related interactions with water vapor. *Appl. Surf*, 351:725–737, 2015. (Cited on page 20.)
- [95] P. Leuk, M. Schneeberger, U. Hirn, and W. Bauer. Heat of sorption: A comparison between isotherm models and calorimeter measurements of wood pulp. *Drying Technol.*, 34:563–573, 2016. (Cited on page 20.)
- [96] H. Weisser and F. Liebenspacher. Determination of water content and moisture sorption isotherms of cellulose packaging material. In *Food Properties and Computer-Aided Engineering of Food Processing Systems*, pages 223–230. by R. P. Singh and A. G. Medina, Kluwer, 1989. (Cited on page 21.)
- [97] H. Gupta and S. G. Chatterjee. Parallel diffusion of moisture in paper. part 1: Steady-state conditions. *Ind. Eng*, 42:6582–6592, 2003. (Cited on page 21.)

- [98] M. G. A. Vieira and S. C. S. Rocha. Mathematical modeling of handmade recycled paper drying kinetics and sorption isotherms. *Brazilian J. Chem*, 25:299–312, 2008. (Cited on page 21.)
- [99] J.-W. Rhim and J. H. Lee ‘thermodynamic analysis of water vapor sorption isotherms and mechanical properties of selected paper-based food packaging materials,’ *J. Food Sci*, 74, 2009. (Cited on page 21.)
- [100] A. H. Bedane, M. Eic, M. Farmahini-Farahani, and H. Xiao. Water vapor transport properties of regenerated cellulose and nanofibrillated cellulose films. *J. Membrane Sci*, 493:46–57, 2015. (Cited on page 21.)
- [101] H. Sirringhaus, T. Kawase, R. H. Friend, T. Shimoda, M. Inbasekaran, W. Wu, and E. P. Woo. High-resolution inkjet printing of all-polymer transistor circuits. *Science*, 290:2123–2126, 2000. (Cited on page 33.)
- [102] Paul Calvert. Inkjet Printing for Materials and Devices. *Chem. Mater.*, 13:3299–3305, October 2001. (Cited on page 33.)
- [103] Tatsuya Shimoda, Yasuo Matsuki, Masahiro Furusawa, Takashi Aoki, Ichio Yudasaka, Hideki Tanaka, Haruo Iwasawa, Daohai Wang, Masami Miyasaka, and Yasumasa Takeuchi. Solution-processed silicon films and transistors. *Nature*, 440:783–786, 2006. (Cited on page 33.)
- [104] Laure Fabie and Thierry Ondarcuhu. Writing with liquid using a nanodispenser: spreading dynamics at the sub-micron scale. *Soft Matter*, 8:4995–5001, 2012. (Cited on page 33.)
- [105] S. Ubal, B. Xu, B. Derby, and P. Grassia. Continuous Deposition of a Liquid Thread onto a Moving Substrate. Numerical Analysis and Comparison With Experiments. *Journal of Fluids Engineering*, 134:021301, 2012. (Cited on page 33.)
- [106] Leanne Friedrich and Matthew Begley. In situ characterization of low-viscosity direct ink writing: Stability, wetting, and rotational flows. *Journal of Colloid and Interface Science*, 529:599 – 609, 2018. (Cited on page 33.)
- [107] Rahul Karyappa, Terry Ching, and Michinao Hashimoto. Embedded ink writing (eiw) of polysiloxane inks. *ACS Applied Materials & Interfaces*, 12:23565–23575, 2020. (Cited on page 33.)
- [108] Jennifer A Lewis. Direct-write assembly of ceramics from colloidal inks. *Current Opinion in Solid State and Materials Science*, 6:245 – 250, 2002. (Cited on page 33.)
- [109] Bradley K. Deuser, Lie Tang, Robert G. Landers, Ming C. Leu, and Greg E. Hilmas. Hybrid Extrusion Force-Velocity Control Using Freeze-Form Extrusion Fabrication for Functionally Graded Material Parts. *Journal of Manufacturing Science and Engineering*, 135:041015, 2013. (Cited on page 33.)
- [110] Brian N. Turner, Robert Strong, and Scott A. Gold. A review of melt extrusion additive manufacturing processes: I. process design and modeling. *Rapid Prototyping Journal*, 20:192–204, 2014. (Cited on page 33.)
- [111] Huanxiong Xia, Jiakai Lu, Sadegh Dabiri, and Gretar Tryggvason. Fully resolved numerical simulations of fused deposition modeling. part i: fluid flow. *Rapid Prototyping Journal*, 24:463–476, 2018. (Cited on page 33.)
- [112] Zedong Li, Hao Liu, Cheng Ouyang, Wei Hong Wee, Xingye Cui, Tian Jian Lu, Belinda Pingguan-Murphy, Fei Li, and Feng Xu. Recent advances in pen-based writing electronics and their emerging applications. *Advanced Functional Materials*, 26:165–180, 2016. (Cited on page 34.)

- [113] Jungchul Kim, Myoung-Woon Moon, Kwang-Ryeol Lee, L. Mahadevan, and Ho-Young Kim. Hydrodynamics of writing with ink. *Phys. Rev. Lett.*, 107:264501, 2011. (Cited on page 34.)
- [114] Jungchul Kim, Myoung-Woon Moon, and Ho-Young Kim. Dynamics of hemiwicking. *Journal of Fluid Mechanics*, 800:57–71, 2016. (Cited on page 34.)
- [115] P. C. Duineveld. The stability of ink-jet printed lines of liquid with zero receding contact angle on a homogeneous substrate. *Journal of Fluid Mechanics*, 477:175–200, February 2003. (Cited on page 34.)
- [116] Alice B. Thompson, Carl R. Tipton, Anne Juel, Andrew L. Hazel, and Mark Dowling. Sequential deposition of overlapping droplets to form a liquid line. *Journal of Fluid Mechanics*, 761:261–281, 2014. (Cited on page 34.)
- [117] Wenchao Zhou, Drew Loney, Andrei G. Fedorov, F. Levent Degertekin, and David W. Rosen. Shape evolution of multiple interacting droplets in inkjet deposition. *Rapid Prototyping Journal*, 21:373–385, 2015. (Cited on page 34.)
- [118] K. Franke and S. Rose. Ink-deposition model: the relation of writing and ink deposition processes. In *Ninth International Workshop on Frontiers in Handwriting Recognition*, pages 173–178, 2004. (Cited on page 34.)
- [119] Vignesh Murali, Jos C.H. Zeegers, and Anton A. Darhuber. Infrared thermography of sorptive heating of thin porous media – Experiments and continuum simulations. *International Journal of Heat and Mass Transfer*, 147:118875, February 2020. (Cited on pages 34, 35, 47, 56, 57, 62, and 65.)
- [120] A. F. Forughi, S. I. Green, and B. Stoeber. Optical transparency of paper as a function of moisture content with applications to moisture measurement. *Review of Scientific Instruments*, 87:023706, 2016. (Cited on pages 34, 62, and 66.)
- [121] L. A. Richards. Capillary conduction of liquids through porous mediums. *Physics*, 1:318–333, November 1931. (Cited on page 34.)
- [122] Tapio Fabritius, Juha Saarela, and Risto Myllyla. Determination of the refractive index of paper with clearing agents. In Willy L. Bohn, Vladimir S. Golubev, Andrey A. Ionin, and Vladislav Ya. Panchenko, editors, *International Conference on Lasers, Applications, and Technologies 2005: High-Power Lasers and Applications*, volume 6053, pages 265 – 272. SPIE, 2006. (Cited on page 37.)
- [123] G. I. Mantanis, R. A. Young, and R. M. Rowell. Swelling of compressed cellulose fiber webs in organic liquids. *Cellulose*, 2:1–22, 1995. (Cited on page 39.)
- [124] Martina Botkova, Stefan Suty, Michal Jablonsky, Lucia Kucerkova, and Milan Vrska. Monitoring of kraft pulps swelling in water. *Cellulose Chem. Technol.*, 47:95–102, 2013. (Cited on page 39.)
- [125] Jonghyun Ha and Ho-Young Kim. Capillarity in soft porous solids. *Annual Review of Fluid Mechanics*, 52:263–284, 2020. (Cited on page 39.)
- [126] Adam Szymkiewicz. *Modelling water flow in unsaturated porous media: accounting for nonlinear permeability and material heterogeneity*. GeoPlanet. Springer, New York, 2013. OCLC: ocn768170119. (Cited on pages 45 and 95.)
- [127] A. Ashari and H. Vahedi Tafreshi. General capillary pressure and relative permeability expressions for through-plane fluid transport in thin fibrous sheets. *Colloids and Surfaces A: Physicochemical and Engineering Aspects*, 346(1):114–122, August 2009. (Cited on pages 47 and 75.)

- [128] D. A. Nield and A. Bejan. Convection in Porous Media, 2013. (Cited on page 47.)
- [129] W. James Brickman, H. Brian Dunford, Elmer M. Tory, John L. Morrison, and Robert K. Brown. The reactivity of cellulose II. *Can. J. Chem.*, 31(6):550–563, June 1953. (Cited on page 47.)
- [130] J. Greyson and A. A. Levi. Calorimetric measurements of the heat of sorption of water vapor on dry swollen cellulose. *Journal of Polymer Science Part A: General Papers*, 1(11):3333–3342, 1963. (Cited on page 47.)
- [131] Sunkyu Park, Richard A. Venditti, Hasan Jameel, and Joel J. Pawlak. Studies of the heat of vaporization of water associated with cellulose fibers characterized by thermal analysis. *Cellulose*, 14(3):195–204, May 2007. (Cited on page 47.)
- [132] Inês Portugal, Vânia M. Dias, Rui F. Duarte, and Dmitry V. Evtuguin. Hydration of Cellulose/Silica Hybrids Assessed by Sorption Isotherms. *J. Phys. Chem. B*, 114(11):4047–4055, March 2010. (Cited on page 47.)
- [133] Chang Hoe Heo, Hyunjun Cho, and Yeong-Koo Yeo. Dynamic modeling of paper drying processes. *Korean J. Chem. Eng.*, 28(8):1651–1657, August 2011. (Cited on page 47.)
- [134] Alemayehu H. Bedane, Huining Xiao, Mladen Eić, and Madjid Farmahini-Farahani. Structural and thermodynamic characterization of modified cellulose fiber-based materials and related interactions with water vapor. *Applied Surface Science*, 351:725–737, October 2015. (Cited on pages 47 and 48.)
- [135] Patrick Leuk, Michael Schneeberger, Ulrich Hirn, and Wolfgang Bauer. Heat of sorption: A comparison between isotherm models and calorimeter measurements of wood pulp. *Drying Technology*, 34(5):563–573, April 2016. Publisher: Taylor & Francis eprint: <https://doi.org/10.1080/07373937.2015.1062391>. (Cited on page 47.)
- [136] Horst Weisser and Franz Liebenspacher. Determination of Water Content and Moisture Sorption Isotherms of Cellulose Packaging Material. In R. Paul Singh and Augusto G. Medina, editors, *Food Properties and Computer-Aided Engineering of Food Processing Systems*, NATO ASI Series, pages 223–230. Springer Netherlands, Dordrecht, 1989. (Cited on page 48.)
- [137] M. G. A. Vieira and S. C. S. Rocha. Mathematical modeling of handmade recycled paper drying kinetics and sorption isotherms. *Braz. J. Chem. Eng.*, 25(2):299–312, June 2008. (Cited on page 48.)
- [138] Jong-Whan Rhim and Jun Ho Lee. Thermodynamic Analysis of Water Vapor Sorption Isotherms and Mechanical Properties of Selected Paper-Based Food Packaging Materials. *Journal of Food Science*, 74(9):E502–E511, 2009. (Cited on page 48.)
- [139] Hemant Gupta and Siddharth G. Chatterjee. Parallel Diffusion of Moisture in Paper. Part 1: Steady-State Conditions. *Ind. Eng. Chem. Res.*, 42(25):6582–6592, December 2003. Publisher: American Chemical Society. (Cited on page 48.)
- [140] F. W. Murray. On the Computation of Saturation Vapor Pressure. *J. Appl. Meteor.*, 6(1):203–204, February 1967. Publisher: American Meteorological Society. (Cited on page 48.)
- [141] J. D. Sartor and C. E. Abbott. Prediction and Measurement of the Accelerated Motion of Water Drops in Air. *Journal of Applied Meteorology*, 14:232–239, 03 1975. (Cited on page 53.)

- [142] Oskar Javier González Pedraza, J. Jesús Pacheco Ibarra, Carlos Rubio-Maya, Sergio Ricardo Galván González, and Jorge Alberto Rangel Arista. Numerical study of the drift and evaporation of water droplets cooled down by a forced stream of air. *Applied Thermal Engineering*, 142:292 – 302, 2018. (Cited on page 53.)
- [143] C Bouchenna, M Aitsaada, S Chikh, and L Tadrist. Fluid flow inside and outside an evaporating sessile drop. *Journal of Physics: Conference Series*, 925:012006, 2017. (Cited on page 57.)
- [144] K. Kendall and J.C. Padget. Latex coalescence. *International Journal of Adhesion and Adhesives*, 2:149 – 154, 1982. (Cited on page 57.)
- [145] Vignesh Murali, Gianmarco Venditti, Jos C.H. Zeegers, and Anton A. Darhuber. Inkjet deposition of lines onto thin moving porous media - experiments and simulations. *International Journal of Heat and Mass Transfer*, 176:121466, 2021. (Cited on pages 58, 63, 66, 67, 74, 76, 91, 94, and 96.)
- [146] Boris Zhmud and Fredrik Tiberg. Surfactants in ink-jet inks. In David R. Karsa, editor, *Surfactants in Polymers, Coatings, Inks, and Adhesives*, chapter 8. Blackwell, Oxford, 2003. (Cited on page 61.)
- [147] Yulin Deng and Marcos Abazeri. Contact angle measurement of wood fibers in surfactant and polymer solutions. *Wood and Fiber Science*, 30:155–164, 1998. (Cited on page 61.)
- [148] Victoria Dutschk, Konstantin G Sabbatovskiy, Martin Stolz, Karina Grundke, and Victor M Rudoy. Unusual wetting dynamics of aqueous surfactant solutions on polymer surfaces. *Journal of Colloid and Interface Science*, 267:456 – 462, 2003. (Cited on page 61.)
- [149] Victor M. Starov. Surfactant solutions and porous substrates: spreading and imbibition. *Advances in Colloid and Interface Science*, 111:3 – 27, 2004. (Cited on pages 61 and 62.)
- [150] Malgorzata Graca, Jeroen H.H. Bongaerts, Jason R. Stokes, and Steve Granick. Friction and adsorption of aqueous polyoxyethylene (tween) surfactants at hydrophobic surfaces. *Journal of Colloid and Interface Science*, 315:662 – 670, 2007. (Cited on page 61.)
- [151] Merve Dandan Doganci, Belma Uyar Sesli, and H. Yildirim Erbil. Diffusion-controlled evaporation of sodium dodecyl sulfate solution drops placed on a hydrophobic substrate. *Journal of Colloid and Interface Science*, 362:524 – 531, 2011. (Cited on page 61.)
- [152] Daniela Fell, GAuernhammer, Elmar Bonaccorso, Chuanjun Liu, Rudi Sokuler, and Hans-Jürgen Butt. Influence of surfactant concentration and background salt on forced dynamic wetting and dewetting. *Langmuir*, 27:2112–2117, 2011. (Cited on page 61.)
- [153] Yu. G. Bogdanova, V. D. Dolzhikova, D. S. Tsvetkova, I. M. Karzov, and A. Yu. Alent'ev. Contact angles as indicators of the polymer surface structure. *Journal of Structural Chemistry*, 52:1187 – 1194, 2011. (Cited on page 61.)
- [154] Thritima Sritapunya, Boonyarach Kitiyanan, John F. Scamehorn, Brian P. Grady, and Sumaeth Chavadej. Wetting of polymer surfaces by aqueous surfactant solutions. *Colloids and Surfaces A: Physicochemical and Engineering Aspects*, 409:30 – 41, 2012. (Cited on page 61.)
- [155] Katarzyna Szymczyk, Anna Zdziennicka, Joanna Krawczyk, and Bronislaw Janczuk. Correlation between wetting, adhesion and adsorption in the polymer–aqueous solutions of ternary surfactant mixtures–air systems. *Applied Surface Science*, 288:488 – 496, 2014. (Cited on page 61.)

- [156] Diana Mafko, Anna Zdziennicka, Joanna Krawczyk, and Bronislaw Janczuk. Wettability prediction of such polymers as polyethylene and polytetrafluoroethylene by aqueous solutions of classical surfactants and biosurfactants. *Colloids and Surfaces A: Physicochemical and Engineering Aspects*, 506:409 – 415, 2016. (Cited on page 61.)
- [157] Thu Thi Yen Le, Siam Hussain, and Shi-Yow Lin. A study on the determination of the critical micelle concentration of surfactant solutions using contact angle data. *Journal of Molecular Liquids*, 294:111582, 2019. (Cited on page 61.)
- [158] Robert Paul Held. Surfactant system for ink jet inks for printing on hydrophobic surfaces, 1998. US Patent 5,852,075. (Cited on page 61.)
- [159] Paul J Bruinsma and Noah C Lassar. Inkjet inks which improve drop-velocity stability and prolong resistor life in inkjet pens, 2003. US Patent 6,607,268. (Cited on page 61.)
- [160] Masayuki Koyano, Hiroshi Goto, Tamotsu Aruga, Kiyofumi Nagai, and Toshiroh Tokuno. Ink set, ink cartridge, inkjet recording method, and inkjet recording apparatus, 2013. US Patent 8,435,339. (Cited on page 61.)
- [161] Sadano Okuda, Tsutomu Nio, Hiroshi Hayashi, Shinichiro Shimura, Takayuki Shimizu, Masahiko Abe, Hideki Sakai, and Kenichi Sakai. W/o emulsion ink for inkjet, 2010. US Patent 7,717,989. (Cited on page 61.)
- [162] Sandra Helton McCain, Terence Edward Franey, Ashok Vishnu Gangal, and Agnes Kam Zimmer. Ink jet ink containing wetting agent, 1999. US Patent 5,981,623. (Cited on page 61.)
- [163] John R Moffatt. Bleed alleviation in ink-jet inks, 1992. US Patent 5,116,409. (Cited on page 61.)
- [164] John R Moffatt and James P Shields. Bleed alleviation using zwitterionic surfactants and cationic dyes, 1992. US Patent 5,106,416. (Cited on page 61.)
- [165] Takashi Tamai, Michihiko Namba, and Akihiko Matsuyama. Inkjet recording ink, ink cartridge and inkjet recording method, 2014. US Patent 8,727,523. (Cited on page 61.)
- [166] M. Tschapek and L. Boggio. Surfactants and soil water evaporation and migration. *Journal of Plant Nutrition and Soil Science*, 144:112–120, 1981. (Cited on page 62.)
- [167] R. E. Zartman and Richard A. Bartsch. Using Surfactants to Enhance Drainage from a Dewatered Column. *Soil Science*, 149:52–55, 1990. (Cited on page 62.)
- [168] Milind V Karkare, Hoa T La, and Tomlinson Fort. Criteria for effectiveness of surfactants as water-moving agents in ”unsaturated” wet sand. *Langmuir*, 9:1684–1690, 1993. (Cited on page 62.)
- [169] Milind V Karkare and Tomlinson Fort. Water movement in ”unsaturated” porous media due to pore size and surface tension induced capillary pressure gradients. *Langmuir*, 9:2398–2403, 1993. (Cited on pages 62 and 82.)
- [170] James E. Smith and Robert W. Gillham. The effect of concentration-dependent surface tension on the flow of water and transport of dissolved organic compounds: A pressure head-based formulation and numerical model. *Water Resources Research*, 30:343–354, 1994. (Cited on page 62.)
- [171] E.J. Henry, J.E. Smith, and A.W. Warrick. Solubility effects on surfactant-induced unsaturated flow through porous media. *Journal of Hydrology*, 223:164 – 174, 1999. (Cited on pages 62 and 82.)

- [172] Chris L. Brown, Gary A. Pope, Linda M. Abriola, and Kamy Sepehrnoori. Simulation of surfactant-enhanced aquifer remediation. *Water Resources Research*, 30:2959–2977, 1994. (Cited on page 62.)
- [173] E.J Henry and J.E Smith. The effect of surface-active solutes on water flow and contaminant transport in variably saturated porous media with capillary fringe effects. *Journal of Contaminant Hydrology*, 56:247 – 270, 2002. (Cited on page 62.)
- [174] E. J. Henry, J. E. Smith, and A. W. Warrick. Two-dimensional modeling of flow and transport in the vadose zone with surfactant-induced flow. *Water Resources Research*, 38:33–1 – 33–16, 2002. (Cited on page 62.)
- [175] Klaus M. Rathfelder, Linda M. Abriola, Michael A. Singletary, and Kurt D. Pennell. Influence of surfactant-facilitated interfacial tension reduction on chlorinated solvent migration in porous media: observations and numerical simulation. *Journal of Contaminant Hydrology*, 64:227 – 252, 2003. (Cited on page 62.)
- [176] Kevin T Hodgson and John C Berg. The effect of surfactants on wicking flow in fiber networks. *Journal of Colloid and Interface Science*, 121:22–31, 1988. (Cited on pages 62, 64, 73, and 84.)
- [177] S. H. Davis and L. M. Hocking. Spreading and imbibition of viscous liquid on a porous base. *Physics of Fluids*, 11:48–57, 1999. (Cited on page 62.)
- [178] S. H. Davis and L. M. Hocking. Spreading and imbibition of viscous liquid on a porous base. ii. *Physics of Fluids*, 12:1646–1655, 2000. (Cited on page 62.)
- [179] V.M. Starov, S.R. Kostvintsev, V.D. Sobolev, M.G. Velarde, and S.A. Zhdanov. Spreading of liquid drops over dry porous layers: Complete wetting case. *Journal of Colloid and Interface Science*, 252:397 – 408, 2002. (Cited on page 62.)
- [180] Markus Hilpert and Avishai Ben-David. Infiltration of liquid droplets into porous media: Effects of dynamic contact angle and contact angle hysteresis. *International Journal of Multiphase Flow*, 35:205–218, 2009. (Cited on page 62.)
- [181] B. Markicevic and H. K. Navaz. Primary and secondary infiltration of wetting liquid sessile droplet into porous medium. *Transport in Porous Media*, 85:953–974, 2010. (Cited on page 62.)
- [182] Jarl B. Rosenholm. Liquid spreading on solid surfaces and penetration into porous matrices: Coated and uncoated papers. *Advances in Colloid and Interface Science*, 220:8–53, 2015. (Cited on page 62.)
- [183] Leonardo Espin and Satish Kumar. Droplet spreading and absorption on rough, permeable substrates. *Journal of Fluid Mechanics*, 784:465–486, 2015. (Cited on page 62.)
- [184] Hua Tan. Absorption of picoliter droplets by thin porous substrates. *AIChE Journal*, 63:1690–1703, 2017. (Cited on page 62.)
- [185] Truong Pham and Satish Kumar. Imbibition and evaporation of droplets of colloidal suspensions on permeable substrates. *Phys. Rev. Fluids*, 4:034004, 2019. (Cited on page 62.)
- [186] Rachid Chebbi. Absorption and spreading of a liquid droplet over a thick porous substrate. *ACS Omega*, 0:null, 0. (Cited on page 62.)
- [187] R.T. van Gaalen, C. Diddens, D.P. Siregar, H.M.A. Wijshoff, and J.G.M. Kuerten. Absorption of surfactant-laden droplets into porous media: A numerical study. *Journal of Colloid and Interface Science*, 597:149–159, 2021. (Cited on page 62.)

- [188] Karol J. Mysels. Surface tension of solutions of pure sodium dodecyl sulfate. *Langmuir*, 2:423–428, 1986. (Cited on page 63.)
- [189] Mei Li, Yahya Rharbi, Xiaoyu Huang, and Mitchell A. Winnik. Small variations in the composition and properties of triton x-100. *Journal of Colloid and Interface Science*, 230:135 – 139, 2000. (Cited on page 63.)
- [190] Gilbert D. Miles and Leo Shedlovsky. Minima in surface tension–concentration curves of solutions of sodium alcohol sulfates. *The Journal of Physical Chemistry*, 48:57–62, 1944. (Cited on page 63.)
- [191] Haris Khan, John M Seddon, Robert V Law, Nicholas J Brooks, Eric Robles, João T Cabral, and Oscar Ces. Effect of glycerol with sodium chloride on the kraft point of sodium dodecyl sulfate using surface tension. *Journal of Colloid and Interface Science*, 538:75 – 82, 2019. (Cited on page 63.)
- [192] J.G. Göbel and G.R. Joppien. Dynamic interfacial tensions of aqueous triton x-100 solutions in contact with air, cyclohexane, n-heptane, and n-hexadecane. *Journal of Colloid and Interface Science*, 191:30 – 37, 1997. (Cited on page 63.)
- [193] Hisham J. Y. El-Aila. Interaction of nonionic surfactant triton-x-100 with ionic surfactants. *Journal of Dispersion Science and Technology*, 30:1277–1280, 2009. (Cited on page 63.)
- [194] Michiko Kodama and Masaji Miura. The second cmc of the aqueous solution of sodium dodecyl sulfate. ii. viscosity and density. *Bulletin of the Chemical Society of Japan*, 45:2265–2269, 1972. (Cited on page 63.)
- [195] Rajinder Pal. Rheological behaviour of concentrated surfactant solutions and emulsions. *Colloids and Surfaces*, 64:207 – 215, 1992. (Cited on page 63.)
- [196] Jochen Winkelmann. Diffusion coefficient of sodium dodecyl sulfate in water. *Springer-Materials Vol. 15B2: “Diffusion in Gases, Liquids and Electrolytes”*, 2018. (Cited on page 63.)
- [197] Derek G. Leaist. A moving-boundary technique for the measurement of diffusion in liquids. triton x-100 in water. *Journal of Solution Chemistry*, pages 187–197, 1991. (Cited on page 63.)
- [198] Santanu Paria, C. Manohar, and Kartic C. Khilar. Adsorption of anionic and non-ionic surfactants on a cellulosic surface. *Colloids and Surfaces A: Physicochemical and Engineering Aspects*, 252:221 – 229, 2005. (Cited on pages 64 and 85.)
- [199] Victor K La Mer. *Retardation of evaporation by monolayers: transport processes*. Academic Press, 1962. (Cited on page 65.)
- [200] E. R. Noe and R. G. Dressler. Performance of odd- and even-chain pure alcohol monolayers in water evaporation retardation. *I&EC Product Research and Development*, 6:132–137, 1967. (Cited on page 65.)
- [201] G.T. Barnes. Permeation through monolayers. *Colloids and Surfaces A: Physicochemical and Engineering Aspects*, 126:149 – 158, 1997. (Cited on page 65.)
- [202] Paul Andrew Coop. *Detection of Evaporation Reducing Monolayers on Open Water Surfaces*. PhD thesis, University of New England, 2011. (Cited on page 65.)
- [203] K. Lunkenheimer and M. Zembala. Attempts to study a water evaporation retardation by soluble surfactants. *Journal of Colloid and Interface Science*, 188:363 – 371, 1997. (Cited on page 65.)

- [204] V.B. Fainerman, A.V. Makievski, J. Krägel, A. Javadi, and R. Miller. Studies of the rate of water evaporation through adsorption layers using drop shape analysis tensiometry. *Journal of Colloid and Interface Science*, 308:249 – 253, 2007. (Cited on page 65.)
- [205] Peixun Li, Buxing Han, Haike Yan, and Ruilin Liu. Vapor pressure of the aqueous solution of sodium dodecyl sulfate. *Journal of Chemical & Engineering Data*, 41:285–286, 1996. (Cited on page 65.)
- [206] R. Sadeghi and R. Hosseini. Vapor-liquid equilibrium properties of sodium n-heptyl sulfonate in water and in aqueous solutions of poly(ethylene glycol) at different temperatures. *J. Iran. Chem. Soc.*, 7:621–629, 2010. (Cited on page 65.)
- [207] Saivan Solaimani and Rahmat Sadeghi. Thermodynamic and aggregation properties of sodium n-hexylsulfonate in aqueous solution. *Fluid Phase Equilibria*, 363:106 – 116, 2014. (Cited on page 65.)
- [208] Ian Shepherd and Huining Xiao. The role of surfactants as rewetting agents in enhancing paper absorbancy. *Colloids and Surfaces A: Physicochemical and Engineering Aspects*, 157:235–244, 1999. (Cited on pages 66 and 67.)
- [209] Chunhee Kim and You-Lo Hsieh. Wetting and absorbency of nonionic surfactant solutions on cotton fabrics. *Colloids and Surfaces A: Physicochemical and Engineering Aspects*, 187-188:385–397, 2001. (Cited on page 66.)
- [210] Abraham Marmur. Penetration and displacement in capillary systems of limited size. *Advances in Colloid and Interface Science*, 39:13–33, 1992. (Cited on pages 67 and 84.)
- [211] Barbara Widera, Roland Neueder, and Werner Kunz. Vapor pressures and osmotic coefficients of aqueous solutions of sds, c6tab, and c8tab at 25 deg.c. *Langmuir*, 19:8226–8229, 2003. (Cited on page 71.)
- [212] Gianmarco Venditti, Vignesh Murali, and Anton A. Darhuber. Inkjet deposition of surfactant solutions onto thin moving porous media - experiments and simulations. *Journal of Colloid and Interface Science*, page submitted, 2021. (Cited on pages 74, 77, 79, 86, 94, and 96.)
- [213] Timothy S. Sammarco and Mark A. Burns. Thermocapillary pumping of discrete drops in microfabricated analysis devices. *AIChE Journal*, 45:350–366, 1999. (Cited on page 75.)
- [214] I. Langmuir. The adsorption of gases on plane surfaces of glass, mica and platinum. *Journal of the American Chemical Society*, 40:1361–1403, 1918. (Cited on page 77.)
- [215] M. Tschapek and C. Wasowski. Spreading of a surfactant in an unsaturated disperse material. *Colloids and Surfaces*, 5:65–73, 1982. (Cited on page 82.)
- [216] Milind V. Karkare and Tomlinson Fort. Flow in "unsaturated" porous media due to water-insoluble surfactants: Role of momentum transfer from a spreading monolayer. *Langmuir*, 10:3701–3704, 1994. (Cited on page 82.)
- [217] Eric J. Henry and James E. Smith. Numerical demonstration of surfactant concentration-dependent capillarity and viscosity effects on infiltration from a constant flux line source. *Journal of Hydrology*, 329:63 – 74, 2006. (Cited on page 82.)
- [218] Laurie Saulnier, Lorène Champougny, Gaël Bastien, Frédéric Restagno, Dominique Langevin, and Emmanuelle Rio. A study of generation and rupture of soap films. *Soft Matter*, 10:2899–2906, 2014. (Cited on page 83.)

- [219] Karol J. Mysels and Malcolm N. Jones. Direct measurement of the variation of double-layer repulsion with distance. *Discuss. Faraday Soc.*, 42:42–50, 1966. (Cited on page 83.)
- [220] D. Exerowa and A. Scheludko. Porous plate method for studying microscopic foam and emulsion films. *C. R. Acad. Bulg. Sci.*, pages 24–47, 1971. (Cited on page 83.)
- [221] Romain Aranda, Hossein Davarzani, Colombano S., Fabien Laurent, and Henri Bertin. Experimental study of foam flow in highly permeable porous media for soil remediation. *Transport in Porous Media*, 134, 2020. (Cited on page 84.)
- [222] Kun Ma, Jose L. Lopez-Salinas, Maura C. Puerto, Clarence A. Miller, Sibani Lisa Biswal, and George J. Hirasaki. Estimation of parameters for the simulation of foam flow through porous media. part 1: The dry-out effect. *Energy & Fuels*, 27:2363–2375, 2013. (Cited on page 84.)
- [223] Yong-Sheng Zhao, Yimeng Su, Jing Lian, He Wang, Lu Li, and Chuanyu Qin. Insights on flow behavior of foam in unsaturated porous media during soil flushing. *Water Environment Research*, 88:2132–2141, 2016. (Cited on page 84.)
- [224] Clément Portois, Christian S. Boeije, Henri J. Bertin, and Olivier Atteia. Foam for environmental remediation: Generation and blocking effect. *Transport in Porous Media*, 124:787–801, 2018. (Cited on page 84.)
- [225] Raphaël Poryles, Nicolas Gland, Andrew King, Elisabeth Rosenberg, Loïc Barré, and Thibaud Chevalier. Foam trapping in a 3d porous medium: in situ observations by ultra-fast x-ray microtomography. *Soft Matter*, 16:6354–6361, 2020. (Cited on page 84.)
- [226] Daniel F. Varnell. Composition and method for improved ink jet printing performance, 1999. World Patent WO1999006219A1. (Cited on page 85.)
- [227] John L. Stoffel, Hai Q Tran, Ronald A. Askeland, Lawrence E Gibson, Steven D Schultz, Michael F Koenig, Sen Yang, William R Sperry, and Richard R. Hartman. Composition and ink receiving system incorporating the composition, 2009. US Patent US7582188B2. (Cited on page 85.)
- [228] Xiaoqi Zhou. Surface treatment composition, inkjet printable article and method of making the same, 2009. World Patent WO2009157952A1. (Cited on page 85.)
- [229] Asaf Oko, Agne Swerin, Birgit D. Brandner, Douglas Bugner, Wayne Cook, and Per M. Claesson. Aggregation of inkjet ink components by ca and mg ions in relation to colorant pigment distribution in paper. *Colloids and Surfaces A: Physicochemical and Engineering Aspects*, 456:92–99, 2014. (Cited on page 85.)
- [230] Akira Watanabe. Physico-chemical studies on surface active agents. (v) the precipitation of anionic surface active agents by metal ions. *Bulletin of the Institute for Chemical Research*, 38:248–273, 1960. (Cited on pages 85 and 103.)
- [231] J.M Peacock and E Matijevic. Precipitation of alkylbenzene sulfonates with metal ions. *Journal of Colloid and Interface Science*, 77:548–554, 1980. (Cited on pages 85 and 103.)
- [232] K. Lee Matheson, Michael F. Cox, and Dewey L. Smith. Interactions between linear alkylbenzene sulfonates and water hardness ions. i. effect of calcium ion on surfactant solubility and implications for detergency performance. *Journal of the American Oil Chemists’ Society*, 62:1391–1396, 1985. (Cited on page 85.)

- [233] Kevin L. Stellner and John F. Scamehorn. Hardness tolerance of anionic surfactant solutions. 1. anionic surfactant with added monovalent electrolyte. *Langmuir*, 5:70–77, 1989. (Cited on pages 85 and 103.)
- [234] Cheryl H. Rodriguez, Lori H. Lowery, John F. Scamehorn, and Jeffrey H. Harwell. Kinetics of precipitation of surfactants. i. anionic surfactants with calcium and with cationic surfactants. *Journal of Surfactants and Detergents*, 4:1–14, 2001. (Cited on page 85.)
- [235] Lloyd R. Snyder, Joseph J. Kirkland, and John W. Dolan. *Introduction to Modern Liquid Chromatography, Third Edition*. John Wiley & Sons, 2010. (Cited on page 89.)
- [236] A.O. Kuhn and M. Lederer. Adsorption chromatography on cellulose: Ii. separations of aromatic amino acids, biogenic amines, alkaloids, dyes and phenols and determination of hydrophobic constants. *Journal of Chromatography A*, 440:165–182, 1988. (Cited on page 89.)
- [237] Bernd Spangenberg, Colin F. Poole, and Christel Weins. *Quantitative Thin-Layer Chromatography*. Springer-Verlag, 2011. (Cited on page 89.)
- [238] Wei W. Yu and Ian M. White. Chromatographic separation and detection of target analytes from complex samples using inkjet printed sers substrates. *Analyst*, 138:3679–3686, 2013. (Cited on page 89.)
- [239] Abdennour Abbas, Andrew Brimer, Joseph M. Slocik, Limei Tian, Rajesh R. Naik, and Srikanth Singamaneni. Multifunctional analytical platform on a paper strip: Separation, preconcentration, and subattomolar detection. *Analytical Chemistry*, 85:3977–3983, 2013. (Cited on page 89.)
- [240] D. Donigian, P. C. Wernett, M. McFadden, and J. J. McKay. Ink-jet dye fixation and coating pigments. *Tappi Journal*, 82:175–182, 1999. (Cited on pages 90 and 104.)
- [241] R. N. S. Sodhi, L. Sun, M. Sain, and R. Farnood. Analysis of ink/coating penetration on paper surfaces by time-of-flight secondary ion mass spectrometry (tof-sims) in conjunction with principal component analysis (pca). *The Journal of Adhesion*, 84:277–292, 2008. (Cited on page 90.)
- [242] A. Filenkova, E. Acosta, P. M. Brodersen, R. N. S. Sodhi, and R. Farnood. Distribution of inkjet ink components via tof-sims imaging. *Surface and Interface Analysis*, 43:576–581, 2011. (Cited on page 90.)
- [243] Risto Koivunen, Eveliina Jutila, Roger Bollström, and Patrick Gane. Investigating chromatographic interactions in porous pigment coatings between inkjettable polyelectrolytes and model colorant solutions. *Colloids and Surfaces A: Physicochemical and Engineering Aspects*, 579:123676, 2019. (Cited on page 92.)
- [244] Ján Široký, Richard S. Blackburn, Thomas Bechtold, Jim Taylor, and Patrick White. Alkali treatment of cellulose ii fibres and effect on dye sorption. *Carbohydrate Polymers*, 84(1):299–307, 2011. (Cited on page 100.)
- [245] Mokhtar Arami, Nargess Yousefi Limaee, Niyaz Mohammad Mahmoodi, and Nooshin Salman Tabrizi. Equilibrium and kinetics studies for the adsorption of direct and acid dyes from aqueous solution by soy meal hull. *Journal of Hazardous Materials*, 135:171–179, 2006. (Cited on page 100.)
- [246] Vita Halysh, Pikus Stanisław, G. Dobele, Bogdan Pasalskiy, Volodymyr Gun'ko, and Mykola Kartel. Sugarcane bagasse and straw as low-cost lignocellulosic sorbents for the removal of dyes and metal ions from water. *Cellulose*, 27:8181–8197, 2020. (Cited on page 100.)

- [247] Ridha Lafi, Lotfi Abdellaoui, Imed Montasser, and Amor Hafiane. Removal of methyl orange from aqueous solution onto modified extracted cellulose from stipa tenacissima l. *International Journal of Environmental Analytical Chemistry*, 0:1–17, 2020. (Cited on page 100.)
- [248] Chun-Hui Zhou, Di Zhang, Dong-Shen Tong, Lin-Mei Wu, Wei-Hua Yu, and Suryadi Ismadji. Paper-like composites of cellulose acetate–organo-montmorillonite for removal of hazardous anionic dye in water. *Chemical Engineering Journal*, 209:223–234, 2012. (Cited on page 100.)
- [249] Aparna Roy, Basudam Adhikari, and S. B. Majumder. Equilibrium, kinetic, and thermodynamic studies of azo dye adsorption from aqueous solution by chemically modified lignocellulosic jute fiber. *Industrial & Engineering Chemistry Research*, 52:6502–6512, 2013. (Cited on page 100.)
- [250] Cesar Laureano-Anzaldo, Nadia Berenice Haro, Juan Meza-Contreras, Jorge Robledo-Ortíz, and Ricardo Manríquez-González. Chemical modification of cellulose with zwitterion moieties used in the uptake of red congo dye from aqueous media. *Cellulose*, 26:9207–9227, 2019. (Cited on page 100.)
- [251] Miaolin Hou and George L. Baughman. Predicting the precipitation of acid and direct dyes in natural waters. *Dyes and Pigments*, 18:35–46, 1992. (Cited on page 103.)
- [252] Vipasiri Vimonses, Bo Jin, and Christopher W.K. Chow. Insight into removal kinetic and mechanisms of anionic dye by calcined clay materials and lime. *Journal of Hazardous Materials*, 177:420–427, 2010. (Cited on page 103.)
- [253] C. M. Gilbert Carlsson and Goeran Stroem. Reduction and oxidation of cellulose surfaces by means of cold plasma. *Langmuir*, 7:2492–2497, 1991. (Cited on page 104.)
- [254] Kuanjun Fang, Shaohua Wang, Chaoxia Wang, and Anli Tian. Inkjet printing effects of pigment inks on silk fabrics surface-modified with o₂ plasma. *Journal of Applied Polymer Science*, 107:2949–2955, 2008. (Cited on page 104.)
- [255] Mikko Tuominen, Johanna Lahti, Juho Lavonen, Tapani Penttinen, Jari P. Räsänen, and Jurkka Kuusipalo. The influence of flame, corona and atmospheric plasma treatments on surface properties and digital print quality of extrusion coated paper. *Journal of Adhesion Science and Technology*, 24:471–492, 2010. (Cited on page 104.)
- [256] Sami-Seppo Ovaska, Katriina Mielonen, Kaj Backfolk, Tadeusz Lozovski, Ringaudas Rinkunas, and Jonas Sidaravicius. A novel approach for studying the effects of corona treatment on ink-substrate interactions. *Nordic Pulp & Paper Research Journal*, 30:681–688, 2015. (Cited on page 104.)
- [257] Joanna Pawlat, Piotr Terebun, Michał Kwiatkowski, and Jaroslaw Diatczyk. RF atmospheric plasma jet surface treatment of paper. *Journal of Physics D: Applied Physics*, 49:374001, 2016. (Cited on page 104.)
- [258] Chunming Zhang, Libing Wang, Miao Yu, Lijun Qu, Yajing Men, and Xiangwu Zhang. Surface processing and ageing behavior of silk fabrics treated with atmospheric-pressure plasma for pigment-based ink-jet printing. *Applied Surface Science*, 434:198–203, 2018. (Cited on page 104.)
- [259] Rahul Navik, Sameera Shafi, Md Miskatul Alam, Md Amjad Farooq, Lina Lin, and Yingjie Cai. Influence of dielectric barrier discharge treatment on mechanical and dyeing properties of wool. *Plasma Science and Technology*, 20:065504, 2018. (Cited on page 104.)

- [260] Pei-Ching Yu, Chih-I Chen, Rung-Je Yang, Fu-Su Yen, and Shih-Tsung Max Yen. Porous χ - al_2o_3 flake powder as dye-fixing materials for inkjet printing paper. *Journal of the American Ceramic Society*, 95:2124–2126, 2012. (Cited on page 104.)
- [261] Katriina Mielonen, Pavel Geydt, Monika Österberg, Leena-Sisko Johansson, and Kaj Backfolk. Inkjet ink spreading on polyelectrolyte multilayers deposited on pigment coated paper. *Journal of Colloid and Interface Science*, 438:179–190, 2015. (Cited on page 104.)
- [262] Katriina Mielonen, Teija Laukala, Johanna Lyytikäinen, and Kaj Backfolk. The effect of anionic-cationic multilayering and microstructure on dye-based ink absorption. *Chemical Engineering Science*, 190:396–404, 2018. (Cited on page 104.)
- [263] Haizhen Yang, Kuanjun Fang, Xiuming Liu, and Fangfang An. High-quality images inkjetted on different woven cotton fabrics cationized with p(st-ba-vbt) copolymer nanospheres. *ACS Applied Materials & Interfaces*, 11:29218–29230, 2019. (Cited on page 104.)
- [264] D.M. Lewis. The chemistry of reactive dyes and their application processes. In M. Clark, editor, *Handbook of Textile and Industrial Dyeing*, volume 1 of *Woodhead Publishing Series in Textiles*, pages 303–364. Woodhead Publishing, 2011. (Cited on page 104.)
- [265] Min Li, Liping Zhang, Yajie An, Wujun Ma, and Shaohai Fu. Relationship between silk fabric pretreatment, droplet spreading, and ink-jet printing accuracy of reactive dye inks. *Journal of Applied Polymer Science*, 135:46703, 2018. (Cited on page 104.)
- [266] Yawei Song, Kuanjun Fang, Mohd Nadeem Bukhari, Yanfei Ren, Kun Zhang, and Zhiyuan Tang. Green and efficient inkjet printing of cotton fabrics using reactive dye@copolymer nanospheres. *ACS Applied Materials & Interfaces*, 12:45281–45295, 2020. (Cited on page 104.)
- [267] Bernard John Eastlund, Donald Emmett Spann, and Dheya Mortada Alfekri. Microwave energy ink drying method, 2003. US Patent 6,508,550 B1. (Cited on page 104.)
- [268] S Dana Seccombe. Printer including microwave dryer, 2003. US Patent 6,578,959 B1. (Cited on page 104.)
- [269] Geoff Wotton and Michael Klopfenstein. Microwave applicator for inkjet printer, 2003. US Patent 6,663,239 B2. (Cited on page 104.)
- [270] Kenneth Wolnick and William Decker. Infrared dryer for printing presses, 1989. US Patent 4,809,608. (Cited on page 104.)
- [271] Ying Li, Wen Juan Gu, and Bang Gui He. Research on the influence of drying method on ink penetration of coated paper. In *Biotechnology, Chemical and Materials Engineering III*, volume 884 of *Advanced Materials Research*, pages 312–315, 2014. (Cited on page 104.)
- [272] Xu Jingxiang, Li Jinyao, Li Haichao, Zhang Mingming, and Cai Jifei. Research progress on water-based ink drying technology. *IOP Conference Series: Materials Science and Engineering*, 565:012017, 2019. (Cited on page 104.)

Summary

The physics of ink-jet printing onto thin porous substrates

Ink-jet printing consists of ejection and precise deposition of ink droplets onto substrates that are moving underneath the printhead. For ink-jet printing onto porous substrates, water based inks are in widespread use that are beneficial from an environmental standpoint. Depending on the chemistry of the receiving porous substrate and the nature of the ink-solvent, upon impact, the ejected ink may form non-wetting drops or may spread until the contact angle reaches the receding angle after which the droplets retract, with their volume rapidly vanishing. During this time, absorption occurs manifested as the advance of the wicking front (saturated flow) and unsaturated flow, with simultaneous evaporation of the solvent. Any added solute, such as a dye, then adsorbs onto the substrate.

In this dissertation, the unsaturated flow regime occurring on a time-scale of seconds or larger (10^0 - 10^3 s) is studied with particular focus on the heat and mass transfer aspects governing ink-jet printing. The main contributions to mass transfer arise from evaporation of the solvent and the condensation of the vapor phase and lateral wicking inside the paper. These effects translate as changes in the temperature of the paper.

To this end, infrared (IR) thermography is developed as an experimental tool to unravel the thermal signature associated with the solvent (water) – substrate (paper) interactions (Chapter 2). Using IR thermography, the temperature changes accompanying water imbibition into thin porous media that are in direct contact with the ambient atmosphere are studied. Through systematic experiments, where a dry substrate is moved into a stationary wet zone at a constant speed of the motion of the substrate (U_{sub}), temperature increases up to 3°C are measured. Quantifying the temperature increase as a function of U_{sub} is the key objective. The reason for the temperature increase is due to both the motion of the dry substrate into a stationary wet-zone (sorptive heating) leading to an increase in the mass of the liquid in the paper, and due to the recondensation of the evaporated water. As will be shown, recondensation

of the evaporated water has a stronger impact on the temperature profile than sorptive heating for low substrate speeds. Furthermore, a theoretical model is developed considering 1-D Richards' equation for unsaturated flow in porous media with heat transfer and evaporative mass-loss coupled to a 2-D gas phase domain where the flow of the gas, transport of vapor and the temperature changes of the surrounding air are considered.

Subsequently, ink-jet printing by using a piezo-driven ink-jet nozzle to deposit drops of pure water onto a moving porous substrates to form lines is studied (Chapter 3). Here systematization is done by changing U_{sub} and the frequency of jetting (f). Optical transmission imaging is developed as an experimental method along with IR thermography to measure moisture content and evaporative cooling respectively. This has culminated in the systematic measurement of moisture content and evaporation induced temperature changes as functions of U_{sub} and f . A 2-D numerical model coupling Richards' equation for unsaturated flow and heat transfer is developed for systematic comparison with the experiments. The salient feature of this model is the ink-jet deposition function which models the addition of ink-jet drops approximated as a continuous liquid jet onto paper at a particular frequency of jetting. The combination of experiments and numerical modeling yields detailed insights into the various transport processes governing ink-jet printing onto moving paper sheets.

The role of surfactants in ink-jet printing is explored (Chapter 4). The deposition of lines of ink-jet deposited droplets of surfactant solutions is studied again through systematic series of experiments as functions of U_{sub} and f , using optical transmission imaging and IR thermography. The experiments in this dissertation present clear visualization of the effect of surfactant on the moisture content which primarily arises due to gradients in the surfactant concentration, inducing capillary pressure gradients which trigger moisture migration within the wet-zone from contaminated zones of high surfactant concentration to purer zones of low or zero surfactant concentration. It is shown from drop-casting and during ink-jet printing that the surfactant front always lags the solvent front due to adsorption of the surfactant onto the fibres of the paper. Moreover, the experiments play an integral role in the validation of the dual-porosity numerical model developed by the theoretical counter-part of this work.

Through the study detailed in chapter 4, the stage is set for quantifying the chromatographic separation of water-dye mixtures (Chapter 5). Dyes exhibit a stronger interaction with the paper matrix due to their relatively large size. Moreover, different dyes are known to exhibit different delays behind the advancing solvent front. Experiments are performed in the context of drop-casting and ink-jet printing to measure the delay or retardation of different types of

dyes in paper. This retardation is essential to achieving the required resolution and color homogeneity.

Finally, Chapter 6 summarizes the main findings of this work and offers some recommendations for future study.

Curriculum Vitae

- 21 August 1991 Born in Chennai, India
- 2009-2013 **Bachelor of Technology, Mechatronics Engineering**
SASTRA University
Thanjavur, India
- 2015–2017 **Master of Science, Mechanical Engineering**
Eindhoven University of Technology
Eindhoven, The Netherlands
- 2017–2021 **PhD in Applied Physics**
Fluids and Flows group
Department of Applied Physics
Eindhoven University of Technology
Eindhoven, The Netherlands

List of publications and conferences

This thesis is based on the following publications

- V. Murali, Zeegers J.C.H and A.A. Darhuber Infrared thermography of sorptive heating of thin porous media- experiments and simulations. *International Journal of Heat and Mass Transfer*. 147, 10 p., 118875. **(Chapter 2)**
- V. Murali, G. Venditti, Zeegers J.C.H and A.A. Darhuber Inkjet deposition of lines onto thin moving porous media- experiments and simulations. *International Journal of Heat and Mass Transfer*. 176, 11 p., 121466. **(Chapter 3)**
- G. Venditti, V. Murali, and A.A. Darhuber Inkjet deposition of lines of surfactant solutions onto thin moving porous media- experiments and simulations. *Submitted to Colloids and Surfaces A: Physicochemical and Engineering Aspects*. **(Chapter 4)**
- G. Venditti, V. Murali and A.A. Darhuber Chromatographic effects in ink-jet printing. *Submitted to Langmuir (Accepted)*. **(Chapter 5)**

Conference contributions

Oral presentations

- V. Murali, Zeegers J.C.H and A.A. Darhuber "Infrared thermography of sorptive heating of thin porous media." Canon Production Printing, Venlo, The Netherlands, March 2019
- V. Murali, Zeegers J.C.H and A.A. Darhuber "Infrared thermography of sorptive heating of thin porous media." Interpore 2019, Valencia, Spain, May 2019.
- V. Murali, Zeegers J.C.H and A.A. Darhuber "Infrared thermography of sorptive heating of thin porous media." Physics@Veldhoven 2020, Veldhoven, The Netherlands, January 2020.

- V. Murali, Zeegers J.C.H and A.A. Darhuber "The physics of ink-jet printing onto thin porous media" Liquid penetration day, Canon Production Printing, Venlo, The Netherlands, October 2020.
- V. Murali, G. Venditti, Zeegers J.C.H and Darhuber A.A. "Ink-jet deposition of lines onto thin moving porous media." Interpore 2021, May 2021.
- V. Murali, G. Venditti, and A.A Darhuber . "Ink-jet printing lines of pure and surfactant solutions onto thin moving porous media." Canon Production Printing, Venlo, The Netherlands, May 2021.
- V.Murali, G. Venditti, Zeegers J.C.H and A.A. Darhuber "Ink-jet printing lines of pure and surfactant solutions onto thin moving porous media." ECS 2021, Brussels, Belgium, September 2021.

Poster presentations

- V. Murali, Zeegers J.C.H and A.A. Darhuber "Infrared thermography of sorptive heating of thin porous media." Fundamentals of ink-jet printing workshop, Lorentz center, Leiden, The Netherlands, July 2019
- G. Venditti, V. Murali and A.A. Darhuber "Ink-jet deposition of lines onto thin moving porous media- simulations." Interpore 2020, May 2021.
- G. Venditti, V. Murali and A.A. Darhuber "Ink-jet deposition of lines onto thin moving porous media- simulations." ECS 2021, Brussels, Belgium, September 2021.

Acknowledgements

As the curtain falls on my time as a PhD candidate, the moment is ripe to reflect on the past four years and thank several people who have played important roles in my growth as a physicist.

First and foremost, I would like to thank my supervisor Anton Darhuber for giving me the opportunity to work on the fascinating topics of microfluidics and transport phenomena. Throughout the past four years, I have enjoyed and benefited greatly from working closely with him and learning from him. I am very grateful for all his support, guidance and most of all for all the time he patiently spent with me to improve various aspects of my work. In particular, his advice on improving the tenor and style of my presentations has been most valuable, as my talks in many conferences since have been received well. I would also like to thank Jos Zeegers for his support from the days when I was a master student. Jos' pragmatic approach has always helped me stay on track. Furthermore, I would like to thank Hans Kuerten who was my mentor during my master's study and it was he who strongly encouraged me to study ink-jet printing for my PhD. I wish to extend thanks to Nicloae Tomozeiu for being an active member in the bi-weekly meetings and for his valuable suggestions to improve the work and constant motivation. I thank the other members of the user committee, Herman Wijshoff, Holger Steeb, Jurian Luiken, Marco Ramioli and Wouter den Otter for their feedback and suggestions over the past four years. I'm grateful to have been part of a large collaboration between TU/e and Canon Production Printing. The latter organization's various scientific activities have been very helpful for many PhD students. The role of Jorgen van der Veen in the successful completion of the many experiments detailed in this thesis has been important. His knowledge of optics has been crucial. He too has always been available to lend support whenever I approached him. Gerald Oerlemans is thanked for his support on the mechanics side of my experiments. I thank all staff members of our group, particularly, Matias, Rudie and Hanneke for lunch-time discussions and post-conference discussions. A very special thanks to the secretary of our group, Marjan Rodenburg, for organising all aspects from Bbqs to reimbursements. Without her help, many of us would be lost.

An observant reader of this thesis might have come across the name Gian-

marco Venditti often. The work detailed in this thesis is a collaborative effort between myself and Gianmarco. I thank him for his friendship and for being a great guy to work with and chill. I thank my other friends from the group Twan, Karun, Andres, Matteo, Cosimo, Rik, Steven, Kim, Abheeti, Haijing, Ralf and Timo for the many Thursday borrel sessions before all the madness with corona. Special thanks to Rik for being my office mate and participating in a lot of banter sessions. Special thanks also to Gianluca (and his better half, Alicia) for the numerous chilling sessions and Christmas dinner. Several others outside the TU/e have also contributed immensely for my life in Eindhoven, notably, my friends from the gym Tariq and Rob (whose surname still eludes me). I thank Rob for introducing me to the dead-lift and the clean and press. There are only a few activities that give me as much satisfaction as the display of raw and primal strength during a flawless dead-lift.

I thank Martijn and Irene for being gracious dinner hosts many times in the last 4-5 years and also for taking me to many cool parties in Eindhoven, which I would have never known about otherwise. I thank Ilya Kolpakov for being my running buddy and for always being there in times of need. A very special thanks to my friend Giulia Janzen, for the countless chilling sessions, trips and discussions, especially during the difficult days of corona curfew. My efforts to make you watch football will one day reap reward. I am also very pleased to have a friend in Qierui Zhang from Univeristy of Twente. Her time and effort to improve my CV and actually finding right positions for me to apply have been immensely helpful.

I would also like to thank my friends from India Ramc, HHS, Krish, Prakaash, Susa, Pranav, Antara and Vishnu. The bond forged in our bachelor days is still strong. Some of you also visited me in Europe and I will always cherish the many great times we've had together. Soon we will meet in our favourite Chennai.

Last but not the least, I thank my parents, for, without them none of this would have been possible.

Vignesh

Eindhoven,
The Netherlands, August 2021